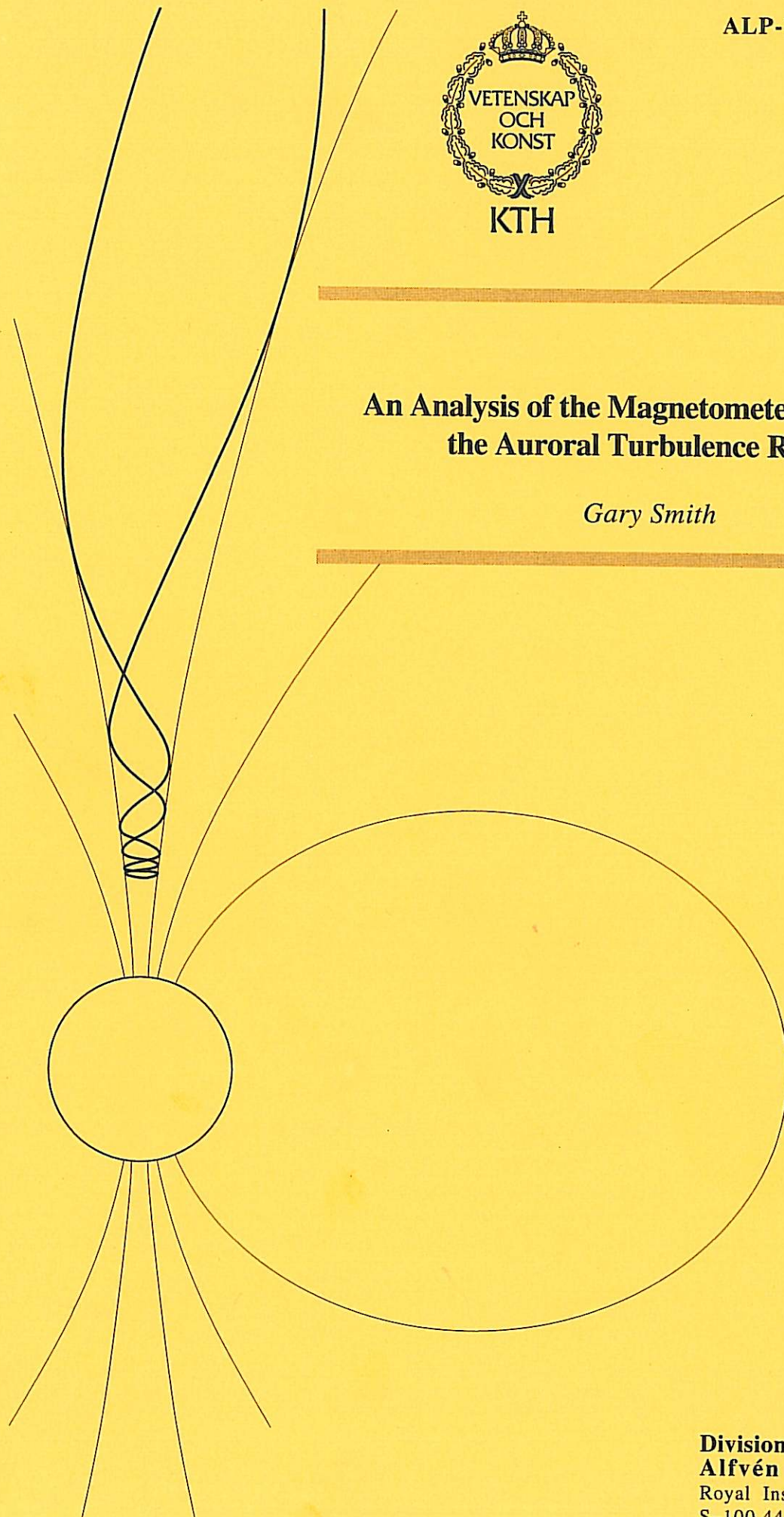


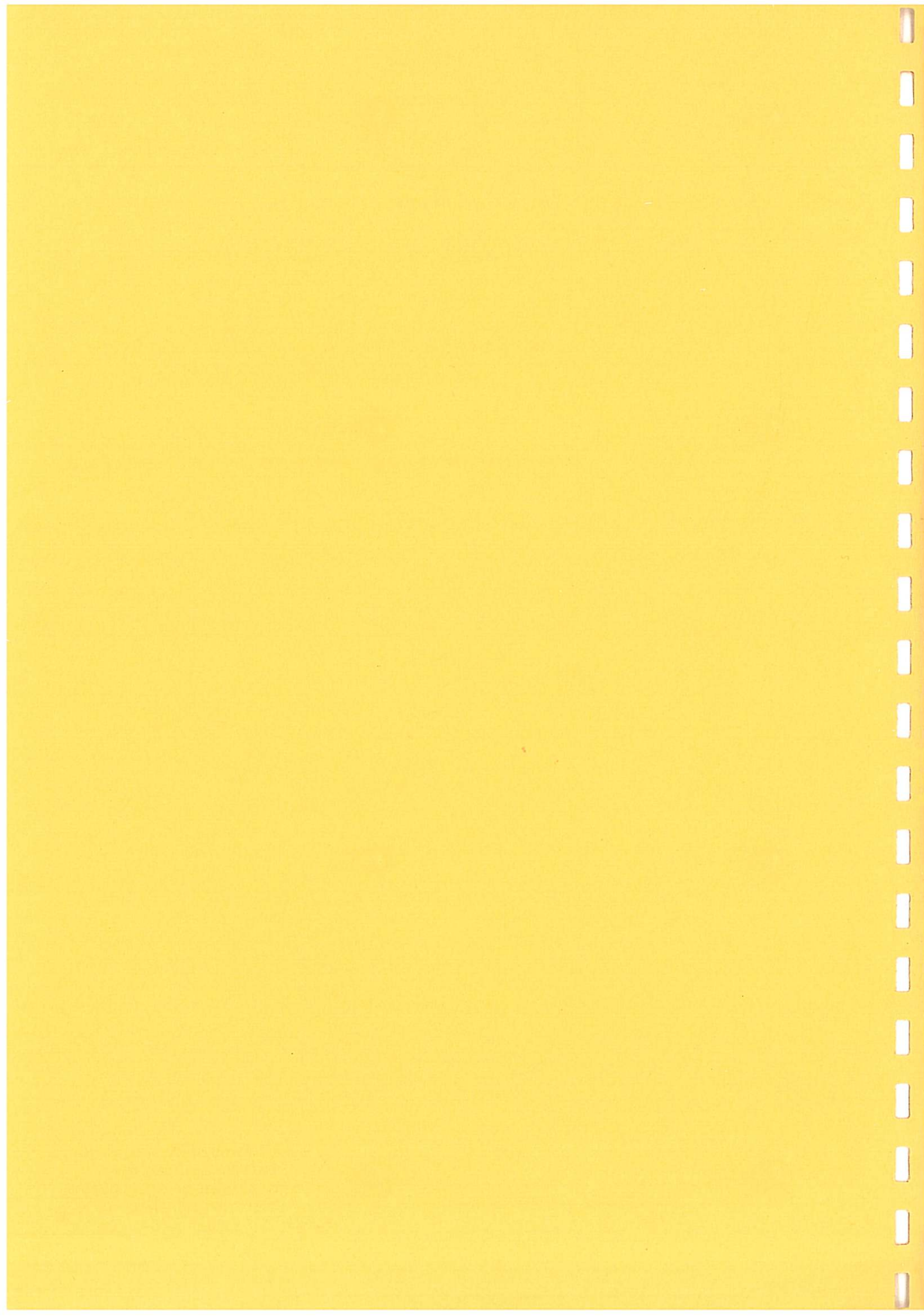


An Analysis of the Magnetometer Data from the Auroral Turbulence Rocket

Gary Smith



**Division of Plasma Physics
Alfvén Laboratory**
Royal Institute of Technology
S-100 44 Stockholm, Sweden

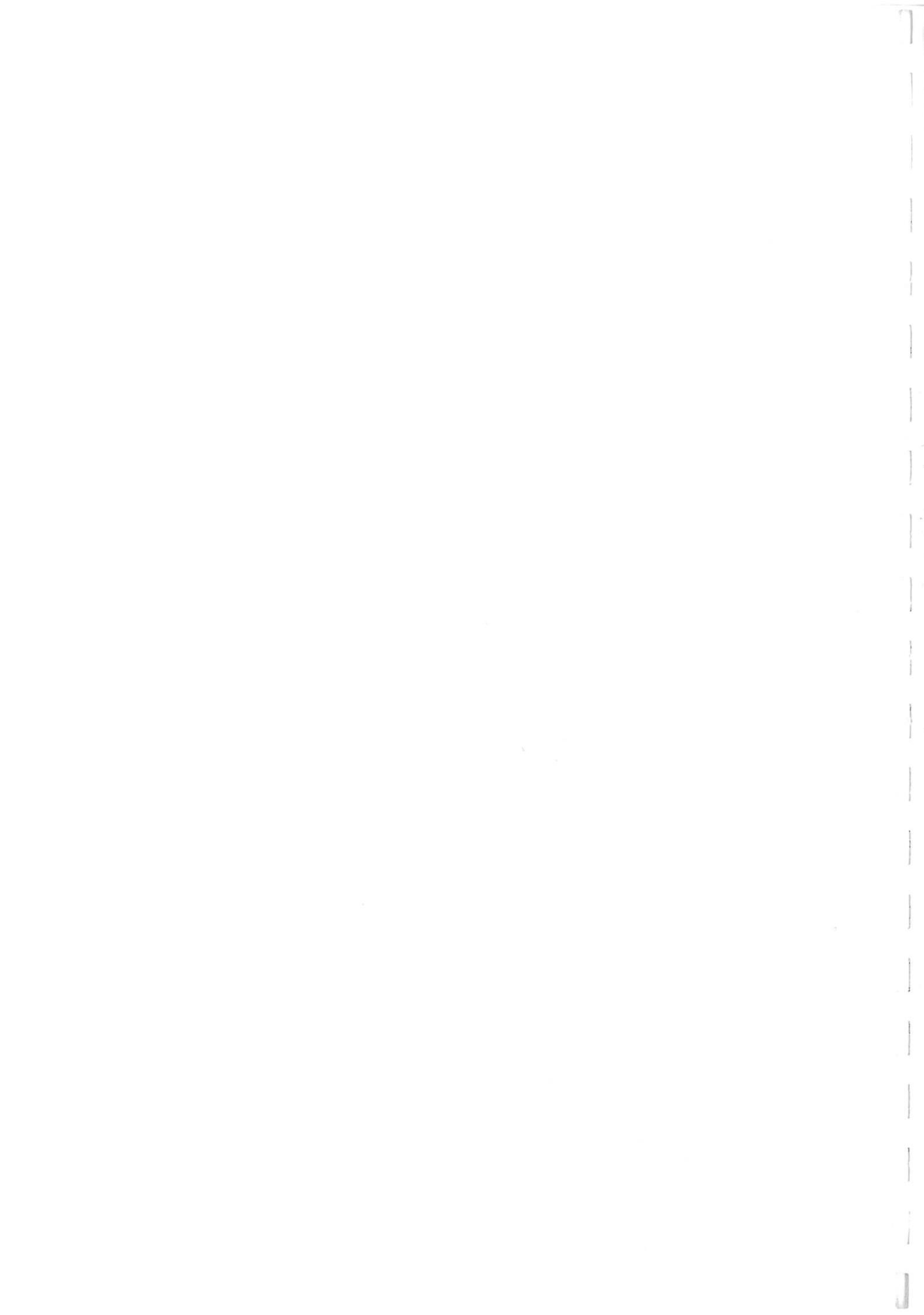


An Analysis of the Magnetometer Data from the Auroral Turbulence Rocket

Gary Smith

Division of Plasma Physics
Alfvén Laboratory
Royal Institute of Technology
S-100 44 Stockholm, Sweden

September 1995



Abstract

This report presents the magnetic field data reduction for the Auroral Turbulence sounding rocket. A technique was developed for removing the unwanted oscillations due to the spinning and coning of the payload.

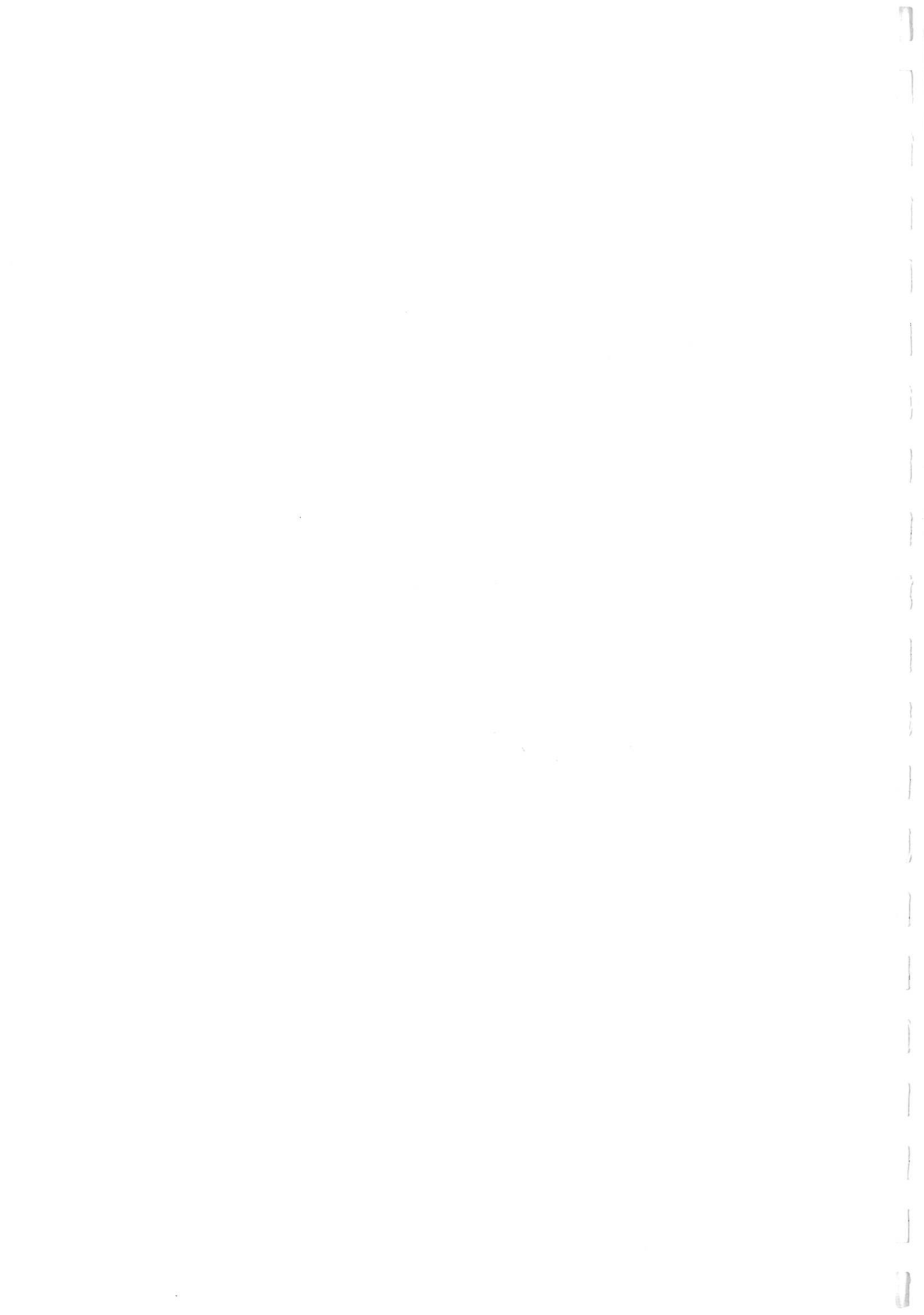
Application of this technique during the traversal of a break-up auroral arc yielded results accurate to the order of 5 nT.

The results show increased perturbations of the perpendicular magnetic field inside the arc, which appear to correlate in some places with electric field disturbances. The ratio of the magnitudes of these disturbances is not inconsistent with the presence of Alfvén waves.

Contents

Introduction	Overview of report	1
	1 The Aurora: An Introduction	2
	1.1 The Occurrence of Aurora	2
	1.2 Observations of the Aurora	2
	1.3 The Cause of the Aurora	3
	1.4 Energy Emission from the Sun	3
	1.5 The Solar Wind	3
	1.6 The Interplanetary Magnetic Field	4
	1.7 The Magnetosphere	5
	1.8 The Solar Wind -Magnetospheric Dynamo	5
	1.9 The Ionosphere	6
	1.10 Magnetosphere- Ionosphere Coupling	7
	1.11 Region 1 Currents	8
	1.12 The Neutral sheet Current	9
	1.13 The Ring Current	9
	1.14 Region 2 Currents	9
	1.15 The Auroral Electrojets	9
	1.16 Particle Precipitation and the Aurora	10
	1.17 The Auroral Potential Structure	11
	1.18 Discrete Aurora	11
	1.19 Summary	11
	2 The Auroral Turbulence	13
	Mission	
	2.1 Sounding Rocket Flights	13
	2.2 Auroral Substorms	14
	2.3 Problems Associated with Rocket Magnetic Field Measurements	15
	2.4 Overview of the Data Reduction	15
	3 Rocket Dynamics	17
	3.1 Rigid Body Motion	17
	4 Effect of Rocket Dynamics on Magnetic Field Measurements	20
	4.1 The Magnetometer	20
	4.2 Notation	20
	4.3 Simple Examples of Effects on Magnetic Field Measurements	21
	4.4 Simulation of Rocket Motion	22
	4.5 Discussion	24
	5 Magnetometer data Handling	25
	5.1 Raw Data Provided	25
	5.2 Filtering of the Data	25
	5.3 Calibration of the Magnetometer	25
	5.4 technique for "In Flight" Calibration	27
	5.5 Practicalities of Re-Calibration	28
	5.6 Variation of Parameters during the Flight	30
	5.7 Estimate of Errors Caused by Miscalibration	31
	6 Magnetic Field Measurements	34
	6.1 Initial observations	34
	6.2 Possible Interpretation of the Results	35
	6.3 Fitting of Parameters to the Data	37
	6.4 Errors in Parameter fitting	40
	6.5 Extensions to Longer Time Periods	40

6.6	Removing the Motion of the Rocket from the Data	41
6.7	Final Corrections to the Results	42
6.8	Errors due to Data Reduction	42
7	Interpretation of Results	43
7.1	Rocket Dynamics	43
7.2	The Auroral Arc	43
8	Summary	45
9	Further Work	46
	References	47
Appendix A	Data Storage	49
Appendix B	Missing and Repeated records	50
Appendix C	Filtering	52
Appendix D	Incorrect Modelling of the Rocket Motion	54
Appendix E	Text Files Output From <i>Fit_10</i>	56
	Figures 1-40	57



Figures

- 1 Position of the auroral oval
- 2 Height distribution of aurora
- 3 Electron density height variation in the Earth's atmosphere
- 4 Average position of field aligned current systems
- 5 Magnetospheric plasma regions
- 6 Large scale current flow in the Earth's magnetic tail
- 7 Auroral electrojets
- 8 Distribution of diffuse aurora
- 9 Statistical occurrence of discrete aurora
- 10 Summary of auroral phenomena

- 11 Evolution of an auroral substorm
- 12 Flight path of Auroral Turbulence

- 13 Electron energy data
- 14 Height of rocket during arc interception
- 15 Deviation of flight path from a parabola
- 16 Definition of rocket axes

- 17 Effect of magnetometer displaced from rocket's centre of mass
- 18 Demonstration of spin motion
- 19 Demonstration of coning motion
- 20 Projection of coning into 2-dimensions
- 21 Simulations of pure spinning or coning
- 22 Simulations of spinning and coning combined

- 23 Definition of non-orthogonality angles
- 24 Magnetic field magnitude based on ground calibration
- 25 Time variation of calculated calibration parameters

- 26 Magnetic field data for whole flight
- 27 Magnetic field data from period of normal operation
- 28 Magnetic field data from 250 to 330 seconds
- 29 Calculation of angles from magnetic field data
- 30 Angles calculated from magnetic field data
- 31 Demonstration of misalignment of magnetometer and spin axis
- 32 Simulation of magnetometer motion, misaligned with spin axis of rocket
- 33 Definition of misalignment angles
- 34 Fitting of model to the rotational motion of the rocket
- 35 Rotations required to compensate for rocket's attitude changes
- 36 Three axis results for magnetic field
- 37 Parallel and perpendicular magnetic fields
- 38 Perpendicular electric and magnetic fields (large scale)
- 39 Perpendicular electric and magnetic fields (small scale)
- 40 Z-axis Magnetic Field and Its Deviation From a Mean Value

- C1 Filter gain response
- C2 Filter phase response
- C3 Time delay of filter

Introduction: Overview of Report

This project deals with the initial analysis of magnetic field measurements from the Auroral Turbulence sounding rocket.

In order to put this data into context, a general introduction is given in Section 1, dealing with the large scale features of the aurora. Section 2 discusses the precise conditions, and problems, associated with Auroral Turbulence.

The theory for the data reduction is then developed and a its implementation presented and discussed. A number of difficulties arise with the technique because of the large numbers of time varying parameters needed to define the rocket motion.

The results obtained from this are presented in Section 7, and some possible interpretations put forward in Section 8. The report concludes with a short discussion of possible investigations, which the magnetic field data could play a role in.

A number of FORTRAN routines were written for use in this report, each of which will be represented with its name in *italics*.

1 The Aurora: An Introduction.

"The eastern sky was massed with swaying auroral light, the most vivid and beautiful display that I had ever seen - fold on fold the arches and curtains of vibrating luminosity rose and spread across the sky, to slowly fade and yet again spring to glowing life."

Robert F. Scott

The above description of an auroral display observed by Scott during his trek to the South Pole demonstrates a number of typical features of the aurora, although the highly dynamic, coloured arcs and curtains described above are just one manifestation of the phenomena we call aurora today. For a good guide to the different appearances of the aurora see, for example The International Auroral Atlas, 1963.

1.1 The Occurrence of Aurora

Although not restricted to high latitude regions, the aurora is rarely seen outside of the polar regions, and most commonly occurs in roughly circular zones (radius approximately 22° of latitude) centred on the geomagnetic poles. A distinction is made between the auroral zone and the auroral oval, the former being the areas on Earth where, as an average, the aurora is likely to be seen. The latter is an instantaneous description of where aurora occur, and represents an oval, fixed relative to the Sun, under which the Earth rotates (Figure 1).

The height distribution of aurora is also of interest, the first measurements of which were by Cavendish in 1784. However, it was not until the twentieth century, and the photographic work of Störmer, that the question was properly addressed. Figure 2 shows results indicating the variation of height with geomagnetic latitude and magnetic local time. As seen here the majority of aurora occur at altitudes between 100 and 150 km.

1.2 Observations of the Aurora

Scott's description reflects the magnificence of the aurora, but also indicates that such displays are not that common, even in areas which are frequently under the auroral oval. In fact the name aurora encompasses many different effects, observable at a distance, from both the ground and in space, across a wide range of electromagnetic frequencies. The length and time scales, as well as the intensities, vary immensely, from the almost invisible diffuse aurora, nearly uniform over large areas, to the very strong, dynamic curtains called discrete aurora. The latter may have spatial extents of the order of 10 km in the direction across the curtain, but also exhibit fine structure down to scales of 100 m (Borovsky and Suszcynsky, 1993), yet may extend for hundreds of kilometres along the curtain's length.

It should also be noted that signals associated with auroral forms have been recorded in sound waves (Chrzanowski *et al.*, 1961), X-rays (Brown, 1966), and kilometre wavelength radio waves (Gurnett and Inan, 1988), as well as the most commonly observed whitish-green light, with a wavelength of 557.7 nm. A large number of spectral lines at ultra-violet, visible and near infra-red wavelengths are also apparent in different types of aurora (Vallance Jones, 1991).

1.3 The Cause of the Aurora

The twelfth century Norse chronicle, "The King's Mirror" proposes three possible explanations for the aurora.

- i. A fire encircling the Earth
- ii. Creation of light by the Sun
- iii. Re-emission of sunlight absorbed by snow and ice

It is now apparent that the energy source for the aurora is indeed the Sun (as in the second and third proposals above), but by a quite different mechanism than indicated by these theories. It is essential in considering the occurrence and form of aurora to consider how that energy is received by the Earth.

1.4 Energy Emission from the Sun

The release of energy from the Sun can be split into three main parts,

- i. Thermal (blackbody) radiation
- ii. X-ray and extreme ultra-violet radiation
- iii. The solar wind

Table 1 shows the proportions of solar irradiance (power received per metre square of the Earth's surface) for different wavelength regimes.

Table 1 - Electromagnetic energy from the Sun.

Wavelength range	Proportion of Solar Irradiance
Greater than 1.0 μm	<30%
0.32 μm - 1.0 μm	>70%
Less than 0.32 μm	<2%

From Geophysics Handbook

The solar wind is a highly ionised, magnetised plasma continually flowing outward from the Sun at speeds of around 400 km/s. It is electrically quasi-neutral, with almost all negative charge carriers being electrons, and 95% of positive charge carriers being protons. Estimations are that it is responsible for about 10^{-6} of the total energy loss from the Sun, so at first glance appears insignificant compared to the electromagnetic radiation. However, in theories of the aurora, it is this plasma that provides the energy.

1.5 The Solar Wind

The speed of the solar wind is greater than both the speed of sound, and the so-called Alfvén velocity for the plasma. (The Alfvén velocity is the normal propagation velocity for electromagnetic disturbances in a plasma.) This means that information can not be carried upstream in the solar wind, and, as with supersonic flow of air around a jet aeroplane, a shock wave is formed. The shock wave causes the plasma from the solar wind to slow, and to be heated through compression. The region of turbulent plasma just on the Earth side of the shock wave is termed the magnetosheath. The dominant magnetic field in this region originates at the Sun, and is termed the Interplanetary Magnetic Field (IMF). The heating across the shock wave is demonstrated in Table 2 by

typical values for values of the plasma density and temperature in various regions in near-Earth space.

Table 2- Plasma density and temperature for different regions of the near Earth environment.(Figure 5)

	Density (cm^{-3})	Ion kinetic temperature (eV)
Ionosphere	$10^3 - 10^6$	0.3
Plasmasphere	$1 - 10^3$	1
	Plasmapause	
Plasma Sheet	1	6000
PlasmaSheet Boundary Layer	0.1-0.5	500
Lobe	<0.1	100
Magnetospheric Boundary Layer	0.5-2	4000
	Magnetopause	
Magnetosheath	5	800
	Bow Shock	
Solar Wind	5	10

As mentioned above, the solar wind carries about 10^{-6} of the total energy from the Sun. The energy is transported to the near Earth environment in a number of forms (Table 3), but more than 95% is due to the kinetic energy associated with bulk flow. It is this energy which drives the aurora, after being converted to an electrical form in the near Earth environment. The efficiency of this conversion process is controlled by the interplanetary magnetic field.

Table 3 - Energy transportation by the Solar Wind

Type of energy	Percentage of total
Bulk plasma flow	95 %
Thermal energy of protons	$<1\%$
Thermal energy of electrons	2%
Magnetic field	1.5%

1.6 The Interplanetary Magnetic Field (IMF)

The magnetic field permeating the solar wind originates in the Sun. These field lines are commonly viewed as being dragged away from the Sun by the plasma through the concept of 'frozen-in flow' (Appendix 1 of Lemaire and Roth, 1991). The idea of this is that the magnetic flux through a certain volume of plasma is constant in time¹,

¹ Constant flux through a plasma element follows from the assumption that it is a highly conducting medium. As the conductivity tends to infinity, Ohm's Law requires that the total electric field (electrostatic plus convection fields) tends to zero, for a finite current to flow, i.e. $\mathbf{E} + \mathbf{v} \times \mathbf{B} \rightarrow \mathbf{0}$. In a frame moving with the plasma ($\mathbf{v} = \mathbf{0}$) this implies that the electric field must be everywhere zero. Faraday's Law of electromagnetic induction then requires that the rate of change of magnetic flux is also zero (since $\text{curl}(\mathbf{E}) = 0$). This is a good approximation for the highly ionised plasma of the solar wind, but can not be applied in the ionosphere, where the conductivity is much lower.

which is commonly pictured as the magnetic field lines being fixed in the volume of plasma, and thus moving with the bulk plasma flow.

Due to the Sun's rotation, one end of a magnetic flux tube is being rotated (one revolution in about 27 days; although this period depends on the solar latitude of the flux tube's origin!). This tube is "frozen" into the plasma which is moving radially, causing the interplanetary magnetic field, in the Sun's equatorial plane, to be inclined at an average of 45° to the tangent of the Earth's orbit. The component of the IMF perpendicular to this plane (the northward or B_z component) averaged over a long period of time, is approximately zero, but large deviations from this exist. This component of the IMF plays an important role in the transmission of the solar wind's kinetic energy into the magnetosphere.

1.7 The Magnetosphere

Before the discovery of the solar wind, and IMF, it was believed that the near-Earth magnetic field resembled an ordinary dipole field. This field is believed to originate from electrical currents flowing in the molten magma below the Earth's solid crust.

It is now known that the dipole approximation fits quite well close to the Earth, but becomes progressively worse with distance. Major distortions are caused by the pressure of the solar wind (as well as smaller modifications due to currents flowing in the near-Earth environment, and a static field associated with permanent magnetism in ferromagnetic rocks of the Earth's crust).

The solar wind compresses the volume of space dominated by the Earth's magnetic field (the magnetosphere) on the day side of the Earth. It also stretches the magnetosphere into a long 'tail' behind the Earth, which may extend for more than 1000 Earth radii.

The boundary between the magnetosheath and the magnetosphere is termed the magnetopause. It may be situated at altitudes of 10 Earth radii (64 000 km) in the sunward direction.

1.8 The Solar Wind - Magnetospheric Dynamo

When charged particles move perpendicular to magnetic field lines, they experience a Lorentz $\mathbf{v} \times \mathbf{B}$ force. This acts in opposite directions for electrons and positive ions, producing a net charge separation. This charge separation can be viewed as a difference in electrical potential between the two sides of the streaming plasma. The process is that of a magnetohydrodynamic (MHD) power generator or dynamo.

It is often argued that such a MHD dynamo effect is responsible for setting up an electric field from the dawn to dusk side of the magnetopause, although the process for producing this field remains controversial. The epsilon parameter (Perreault and Akasofu, 1978), gives an empirical relation between the power generated by this dynamo, and the solar wind's velocity, magnetic field, and polar angle between the IMF and the northward direction. This parameter shows a good correlation with the observed potential across the polar cap (Reiff *et al.*, 1986), and is an indication that the essence of idea is correct.

The traditional views of the coupling between the magnetosphere and the solar wind describe the process as being due to 'viscous-like interaction' or 'magnetic reconnection' (first proposed in 1961 by Axford and Hines, and Dungey respectively). In these theories, the efficiency of energy conversion from the kinetic energy in the solar wind, to electrical energy in the magnetosphere is highly dependent on the IMF. Lemaire

and Roth (1991) argue that similar results are obtained through ideas involving 'impulsive-penetration' of the magnetopause by distinct patches of plasma (plasmoids), without requiring the application of 'ideal' magnetohydrodynamic (MHD) principles. In their theoretical work, the injection of plasmoids into the magnetosphere, and the associated power input and cross polar electric field developed, are still strongly linked to the orientation of the IMF.

Whatever the precise details of the mechanism, measurements indicate a direct link between the power entering the magnetosphere, and auroral activity, see Siscoe (1991) for a review of factors affecting the size of the auroral oval.

1.9 The Ionosphere

The power input to the magnetosphere seems to have a direct effect on the production of aurora, but electric fields generated at the magnetopause at an altitude of greater than 60 000 km are far removed from the observed auroral displays at about 100 km. In the latter height region, called the ionosphere, the plasma environment differs greatly from that considered before. As indicated in Table 2 the ionospheric plasma is a lot denser and cooler than other plasmas in the near-Earth environment. This is indicative of the fact that the ionosphere marks the interface between the neutral mesosphere, and the highly ionised exosphere.

Figure 3 shows how the density of electrons (equal to the plasma density) , varies with altitude. It also illustrates the effects of solar activity, both on time scales of one day, and over the 11 year solar cycle. The main source of these electrons is from the ionisation of atmospheric neutrals by short wavelength radiation from the sun. The neutral components of the ionosphere are only shown for heights above 400 km because at lower heights the numbers are too large to fit on the graph. This highlights the fact that although the ionosphere is a plasma, it is only a weakly ionised one, and although it has many properties of a plasma, the neutrals must not be neglected.

In fact, below about 130 km, collisions between ions and neutrals dominate, whilst electron collisions are much rarer. This means that winds in the ionosphere can transfer momentum to ions through collisions, and move them perpendicular to magnetic field lines (or vice versa), which, since the electrons are largely unaffected by this process, produces a current flow (or resistive heating of the ionosphere).

The occurrence of neutral winds in the troposphere (lowest 10 km of the atmosphere) is the result of pressure gradients combined with Coriolis acceleration due to the Earth's rotation. The pressure gradients are a result of differential heating of the atmosphere. In the auroral ionosphere these winds are mainly horizontal , and are produced not only by solar radiation, but also by the direct influx of particles from the magnetosphere, and heating from the flow of large currents in the ionosphere. It should also be mentioned that over long periods the atmosphere exhibits vertical oscillations, due to waves in the atmosphere, tidal and seasonal effects. These will alter the general height at which aurora are observed, but should have little effect over the timescales of individual arcs.

In short then, although the 'blackbody' radiation is the dominant source of energy from the Sun, it plays a minor role in the production of the aurora.

1.10 Magnetosphere-Ionosphere Coupling

How is the electrical power at the magnetopause transmitted down to the ionosphere? The first theories for the coupling mechanism were published in 1908 by Kristian Birkeland. His idea was that currents flow along magnetic field lines into and out from the polar regions. These currents are now known as field-aligned or Birkeland currents.

The large-scale distributions of Birkeland currents have been well mapped by satellite measurements on the basis of magnetic field measurements. Although it is not possible to uniquely define electric current configurations from satellite magnetometer results (more will be said about this later), the large scale results are hard to explain in other ways, and the results fit other measurements (see Potemra, 1987 for a review).

It is apparent from these observations that many different types of current system can exist (Potemra, 1993, distinguishes six main classes), of which two distinct configurations are dominant. One is during extended periods of northward pointing IMF. This is known as the NBZ (northward Bz) system, and results in aurora being present right across the polar cap. This is an occurrence of much lower power conversion by the magnetospheric MHD dynamo, and will not be considered further here (Ijima, 1984).

The other main current systems are the region 1 and region 2 systems shown in Figure 4. These currents appear to be driven by the MHD dynamo. Particle measurements indicate that the majority of the current is carried by electrons moving in helices along magnetic field lines, although at least part of the current is usually carried by positive ions as well.

The most common way of viewing the source of these field aligned currents is to view them as necessary for current continuity, where the current perpendicular to the magnetic field is given by the MHD equation:

$$\mathbf{J}_\perp = \frac{\mathbf{B}}{B^2} \times \left[\rho \frac{d\mathbf{v}}{dt} - \rho \mathbf{v} \nabla \mathbf{v} + \nabla P_\perp + (P_\parallel - P_\perp) \frac{(\mathbf{B} \cdot \nabla) \mathbf{B}}{B^2} \right] \quad (1.1)$$

where:

\mathbf{J}_\perp = current density perpendicular to the magnetic field

B = magnetic field strength \mathbf{B} = magnetic field

s = distance along magnetic field line

ρ = plasma mass density

\mathbf{v} = dynamic viscosity of plasma

P_\parallel = hydrostatic pressure parallel to the magnetic field

P_\perp = hydrostatic pressure perpendicular to the magnetic field

\mathbf{v} = bulk velocity of plasma

and the terms on the right hand are usually referred as drifts due to:

- inertia (or polarisation)
- viscosity
- diamagnetic or pressure gradient

- gyromotion (or gyro orbit crowding)

respectively, see Vasyliunas (1984) for derivations.

From this, and one of the Maxwell Equations, it can be seen that :

$$\nabla \cdot \mathbf{J}_\perp + B \frac{\partial J_\parallel}{\partial s} = 0 \quad (1.2)$$

J_\parallel = current density parallel to the Earth's magnetic field, and we have assumed that:

$$\nabla \cdot \frac{\partial \mathbf{E}}{\partial t} = 0 \quad (1.3)$$

i.e. the divergence of the rate of change of the electric field ("displacement current") is zero.

As Vasyliunas (1984) stresses, there are two important ideas to bear in mind when applying these equations. Firstly, a current may flow at any point within a plasma. Although the magnetospheric current systems are often likened to electrical circuits, this analogy is only valid for the large scale effects. On a smaller scale, it is the fact that currents are not restricted to flowing along fixed paths in space, that makes explaining how the flow inside a planet can set a magnetic field so much harder than explaining the field due to a solenoid.

Secondly, the separate terms in Equation (1.1) are given names only as a guide to the mechanism by which they are produced. In the general case where currents are produced by a number of effects, there is no way, solely through measurements of the currents, to determine the relative importance of each mechanism. Similarly, point measurements of current flow, are not sufficient to accurately distinguish between possible source regions for the currents.

With these caveats in mind we proceed to draw a current circuit analogy as a means of representing the overall effects.

1.11 Region 1 Currents

The electric field set up across the magnetosphere, will tend to cause the flow of current from dawn to dusk across the tail region. It will also cause an $\mathbf{E} \times \mathbf{B}$ drift motion of the plasma in the neutral sheet (Section 1.12). This bulk flow is directed sunward, causing a shear at the magnetopause, where this plasma meets the solar wind plasma flowing away from the Sun. This boundary region is viewed as the source region for the region 1 field-aligned currents connecting to the ionosphere, although there is some doubt over the exact position of the current generation (see Potemra, 1994, for a review). Thus if, bearing in mind the discussion above, any finite volume can be defined as the origin of these currents, it appears that under different conditions they show signatures of originating from a number of the different layers depicted in Figure 5.

The region 1 currents then can be represented as flowing from the magnetospheric dynamo, along magnetic field lines, down to the ionosphere. The plasma here has a low density, so these currents can be viewed as the motion of electrons (ion flow being of minor importance due to their greater mass (Newell *et al.*, 1991)) along helical paths around magnetic field lines. The electric potential produced in the magnetosphere can also be transmitted down to the ionosphere.

Before proceeding to describe the region 2 currents it is necessary to look at some of the other currents flowing in the near-Earth environment

1.12 The Neutral Sheet Current

As described above, the tail of the Earth's magnetic field has a potential from dawn to dusk. This combines with the north - south component of the magnetic field resulting in a convective drift of the plasma towards the Earth (i.e. sunward).

In addition to this bulk flow, a current flows perpendicular to the magnetic field (i.e. across the tail). This current is a result of the terms on the right hand side of Equation (1.1). It flows in a thin sheet around the symmetry plane of the tail, named the plasma or neutral sheet. In this region the magnetic field lines have components oriented in the direction towards the Earth above the sheet, whilst below it they point away. Near the Earth, these lines are continuous (or closed) and approximate a dipole field. Far into the tail, the large scale current flow is as shown in Figure 6. This indicates that the current flows around two large rings, (cylinders in three dimensions), which behave as solenoids. The flow direction is opposite in the two rings, resulting in the production of anti-parallel magnetic fields (which are joined at great distances from the Earth). In the central region the fields tend to cancel producing a null or neutral magnetic field. This is the origin of the name of the neutral sheet.

1.13 The Ring Current

On closed magnetic field lines the dominant motion of charged particles is an adiabatic bounce motion between magnetic mirrors in the northern and southern hemispheres. On top of this, the curvature of the magnetic field lines produces a drift of the particles, both because of the magnetic field gradient, and the centrifugal force associated with curvature of the guiding centre path (inertial effects). This is in opposite directions for electrons and ions, and represents a current flowing around the Earth. This is the ring current.

1.14 Region 2 Currents

The region 2 currents flow in the opposite direction to the region 1 currents, and are always displaced slightly equatorward (Figure 4). It is believed that while the region 1 currents are produced directly by the magnetospheric dynamo, the region 2 currents are the result of divergence of the ring current (Figure 5), caused by plasma pressure gradients (Potemra, 1994).

1.15 The Auroral Electrojets

Referring back to the circuit analogy, we have seen how an electric potential can be set up (as in a battery), and how that electric field may be transmitted to another place (e.g. as along conducting wires), but not how the electrical energy is dissipated. In order for current to flow a connection must be made to complete the circuit. This is provided in the form of a resistive material (a load); the ionosphere. The potential (of the order of 100 kV) from dawn to dusk tends to cause plasma flow across the polar cap. However this is not a flow, as may be expected, so that current flows from dawn to dusk, but, due to the magnetic field permeating the polar cap, is an $\mathbf{E} \times \mathbf{B}$ drift. This means that the plasma as a whole is convecting away from the Sun.

As mentioned in the discussion of the ionosphere, it is not always true that the ions and electrons in the plasma will move together. At lower altitudes the ion collisions result in the ions moving in the direction of the electric field, whilst electrons still follow their $\mathbf{E} \times \mathbf{B}$ drift. The results of this are:

- a current from dawn to dusk due to the ions, and
- current toward the sun, across the poles, due to the electrons.

The above describes how the region 1 currents close, but remember that there also the region 2 currents flowing in the opposite direction. Since the ionosphere is a resistive medium, consideration of Figure 4 will show that current can flow from the region 1 zone to the nearby region 2 current, thus creating an electric field pointing equatorward in the morning side, and poleward in the evening side. The $\mathbf{E} \times \mathbf{B}$ convective plasma drift is thus sunward in both sectors of the auroral oval. Again, at low enough altitudes (high enough densities), this results in electrons carrying a current. In this case it flows towards the night side, and is called the westward electrojet in the evening side, and the eastward electrojet in the morning. This is illustrated in Figure 7.

It is magnetic disturbances caused by these horizontal flowing currents that are measured to produce the AL, AH, and AE indices used to describe geomagnetic disturbances (see Appendix 3B of Vallance Jones (1974) for a description of the different parameters used in describing auroral activity).

The flow of current around the auroral electrojet systems represents by far the greatest sink for the energy injected into the Earth system from the solar wind. The heating effect of the collisions between this flowing plasma and the neutral atmosphere, produce large scale winds. These winds have been shown to have little effect on the flow of field-aligned currents (Lyons and Walterscheid, 1986).

1.16 Particle Precipitation and the Aurora

Having given a description of the energy source for the aurora, it is now possible to consider the direct cause of the lights seen to shimmer across the sky. Early studies of the auroral spectrum indicated a wide variety of lines, but in 1925 McLennan and Shrum managed to identify the dominant 557.7 nm radiation as being due to a forbidden transition of electrons in oxygen atoms. Further studies indicated that the spectral lines observed could be explained by the excitation (and subsequent decay) of atmospheric components, by electrons with energies of the order of 10 keV.

The excitation is created when electrons of the right energy collide with the atmospheric ions, atoms and molecules. The colour the aurora produces depends on which species is excited, which is determined by the height at which the electrons release their energy. This is due to the fact that the composition of the atmosphere varies rapidly with height in the ionosphere, due to lack of vertical mixing, and the chemical reactions produced by the large amount of ionising UV radiation.

The electrons, as confirmed by *in situ* particle measurements, precipitate into the atmosphere in the regions of upflowing current. The depth to which they penetrate the ionosphere depends on their energy, and on their pitch angle (angle to which the helical motion along magnetic field lines is inclined to the magnetic field direction). Electrons with too large a pitch angle will not reach the ionosphere, due to the magnetic mirror effect.

As the electrons reach denser parts of the atmosphere, they will start to be scattered, and lose energy. Since the collision cross-section for exciting atmospheric species increases with decreasing energies, the electrons will not undergo such a collision until their energies have been decreased sufficiently. It is during this non-collisional slowing that the electrons emit X-rays as Bremsstrahlung.

1.17 The Auroral Potential Structure

Although early particle measurements confirmed the existence of field-aligned currents, and indicated their relationship to the aurora, they also raised certain questions. It appeared that the electrons at high altitudes did not have either the correct energies, or the correct pitch angle distribution, to reach the heights measured for discrete auroral arcs. This discrepancy is now believed to be due to the existence of magnetic field aligned electric fields, at altitudes of between 10 000 km and 20 000 km, which accelerate the particles and change their pitch angle, producing beams of near mono-energetic electrons (Burch, 1991).

The exact form of this auroral potential structure is as yet unknown, and a number of different theories exist as to its method of production (Fälthammar, 1991). It is believed that such potential structures are only formed when the influx of energy from the solar wind exceeds a certain (variable!) level. This occurs mainly during the events known as auroral substorms.

In the absence of formation of these acceleration zones, there still exists an aurora, although much less intense than the arcs observable with the eye. This is the diffuse aurora and occur in regions of upflowing current, associated with the wide background level of the electron spectra, rather than with mono-energetic beams (Lyons, 1991). The occurrence of the diffuse aurora at various levels is shown in Figure 8.

1.18 Discrete Aurora

The intense curtains, and arc structures (collectively referred to as arcs), are associated with accelerated electrons precipitating into the atmosphere. Most auroral activity of this type is associated with the auroral substorm (Akasofu, 1991). As shown in Figure 9 (Friis-Christensen and Lassen, 1991), the statistical probability of occurrence of discrete auroral arcs is greatest in the area of the ionosphere corresponding to region 1 field-aligned currents during these times.

For a description of the features, and a precise definition of the auroral substorm see Rostoker (1987). This also discusses the issue of whether the energy input from the solar wind is transferred directly to the ionosphere, or whether it is stored in the tail region for release at some later time. This relates to the precise mechanism of the substorm, theories of which are presented by Rostoker (1991).

1.19 Summary

The simplified view of the aurora presented here, is that it is produced by the precipitation of accelerated electrons in the field-aligned current regions. These currents are the results of the interaction between the Earth's magnetic field and the solar wind. Figure 10 (from Akasofu, 1991) summarises the interaction and feedback between the different components.

However, there are a number of fundamental problems still to be solved in forming a successful theory of the aurora, as indicated in the following quotes from 1991:

i. [It is necessary to find a satisfactory solution...] To find the physical processes through which energy is able to penetrate inside the magnetopause, providing the energy whose visible manifestation is the aurora. (Rostoker, 1991)

ii. The problem of mapping auroral oval features such as discrete luminous forms (arcs, bands, inverted-Vs) that are excited by accelerated and highly structured electron beams from the outer magnetosphere is still one of the key problems in the physics of geospace. (Galperin and Feldstein, 1991)

iii. A crucial problem in auroral physics is how the auroral primaries are accelerated to their observed energies. (Fälthammar, 1991)

2 The Auroral Turbulence Mission

"The primary scientific objective is this mission is a comprehensive investigation of the variations, in time and space, of the plasma physical properties occurring within and around a strong auroral arc."

The above quote is taken from the Flight Requirements Plan for Black Brant XII 40.005 UE, the payload of which was designated Auroral Turbulence. In realising these objectives, three characteristics of the mission are prominent

- i. A sounding rocket flight through an auroral arc
- ii. Launch during an auroral substorm
- iii. Three sub-payloads, to separate to a distance of 6 km.

2.1 Sounding Rocket Flights

Auroral research, and associated topics in space plasma physics, proceed through a number of different techniques, involving theoretical work backed up by experimental results. The experiments performed range from laboratory work to active rocket experiments, in attempts to understand the mechanisms at work in space plasmas, as well as direct measurements of naturally occurring phenomena. The earliest example of how *in situ* measurements of space plasmas have influenced our understanding of the plasma state, was the discovery of the trapped radiation around the Earth (Van Allen belts). Such measurements are essential today for discriminating between different theories developed to explain the behaviour of plasma on scales too great to be simulated in laboratory experiments.

In situ measurements are performed by both satellites and sounding rockets, both of which have their advantages. Satellites are able to collect data which can be used for measurements of large scale structures (e.g. through global imaging), and for investigating effects occurring at large distances from the Earth. They are able to operate for extended periods of time, and are therefore essential to statistical studies of the aurora.

On the other hand, the visible aurora is produced at low altitudes, specifically at altitudes where the atmospheric density is sufficient for collisions between electrons and ionospheric particles to become significant. By its very nature then, the environment of the aurora severely limits the use of satellites in this region; low altitude satellites have short lifetimes due to atmospheric drag and degradation of materials. Although rockets have still shorter lifetimes, they can expect to collect reasonable amounts of useful data. This is because the flexibility in launch time makes it easier to ensure that they pass through the region(s) of interest. Thus, the reduced cost of developing instruments for short operational lifetimes, and the savings in launch costs compared to satellites, are benefits obtained without significant decrease in the amount of useful information obtained.

Another advantage of rockets over satellites is the improved resolution due to the lower velocity of the sensor platform. To remain in orbit requires a velocity of around 8 km/s, compared to around 1 km/s for a ballistic flight to heights of more than 300 km. To put this another way, an instrument sampled at 50 Hz (i.e. the data presented in this report), can resolve down to about 160 m on a satellite, compared to around 20 m on a rocket. With arc structures having scale lengths down to 100 m the benefits of this are obvious.

2.2 Auroral Substorms

As mentioned in the introduction, the most intense auroral arcs generally occur during auroral substorms. This is a just one manifestation of larger scale disturbances known as magnetospheric substorms. Contemporary theories of substorm behaviour distinguish between increases of auroral activity caused by a direct increase in the energy entering the magnetosphere from the solar wind, and the release of energy stored in the magnetosphere. These theories will not be discussed in any detail here, but it is necessary to consider the effects attributed to each process.

The directly driven component of a substorm produces an expansion of the auroral oval towards the equator, due to increased energy dissipation in the oval. The electric field across the ionosphere is increased, as is the ionospheric conductivity due to increased electron precipitation and ionisation of neutrals. These two effects result in greater current flow in the auroral electrojet system, which may be measured on the ground as an increase in the AE index. Such disturbances typically last around six hours, after which time the auroral oval has returned to its original size. These events appear to be correlated to the northward component of the IMF, such that a change from north to south initiates the substorm, and its end occurs about an hour after the IMF changes back to pointing north again. Note that the inductance of the magnetosphere-ionosphere coupling system introduces a delay between events in the magnetosphere, and their observed effects on the ionosphere.

Within the substorm are disturbances on a time scale of about an hour, which manifest themselves in the activity of the discrete arcs at the poleward edge of the oval. This is usually linked to the unloading of energy from the tail region of the magnetosphere, and has been termed a 'multiple onset substorm'. The characteristic signatures are shown in Figure 11 (Akasofu, 1964). These changes in the auroral intensity, distribution and type were originally called auroral substorms by Akasofu based on results from the International Geophysical Year (1957/58), but more recently this term has come to encompass a wider range of effects. The terminology for all these processes is somewhat confused, owing mainly to misinterpretation of the various events in the past. Rostoker *et al.* (1987) give a good description of how the old terminology relates to current theories.

Figure 11a shows the general distribution of discrete auroral arcs before the beginning of a breakup event. The first indication of its development is the brightening of the most equatorward arc in the late evening sector. This travels poleward at speeds of a few hundreds of metres per second. Simultaneously, this arc starts to twist into a wave like structure which appears to move westwards; this is traditionally called the westward travelling surge. The arcs in the morning sector have a tendency to break into small regions of 'patchy' aurora. About 30 minutes after the onset of this breakup, the poleward expansion of the region of discrete arcs subsides, and the system returns to its pre-breakup state. Breakup events such as this may occur at any time within the substorm, but are often associated with the peak of the current flow in the electrojets.

The Auroral Turbulence rocket, was launched from Poker Flats in Alaska on March 9th, 1994 at 0821 UT. This corresponds to 2321 magnetic local time. The flight was directed approximately north (Figure 12a), and was timed to occur with the start of an auroral breakup event. Thus, the rocket flew through an arc which was very strong, and moving in the same direction as the rocket, at speeds of several hundreds of metres per second.

2.3 Problems Associated with Rocket Magnetic Field Measurements

Magnetic fields (**B**) are the product of a relativistic transformation of the force due to electrical charges and may be viewed, by consideration of the terms in the Maxwell equation

$$\frac{1}{\mu_0} \nabla \times \mathbf{B} = \mathbf{J} + \epsilon_0 \frac{\partial \mathbf{E}}{\partial t} \quad (2.1)$$

to be due to either current flow (**J**=current density) or time variant electric fields (**E**). Even in the case where one of these two terms can be neglected, point measurements of the magnetic field are still not enough to remove ambiguities remaining due to the fact that the curl operator is three dimensional. Assuming the time variation of the magnetic field is small, a rocket's motion through the field can give the information for the field variation along a line, but this is still not good enough to determine three dimensional structures. There is also a problem that with both the sensor and the auroral arc moving at high speed, it is very difficult to distinguish between spatial and temporal variations.

Hence, for this flight three payloads were selected to fly in a triangular formation. The three payloads were given the names Mother, Daughter and Baby, and were intended to have separated from each other by 120 seconds from launch. Unfortunately a number of problems occurred resulting in the failure of separation of Baby from Daughter (although they did both detach from Mother). Some data from Baby and Daughter were still collected, but are not covered by this report.

There exists a further significant problem with rocket borne magnetometer measurements. This results from the fact that the disturbances related to auroral arcs are of the order 10 nT compared to a background field of around 50 000 nT. This low signal-to-noise ratio is compounded by the fact that the rocket is rotating during the flight. This angular motion results in an oscillating signal in the magnetic field measurements. Even if the background field is known, its effects on the data must also be compensated for by correcting for these rotations.

The accuracy requirement for this attitude determination is very high. A misalignment of an axis by only 2×10^{-4} radians (0.01°) will reduce the signal-to-noise ratio to unity. For the Mother payload, this kind of accuracy was achieved by the on-board attitude control system (ACS) measurements of the rocket as a whole. For the other payloads, no such system was available.

2.4 Overview of the Data Reduction

Section 2.3 introduced some of the benefits of sounding rocket flights, and also the problems associated with magnetic field measurements. The bulk of this report deals with a technique for attitude determination for the sensor, using only magnetic field measurements. The reduction of magnetometer data described here is based on the fact that the background magnetic field changes little over the characteristics times of the payload's attitude changes. Hence this field can be used to define a reference direction for the orientation of the payload. In fact, before going into free flight the rocket ACS is used to align the payload with its z-axis approximately parallel to this field.

With this in mind, the small fluctuations associated with arc structures can be viewed as *noise*, with the *signal* being related to the motion of the payload. The form of this relationship is considered in the following section.

Note that although the ACS determines the rocket attitude, the relation between the sensor and the rocket is not necessarily known with sufficient precision. Although not strictly necessary for the Mother payload, the technique presented is generally applicable to other payloads (such as Baby and Daughter), and aims to provide an improvement over the ACS results.

3 Rocket Dynamics

The flight of the Auroral Turbulence rocket reached a maximum altitude of just over 440 km. At these heights the atmosphere is very thin, so to a first approximation, the payload is undisturbed by external forces. This assumption will be discussed in the following sections.

It is also assumed that the payload behaves essentially as a rigid body and undergoes only minor flexing motions. This is a bit harder to justify for Auroral Turbulence than for most sounding rockets. The main reason for this being the Faraday Ring Ammeter (FRA), a ring of optic fibres, almost ten metres in diameter, deployed around the rocket's spin axis. This experimental device aimed to measure the magnetic flux through the ring by its rotation of polarised light (Faraday rotation). As will be discussed later, the deployment of the FRA had a major effect on the motion of the rocket, and there is evidence for it continuing to oscillate throughout the flight. However, the results indicate that this is a minor effect, and so the rigid body approximation is not a bad starting point.

The following discussion is aimed mainly at the period of the flight between about 270 and 300 seconds after launch. The reason for this is that it was during these thirty seconds or so that the rocket was crossing an arc structure.

Figure 13 shows results from an Electron Spectral Analyser (ESA) carried on board Auroral Turbulence. The measurements show clearly that the detector passed through two regions of highly energetic electron precipitation. These are assumed to be correspond to arc structures. The horizontal streaks on the plot, are believed to be artefacts introduced by the instrument's power supply (Peria, private communication). Although the intention had been to fly through a northward moving arc, the launch was made slightly early, and the first arc structure was encountered before all the systems had been properly deployed. In particular the FRA was not fully deployed until a flight time of 234 seconds, whilst the first arc traversal ended at around 230 seconds.

Due to the disturbing effects of FRA deployment, the first arc shall not be considered in this report, which is directed at obtaining good results for the period of the second arc.

3.1 Rigid Body Motion

Rigid body motion, when no torques are acting, is quite a simple problem to solve. The motion can be split into two parts;

- The translation of the centre of mass.
- Rotations around the centre of mass.

3.1.1 Translation of the Centre of Mass

From Newton's Second Law of motion, with gravity the only force acting, and that assumed to exert a constant force, the payload will move with the familiar parabolic trajectory.

Figure 12 shows plots of the position of the rocket during the flight, from ground based radar measurements. The altitude plot (Figure 12b) shows clear changes of climb rate associated with rocket burns (Taurus 24.0 to 27.5 seconds, Black Brant 33.0 to 65.4 seconds, and Nihka 92.0 to 110.6 seconds). Following the Nihka separation at 119.0 seconds after launch, the payload followed an approximately paraboloidal trajectory from

around 100 km up to a maximum altitude of 440 km. The arc interception occurred in the height range, 385 to 410 km.(Figure 14, lower panel).

Figure 15 shows how the flight path differs from a parabola, over varying time intervals. Near the beginning of the flight the standard deviation between the fitted parabola, and the measured data, is of the order of the noise in the measurements only over short periods of time. However, as the flight progresses, the fit becomes better over longer periods, and then worsens again near the end. This is indicative of the fact that the trajectory becomes closer to a parabola during the middle part of the flight.

A possible interpretation of this is that the flight is more nearly parabolic whilst flying at higher altitudes, which would suggest that at lower altitudes, where the atmospheric density is higher, there is more drag on the rocket.

However, for the period of interest, i.e. the traversal of the arc between 270 and 300 seconds after launch, the deviation from the paraboloidal fit is of the order of 0.5m (Figure 14, upper panel). This is not a significant error, given the obvious noise in the measurements, and it is reasonable to assume that over this period of time, the translational motion of the payload is not significantly affected by external perturbing forces (except for gravity).

Unfortunately it is not possible to estimate in this way the effects of external torques on the system, so it was assumed that they are likewise too small to cause significant effects, over short time intervals. The consequences of this assumption will become evident later.

3.1.2 Rotational motion

The assumption that no torques act on the payload, leads to the conclusion that the rotations will remain constant in time. However, this is not such a simple case as the centre of mass motion, because the payload may spin around three orthogonal axes. A simple way to treat this motion is via Lagrangian mechanics.

Consider the rocket to be cylindrical in shape so that two of its principal moments of inertia are equal (Figure 16). The three principal axes of the rocket are denoted 1,2 and 3, and the rocket is oriented at angles θ , ϕ , and ψ (the Euler angles) to the inertia frame x, y and z. In this inertial frame the angular velocity of the rocket can be written

$$\omega = (\dot{\theta}, \dot{\phi} \sin \theta, \dot{\psi} + \dot{\phi} \cos \theta) \quad (3.1.1)$$

$$\text{where } \dot{\theta} = \frac{d\theta}{dt} = \text{time rate of change of } \theta, \text{ etc.} \quad (3.1.2)$$

Defining the three principal moments of inertia to be I_1 , I_2 and I_3 where:

$$I_1 = I_2 = I_{\perp} \quad ; \quad I_3 = I_{//} \quad (3.1.3)$$

allows the kinetic energy to be written

$$T = \frac{1}{2}(\omega \cdot I \cdot \omega) = \frac{1}{2}I_1\dot{\theta}^2 + \frac{1}{2}I_2\sin^2\theta\dot{\phi}^2 + \frac{1}{2}I_3(\dot{\psi} + \dot{\phi}\cos\theta)^2 \quad (3.1.4)$$

which is equal to the Lagrangian in the absence of any potential energy terms.

Applying Hamilton's Variation Principle the calculus of variations yield the Euler-Lagrange equations

$$\frac{d}{dt} \left(\frac{\partial L}{\partial \dot{q}_i} \right) - \frac{\partial L}{\partial q_i} = 0 \quad \text{with } L = \text{Lagrangian} = T, \text{ and } q_i = \text{generalized co-ordinates} \quad (3.1.5)$$

These give the equations of motion:

$$\frac{d}{dt} (I_3 (\dot{\psi} + \dot{\phi} \cos \theta)) = 0 = \frac{d}{dt} J_3 \Rightarrow \text{angular momentum about the 3 - axis is constant} \quad (3.1.6)$$

$$\frac{d}{dt} (I_2 \dot{\phi} \sin^2 \theta + I_3 \cos \theta (\dot{\psi} + \dot{\phi} \cos \theta)) = 0 = \frac{d}{dt} J_z \Rightarrow \text{angular momentum about the} \\ \text{z - axis is constant} \quad (3.1.7)$$

If the z-axis is defined as the direction of the total angular momentum vector **J**, for the case of the symmetrical body, these equations can be simplified to:

$$\dot{\phi} = \frac{J}{I_{\perp}} = \text{coning frequency} = \omega_{\text{cone}} \quad (3.1.8)$$

$$\dot{\psi} = J \cos \theta \left(\frac{1}{I_{//}} - \frac{1}{I_{\perp}} \right) = \text{spin frequency} = \omega_{\text{spin}}$$

and conservation of energy requires that

$$\theta = \text{half-coning angle} = \text{constant} \quad (3.1.9)$$

From the above analysis we see that there are two frequencies involved in the motion. These we associated with two separate mechanisms, which we define to be spinning and coning. The former is the spinning of the rocket around its own axis, the latter the rotation of this spin axis around the total angular momentum vector (a fixed direction in inertial space due to the assumption of no external torque).

The effect of the motion of the payload, on the measurements, depends principally on the mounting of the magnetometer, as the magnetic field changes only slowly with time.

4 Effect of Rocket Dynamics on Magnetic Field Measurements

The motion of the rocket affects the measurements of the magnetic field in a variety of complex ways. To illustrate these a number of simpler situations were considered. Note that the separation of the motion into spinning and coning is purely artificial, in reality they are linked by the equations of motion, but as a means of understanding the effects on the data it is a useful concept.

In the following discussions, a number of assumptions are made concerning the motion. These are different in each section, but in all cases;

- The motion is considered from a reference frame moving with the rocket (in which the rocket has zero linear momentum).
- The background magnetic field is stationary in time.
- The magnetometer is fixed to the rocket with its z-axis aligned with the spin axis
- The rocket (and thus the magnetometer) undergo torque free, rigid body motion.

4.1 The Magnetometer

The magnetic field measurements presented here were obtained with a flux-gate magnetometer. For a description of the principles of operation of this instrument see the review article by Primdahl (1979). Three axis information was provided by the use of three orthogonally mounted sensor coils, (Primdahl, 1982).

The magnetometer was constructed to enable easy mounting on to the rocket, with the intention that the z-axis of the magnetometer be aligned as closely as possible to the long axis of the rocket. To avoid magnetic disturbances from other parts of the payload, the sensor was mounted on a rigid, telescopic boom about 1.5 metres in length, for deployment at 189 seconds after launch.

4.2 Notation

The three axes of the magnetometer form a right hand set associated with vectors x , y and z , where the z -axis is most parallel to the background magnetic field. The magnetic field measured in each of these directions (B_x , B_y , B_z) is determined by the scalar product of x , y , and z with the magnetic field vector. Defining the angles between these vectors by v_i ($i=x, y, z$) gives a measurement of the orientation of each axis, relative to the background field, which is independent of the magnitude of the field, i.e.

$$\cos v_i = \hat{\mathbf{B}} \cdot \hat{\mathbf{i}} \quad \text{with } \hat{\mathbf{B}} \text{ a unit vector in the direction of the magnetic field}$$
$$\hat{\mathbf{i}} \text{ a unit vector in the direction of the } i \text{ axis } (i = x, y, z)$$

The definition of the z -axis, that it is only small angles from the magnetic field, also requires that the other two will be almost perpendicular to this. To highlight the small perturbations, redefine

$$v'_j = v_j - \frac{\pi}{2} \quad (j = x, y)$$

4.3 Simple examples of effects on magnetic field measurements

The following sections deal with the situations where a single effect (i.e. coning or spinning) dominates the magnetic field measurements.

4.3.1 Case One: Magnetometer displaced along the coning axis, from the centre of mass of the rocket, no spinning.

Consider the measurements of the total magnitude of the magnetic field. The coning motion of the rocket will move the magnetometer from the two extreme points indicated in Figure 17. This is a total movement of 2Δ where $\Delta = L\sin\theta$. If the magnetic field changes significantly over this distance, then the coning will introduce an oscillation with amplitude

$$\Delta B = 2L\sin\theta \frac{\partial B}{\partial r} \quad ; \text{ with } \frac{\partial B}{\partial r} = \text{magnetic field gradient in the direction indicated}$$

For Auroral Turbulence, these parameters are approximately, $\theta=0.004$ radians (Section 6.3.2), $L=1$ metre, and an estimated magnetic field gradient of less than 1 nT per metre², giving an expected oscillation of the measured magnetic field with an amplitude on the order of 8×10^{-3} nT.

Based on this calculation the effect of being placed away from the centre of mass is seen to be negligible compared to other sources of error, and hence is ignored in the remainder of this report.

4.3.2 Case Two: Spinning, no coning.

Consideration of Figure 18 shows that in this case the angle v_z will remain constant at a value of $\kappa+\theta$, whilst v_x' and v_y' vary between κ and $-\kappa$. In fact v_x' and v_y' oscillate sinusoidally at the spin frequency, but 90° out of phase with each other i.e.

$$v_x' = \kappa \cos(\omega_{\text{spin}} t)$$

$$v_y' = \kappa \sin(\omega_{\text{spin}} t)$$

4.3.3 Case Three: Coning, no spinning.

In this situation, the z-axis traces out a cone, with a half angle of θ , around an axis at angle κ to the back ground field (Figure 19).

A way to represent this 3-dimensional behaviour, on a 2-dimensional surface is as follows:

Consider a unit sphere around the origin of the magnetometer, and each direction as a radial line. If two lines are separated by an angle θ , the points where these two lines intersect the sphere will also be separated by a distance θ . These lengths on the curved surface of the sphere can be mapped to a flat plane. If the angles are small, there will be little distortion. This is shown for the case of v_z , with pure coning, in Figure 20a.

²Based on the steepest gradients in the magnetic field data being about 5 nT over 0.005 seconds. At a velocity of around 1 km/second, this is a gradient of about 1 nT/metre.

In this situation it is not immediately apparent how the x and y axes will move, but it can be shown that they will trace out figures of eight around axes perpendicular to \mathbf{J} . This is shown in Figure 20b for the x -axis, where \mathbf{J}_x represents a vector perpendicular to \mathbf{J} in the average direction (over a complete cycle) of x .

It becomes quite difficult to visualise the effects of more complex motion, so as an aid, a FORTRAN program (*sim1*) was written to simulate the time-dependence of the three angles v_x' , v_y' and v_z .

4.4 Simulation of Rocket Motion

To produce the equations for this simulation, the dynamics program Sophia implemented using the Maple mathematics software, was used (Lesser, 1993). Sophia allows simple definitions of relationships between frames of reference, representation of vectors, matrices and dyads, transformations between reference frames, and normal vector operations.

The steps used in defining the equations for this simulation are shown below.

- Define a frame for the magnetometer, and in this frame the axes x , y and z .
- Rotate the magnetometer an angle ψ around the z axis (for spin motion).
- Rotate through θ about y axis (opening angle of coning).
- Rotate by ϕ about z axis, (angle to describe the time variation of the coning).
- Define the magnetic field to be in the z -direction in a frame at angle κ to the previous frame (rest frame of the rocket).
- Transform the vectors to a common frame, and find the angles v_i where $i=x, y, z$.

The angles ψ , ϕ and θ are the Euler angles discussed previously, and κ represents the angle between \mathbf{B} and \mathbf{J} .

Results from running this program, with suitable input values, are shown in Figure 21 for the cases of simple coning or spinning already discussed (cases two and three).

4.4.1 Case Four: Both spinning and coning.

Four distinct situations arise for this kind of motion, depending on the relative sizes of the frequencies and angles involved. The results of simulating these four situations are shown in Figure 22.

From these diagrams the following observations can be made, which are fairly straightforward to explain.

Effect	Explanation
v_z is independent of the spin frequency, and oscillates around κ at the coning frequency, with an amplitude of θ .	As the z-axis is aligned with the spin axis, spinning has no effect on these results. Hence they simplify to case three shown above.
v_x' and v_y' are always approximately one quarter of cycle out of phase, e.g. whilst v_x' starts each plot at a maximum, v_y' is at zero.	When purely spinning about the z-axis (case two), the x and the y axes are differentiated only by the definition of the origin in time. This produces a phase shift between the results for v_x' and v_y' of 90° since they are assumed orthogonal. Note that due to the coning, the phase shift does not remain fixed at 90° , but oscillates around this value (although it is impossible to see this in Figure 22).
v_x' and v_y' always exhibit two distinct frequencies in their oscillations, with one being dominant (having much larger amplitude).	As expected from cases two and three, both spinning and coning have an effect on these angles. The greater significance of one frequency over the other is a direct result of the choices of θ and κ . These choices were made to highlight the differences between coning and spinning (and to be representative of the values found for Auroral Turbulence in later sections).
When κ is greater than θ , the dominant frequency for v_x' and v_y' is 2.4 radians per second (i.e. $\omega_{\text{cone}} + \omega_{\text{spin}}$). In this case the angles oscillate at this high frequency, with an amplitude which changes at ω_{cone} from $(\kappa + \theta)$ to $(\kappa - \theta)$	The motion here is dominated by the spinning (since θ is so small). The results are not very different to the case of pure spinning (case two), but are slightly modified by a beating effect with the coning motion. Note that the beating affects both the amplitude and the frequency of the dominant oscillation.

When κ is less than θ , the dominant frequency for v_x' and v_y' is the spin frequency. The effect of the coning is a minor distortion of almost pure spin motion.

This results from the fact that the coning motion, although with a large half angle, takes place about an axis close to the reference direction (i.e. the background magnetic field). Thus, the angles between the reference direction and each axis are not changed much during the coning cycle, and the coning has only a minor effect.

4.5 Discussion

The four cases here indicate the effect of motion on the orientation of the magnetometer, with the assumptions made at the start of this section. This report will proceed to discuss these assumptions in greater detail, indicating that not all are applicable in the case of Auroral Turbulence. However, the angles discussed above, although central to the data reduction, are not measured directly by the magnetometer. The conversion of the magnetic field data into an appropriate form for attitude determination is discussed in Section 5.

5 Magnetometer Data Handling

Before proceeding to use the magnetometer data for calculating the motion of the rocket, a few steps were needed to get the raw data into the correct form.

5.1 Raw Data Provided

The magnetometer uses a method in which a current is fed back to the sensor, in order to cancel out the magnetic field being measured. It is the magnitude of this current that is then converted into a digital signal, in this case a 16-bit binary number. The range of the device was from -60 000 nT to +60 000 nT in each of the axes, corresponding to a resolution of

$$\frac{\text{Fullrange}}{2^{16}} = \frac{120\,000\text{ nT}}{65\,536} = 1.83\text{ nT per bit.}$$

For telemetry purposes, the 16 bits of data associated with each measurement (a word) were split into two eight bit bytes. The data received for use in this project consisted of nine compressed data files, each containing two bytes for each of the three axes, and the associated time after launch for each measurement.

Before proceeding to the discuss the processing of this signal, it should be mentioned that a number of steps were used to get the data into a more manageable form, that provided a better use of the disk space available. Also some checks were made to ensure that the data was in the form of samples taken at constant time intervals, and that missed samples were noted, and repeated measurements removed. The details of these two considerations are given in Appendices 1 and 2 respectively.

5.2 Filtering of the Data

The allocation of telemetry bandwidth for the flight allowed for sampling at 1562.5 Hz, however this far exceeds the cut-off frequency of the magnetometer. This maximum useful measurement frequency is due to delays in the response time of the feedback loop used in the magnetometer, and is estimated to be around 300-400 Hz.

Hence it was possible to filter the high frequency components from the data, and to resample at a lower frequency. The filter used was a low-pass filter with a cut-off at 50 Hz (Appendix C). The data was then resampled at 156.2 Hz, giving a much improved signal to noise ratio.

5.3 Calibration of the Magnetometer

To convert the data into properly scaled magnetic field measurements required the use of calibration information. The original calibration of the magnetometer was performed at Lovön, Stockholm, in December 1988, and gave the following calibration matrix.

$$\underline{\underline{M}} = \begin{pmatrix} 1.81937800 & 0.00000082 & 0.00001372 \\ -0.00085494 & 1.829162000 & 0.00001270 \\ -0.00182227 & 0.00066970 & 1.83133200 \end{pmatrix} \quad (5.3.1)$$

where the magnetic field vector **B** is formed from the raw data vector (**R**) by

$$\underline{\mathbf{B}} = \underline{\mathbf{M}}\underline{\mathbf{R}} + \underline{\mathbf{O}} \quad (5.3.2)$$

$\underline{\mathbf{O}}$ =vector containing the offsets of each axis given by

$$\underline{\mathbf{O}} = \begin{pmatrix} -334.444 \\ -680.003 \\ 1511.442 \end{pmatrix} \quad (5.3.3)$$

In this form the information, with the exception of the offsets, is very hard to interpret in a physically meaningful manner. To assist in this the data was transformed into the system described by (Bolin, 1994) and indicated in Figure 23 (his Figure 3).

In this case the calibration matrix given above can be written

$$\underline{\mathbf{M}} = \begin{pmatrix} -S_3 & 0 & -S_1\alpha \\ -S_3\beta & s2 & -S_1\gamma \\ 0 & 0 & -S_1 \end{pmatrix} \quad (5.3.4)$$

The values of these parameters were obtained from the originals using the routine *chang_calib*, and are shown in Table 4.

Table 4- Calibration parameters

Parameter	Ground calibration	In-flight Calibration	Standard deviation
S1 [nT/bit]	-1.831332	-1.8312	9.67x10 ⁻⁵
S2 [nT/bit]	1.829162	1.8290	2.19x10 ⁻⁵
S3 [nT/bit]	-1.819378	-1.8193	8.05x10 ⁻⁵
O1 [nT]	1511.442	1510	2.70
O2 [nT]	-680.0030	-724	2.38
O3 [nT]	-334.4440	-400	2.92
α [radians]	7.4918116x10 ⁻⁶	6.83x10 ⁻⁶	4.69x10 ⁻⁷
β [radians]	-4.6990786x10 ⁻⁴	-5.6x10 ⁻⁴	4.28x10 ⁻⁴
γ [radians]	6.9348430x10 ⁻⁶	6.4x10 ⁻⁶	5.10x10 ⁻⁶

Such a transformation results in both a reduced number of parameters specifying the calibration (the benefits of this will become apparent later), and a much easier interpretation of the values. This helps in the analysis given below, as well as giving an indication of the physical meaning of the parameters.

The offsets are of course unchanged by this simple geometric transformation. However it should be noted that to fit the notation of Bolin (1994) the offset vector was defined to be

$$\underline{\mathbf{O}} = \begin{pmatrix} \mathbf{O}_3 \\ \mathbf{O}_2 \\ \mathbf{O}_1 \end{pmatrix} = \begin{pmatrix} -334.444 \\ -680.003 \\ 1511.442 \end{pmatrix} \quad (5.3.5)$$

5.3.1 Requirement for Improved Calibration

The calibration was performed in a magnetically clean environment, whereas the rocket used for the flights was anything but. To reduce magnetic interference from the rocket itself, the sensor was placed on a telescopic boom, to be deployed 189 seconds after launch. This was done with a spring mechanism to ensure that the boom locked firmly into place.

Despite being mounted on a boom, there is still the likelihood that the rocket will affect the magnetometer. There is also the problem that the instrument drifts with time, and was transported half way around the world, before being fitted into a rocket which vibrates considerably during launch. The consequence of all this is that, for the kind of accuracy we hoped to obtain, the original calibration was simply not good enough, so some re-calculation of the calibration parameters was necessary.

This is true in general for a magnetometer, but in the case of Auroral Turbulence, the re-calibration is necessary for another reason. The original calibration was performed at the end of 1988, whilst the flight did not take place until March 1994. The intervening five years would be long enough for significant drift, but there were also some modifications made to the magnetometer whilst it was at the Wallops Island range on the East coast of the USA. It is believed that this would change all of the calibration parameters, but by how much is not known. In the absence of any better data, the original parameters must be assumed to be a reasonable approximation.

5.4 Technique for "In Flight" Calibration

The "in flight" calibration used the assumption that the 'true' magnetic field varies only slowly with flight time. To model this smooth variation, a sixth order polynomial was fitted to the magnitude of the magnetic field over the flight (*bmean*). This was done using the data from the rocket itself as a basis for the magnetic field, as magnetic field models are not sufficiently accurate for this purpose. The drawback of such a scheme is that there is no way of knowing if there exists an uncompensated offset in the magnetometer measurements. This would be a problem if the absolute value of the magnetic field was required, but as the most interest is in differences from the average level, this was not a serious concern in this investigation.

A plot of the magnitude of the magnetic field should not be affected by the orientation of the magnetometer, only by its position in the field. Hence there should be no evidence of the spinning or coning frequencies in correctly calibrated measurements. However, imperfections in the calibration will give a biased weighting to one (or two), of the axes. In this case the rotational motion of the rocket will introduce oscillations into the

measurements. These can be seen clearly in Figure 24, where the difference between the polynomial fit, and the originally calibrated data is shown in the upper panel. Note that the amplitude of the oscillations increases throughout the flight. This is assumed to indicate a drift in the calibration parameters.

The aim of the re-calibration of the magnetometer is to find parameters which will remove these oscillations. This was done in the routine *fit_param_amoeba*. The technique used was to minimise the summed squares of the differences between the data obtained using a vector of parameters (**P**) for the calibration, and the expected magnetic field (from the model calculated above).

5.5 Practicalities of Re-Calibration

The difficulty with implementing this idea lay in the fact that, treating the minimisation as a purely mathematical exercise, it was possible to get the best results by using the offsets to give a steady value, and reducing the sensitivities to very low levels to reduce the oscillations. Such a solution reduces the effect of the actual data, making the results more dependent on the calibration parameters. This was obviously not the intention, so a way of obtaining a local minimum in the nine dimensional space (three sensitivities, three offsets and three angles) was required. The reduction of the number of parameters from twelve (nine in the matrix plus three offsets) to nine shows significant advantages here.

This demand is somewhat different to the normal requirement for a minimisation routine where the problem is to find a global minimum, however the *amoeba* subroutine in Numerical Recipes (Press *et al.*, 1986, p.292) provided a good solution. The program forms a simplex in parameter space (the *amoeba*), which is restricted to small movements, always in a downhill direction. By starting with a simplex which is close to a local minima, and restricting the step size, it was possible to find an improved vector **P**. The initial simplex was defined so as to surround the point defined by the ground calibration.

5.5.1 Initial Conditions

It should be noted that the routine is quite sensitive to the size of the initial simplex. The method used to set up this simplex was to change each parameter from the input value, by adding or subtracting a small amount (Δ). Four different values for Δ were used in the program, one each for the sensitivities and offsets, one for the angles α and γ , and a final one for β . The reason for using a different value for β was that in the original calibration it took a value of 100 two orders of magnitude greater than the other angles. In the routine *find_param_amoeba* this is achieved by using a single input Δ for the angles, but multiplying by 100 for β .

When trying to fit nine parameters to a single function (the magnitude of the magnetic field), there are a large number of possible vectors **P** which may be considered to be solutions. The problem lies in the fact that better fits can be obtained by allowing the routine to search a larger volume of parameter space. It is not obvious how to reach a balance between the requirements to obtain a physically realistic solution, and the need to get a better fit.

Sensitivities

In the absence of any estimates for the errors expected in the calibration parameters the following approach was taken. The sensitivities, although possibly changed by the work done on the magnetometer at Wallops Island, should not change greatly. These were given a Δ of 0.001 nT/bit.

Non-orthogonality Angles

The non-orthogonality of the magnetometer is also expected to remain fairly constant, although obviously due to heating during the flight could cause small changes. The problem here is that the angles are small (5×10^{-6} rad = 1×10^{-3} degrees or the angular diameter of a 1 cm coin seen from a distance of 1 km!) and appear to be smaller than the resolution of the measurements performed by Primdahl *et al.* (1980) specifically designed to measure the non-orthogonality of this type of magnetometer. For this reason the angles were originally not included in the fitting, but it was later found that allowing small changes (around 1×10^{-6} radians) gave results not differing greatly from the original values. This allows two possible interpretations;

- The angles differ slightly from those found on the ground, and the changes are indicated by *find_param_amoeba*.
- The small changes are just random results from the motion of the 'amoeba', and indicate that they play a minor role in determining the fit to the model field.

If the former is true then the newly found angles are an improvement; in the case of the latter it appears that they are insignificant compared to the other effects. The results in Table 4 suggest that the latter is true. Either way there is nothing to be lost by using the results from *find_param_amoeba*.

Offsets

The offsets are expected to drift with time, particularly on mounting the magnetometer in the rocket. For this reason the offsets were assumed to be quite far from their ground calibration values. Originally when running *find_param_amoeba*, a value of $\Delta = 4000$ nT was used. This proved to be much too large, and a value of 500 nT was later settled on as being large enough to cover the changes, whilst speeding up the routines considerably.

It is interesting to note that while developing the routine an error occurred suggesting that *find_param_amoeba* was fairly robust with respect to starting conditions, at least as far as the offsets are considered. The results from *find_param_amoeba* were slightly odd, in that the values for the x offset returned were consistently closer to the original value for the y axis, and vice versa. On further checking this was traced to a problem whereby these had been swapped when calibrating using the ground calibration parameters. This demonstrates the fact that the routine can be used to determine the offsets if it is assumed that the knowledge of the other calibration parameters is reasonably good, independent of the starting conditions.

5.5.2 Iterative Fitting

After fitting once, the routine was repeated a number of times starting with different simplexes, although all with one vertex fixed at the point corresponding to the ground calibration, and another at the current best fit. Given that there are nine parameters, each of which can take two values (i.e. original value $\pm \Delta$), there are a total

of $2^9=512$ different initial simplexes that could be chosen. However, it was discovered that the way in which the points were chosen by the routine (based on a binary interpretation of the number of times that an initial vertex had been chosen) meant that there were rarely any changes after fitting with around 100 different vertices (10 simplexes). This was originally done as the unfiltered data was being used, and the computational effort required to run the program with a full search was prohibitive. With the factor of ten reduction achieved by filtering and resampling the data (Appendix C), a full search could be re-instated, but was not done due to lack of time.

5.6 Variation of Parameters During the Flight

Figure 24 indicates the increase in the amplitude with which the calibrated data oscillates around the mean magnetic field level. This was expected to be due to changes in offsets, which drift considerably with time. Figure 25 illustrates this in more detail, by showing the variation in time of the parameters. These results were obtained by running *find_param_amoeba* over ten second periods, starting at consecutive five second intervals, for flight times between 250 and 600 seconds.

A number of interesting features of these graphs are

- The variation of the fitted parameters increases rapidly beyond 400 seconds
- The sensitivities remain reasonably constant (with the possible exception of S_3 after 400 seconds).
- α , O_2 and O_3 show a marked decrease during the flight

The interpretation of these results is not a simple matter because of the dependence of each parameter on all of the others. However, the prior expectation that the offsets are most likely to change during the flight seems to be supported by these results.

One problem with this is that O_1 appears to be fairly constant, which would be very surprising considering that O_2 and O_3 appear to decrease by over 100 nT in the course of the flight. A possible explanation is that the apparent variation in α is an artefact produced by a real variation in O_1 .

The argument for this is simplified if considers the case where β and γ are identically zero, whence the three axis magnetic field measurements reduce to

$$B_x = -S_1\alpha R_z - S_3R_x + O_3$$

$$B_y = S_2R_y + O_2$$

$$B_z = -S_1R_z + O_1$$

In this case it is not inconceivable that oscillations due to the measurement of R_z may be removed by adjusting either O_1 or α . Since B_x is more variable than B_z (consider the amplitudes of the oscillations in the angles in Figure 22), it may be a favoured solution to reduce the effect of oscillations of R_z on B_x rather than on B_z . This could be done by varying α in preference to O_1 . This effect could be quite large given that the values of R_z are much larger than any of the others on the left hand side of the Equations (3.4.1).

Evidence suggesting that this is not too far from the truth can be seen by comparing the results for O_1 and S_1 . The shapes of the two plots for these parameters are similar, in that peaks in S_1 are accompanied by troughs in O_1 , and vice versa.

Remembering the definitions of the offsets (Equation (5.3.5)), this correlation is somewhat surprising, but can be explained by their association in Equation (5.4.1).

Attempts to confirm this relation have, unfortunately been able to confirm or disprove this is a explanation. *Find_param_amoeba_3* was an attempt to detect a variation of O1 by fixing the sensitivities and angles at average values from *find_param_amoeba*, and only doing the fitting for the offsets. This failed, only producing results like Figure 25b, but with larger random variations.

Find_param_amoeba_12 was an attempt to introduce three more parameters to allow for a linear variation in the offsets, and include this in the fitting by trying to get a good result for a longer time period. Not much time was spent on this, but the results were not encouraging.

5.7 Estimate of Errors Caused by Miscalibration

Given that a good solution for the calibration was achieved, it was decided to take average values for the parameters found over a reasonably short period, to try and eliminate the problems associated with their time variation. The size of this period was decided, rather arbitrarily, to be 60 seconds. Given that the arc was encountered between 270 and 300 seconds, this allows results to be obtained over twice this time period. It may have been better to chose a shorter period centred around the arc encounter, but by using a longer period it was hoped to get a better solution for the dynamics of the rocket. The argument used for this was twofold,

- During the arc traversal the *signal* due to the motion is affected by greater *noise* (during to the aurora).
- Considering the problems with trying to determine the parameters at a single point it was hoped that investigating the way they changed over a longer period could yield more reliable results, i.e. increase the signal-to-noise ratio by averaging the results.

The results from these, along with estimates of the errors (obtained by determining the standard deviations of the measured values from the mean value in the routine *plot_fpam_out*) are shown in Table 4

5.7.1 Effects of Offsets and Sensitivities

Assuming that the axes are orthogonal, and that at a given point the background field is 50 000 nT (B_{Earth}) with an angle between the z-axis and the magnetic field of $v_z=10^{-3}$ rad. The x and the y axes are assumed to be aligned so that they measure equal components of the field. Denoting these measured quantities as B_x , B_y and B_z

$$B_z = B_{\text{Earth}} \cos(v_z) \quad (5.7.1)$$

$$B_{\perp} = \sqrt{B_x^2 + B_y^2} = B_{\text{Earth}} \sin(v_z) \quad (5.5.2)$$

Given a raw data vector for the point, \mathbf{R} , the components of the magnetic field follow from;

$$B_x = -s_3 R_x + o_3 \quad (5.7.3a)$$

$$B_y = s_2 R_y + o_2 \quad (5.7.3b)$$

$$B_z = -s_1 R_z + o_1 \quad (5.7.3c)$$

Combining Equations (5.7.1) and (5.7.2) gives:

$$\tan v_z = \frac{B_{\perp}}{B_z} \quad (5.7.4)$$

whereby differentiation leads to

$$(\tan^2 v_z - 1)dv_z = \frac{B_z dB_{\perp} - B_{\perp} dB_z}{B_z^2} \quad (5.7.5)$$

with

$$dB_{\perp} = \frac{B_x dB_x + B_y dB_y}{B_{\perp}} \quad (5.7.6)$$

and

$$dB_i = R_i \times d(\text{sensitivity}) + d(\text{offset}) \quad (i=x, y, z) \quad (5.7.7)$$

For small v_z , the following approximations are valid

$$\frac{B_x}{B_z} \approx \frac{B_y}{B_z} \approx \frac{B_{\perp}}{B_z} \approx v_z \quad (5.7.8)$$

and

$$(\tan^2 v_z - 1) \approx -1 \quad (5.7.9)$$

giving

$$\frac{dv_z}{v_z} = \frac{dB_x}{B_{\perp}} + \frac{dB_y}{B_{\perp}} + \frac{dB_z}{B_z} \quad (5.7.10)$$

or, written in terms of the raw data,

$$-\frac{dv_z}{v_z} = \frac{-ds_3 R_x + do_3}{(-s_3 R_x + o_3)} + \frac{ds_2 R_y + do_2}{(s_2 R_y + o_2)} + \frac{(-ds_1 R_z + do_1)}{(-s_1 R_z + o_1)} \quad (5.7.11)$$

For simplicity take the three sensitivities to be the same (1.83 nT/bit) and the offsets to be, $O_1 = 1500$, $O_2 = -700$, $O_3 = -400$. Estimates for these errors are from Table 4 i.e. $\sigma_{\text{sensitivity}} = 5 \times 10^{-4}$ nT/bit, $\sigma_{O_1} = \sigma_{O_2} = \sigma_{O_3} = 2$ nT. For $B_z = -50\,000$ nT and $B_x = B_y = 35$ nT, the raw data values would be $\mathbf{R} = (-250, 420, 26500)$

Assuming that the errors are independent (not actually true, see Section 5.5), this gives

$$\left(\frac{\sigma_{v_z}}{v_z}\right)^2 = \frac{(\sigma_{s_3} R_x)^2}{50^2} + \frac{(\sigma_{o_3})^2}{50^2} + \frac{(\sigma_{s_2} R_y)^2}{50^2} + \frac{(\sigma_{o_2})^2}{50^2} + \frac{(\sigma_{s_2} R_y)^2}{50000^2} + \frac{(\sigma_{o_2})^2}{50000^2} \quad (5.7.12)$$

which, evaluated term by term is

$$\left(\frac{\sigma_{v_z}}{v_z}\right)^2 = 6.24 \times 10^{-6} + 4.00 \times 10^{-2} + 1.76 \times 10^{-5} + 4.00 \times 10^{-2} + 7.02 \times 10^{-8} + 1.44 \times 10^{-6} \quad (5.7.13)$$

This demonstrates that the accuracy of v_z is determined chiefly by the offsets of the x and the y axes, and that the fractional error that this cause for v_z is of the order of one third. In a similar fashion it may be shown that these offsets are also the major determinants in errors for their respective angles, with similar effects on the accuracy achieved.

5.7.2 Effects of Non-Orthogonality

The equations derived above, can be used to determine the effects of non-orthogonality of the axes (or rather errors in knowledge of the non-orthogonality angles), by writing the derivatives of the measurement along each axis as:

$$dB_x = -s_1 R_z d\alpha \quad (5.7.14a)$$

$$dB_y = -s_3 R_x d\beta - s_1 R_z d\gamma \quad (5.7.14b)$$

$$dB_z = 0 \quad (5.7.14c)$$

These equations then replace Equations (5.7.7)

Following this calculation through in a similar manner to above, produces an unsurprising result. The errors in v_x , v_y and v_z are related to the errors in α , β and γ by factors close to unity. Hence, for example, an error of 4×10^{-4} rad in β produces an error of about 2.8×10^{-4} rad in v_z .

6 Magnetic Field Measurements

Having calibrated the magnetometer, the next stage is to use these calibrated results for determining the attitude changes of the rocket.

6.1 Initial Observations

Figure 26 shows the magnetic field data plotted for the whole flight. This was calibrated with results from *find_param_amoeba9* averaged over the whole flight. The large disturbances at the beginning and end are of no interest, being before the magnetometer was deployed, or after the rocket had re-entered the atmosphere. Figure 27 shows the part of the flight where the magnetometer was giving useful data, and Figure 28 shows some of this in more detail.

6.1.1 Overview of the Measurements

Figure 27 shows the general trends in the measurements through out the flight, namely;

- The approximately parabolic variation of B_z (negative because the payload is oriented upwards)
- The rapidly oscillating fields (about 0.4 Hz) in the x- and y- axes, the amplitudes of which increase during the flight
- A lower frequency oscillation in the amplitudes of the 0.4 Hz oscillation in B_x and B_y . This appears at about 0.1 Hz.
- B_z shows very small oscillations at approximately 0.1 Hz.

The last three observations are shown more clearly in Figure 28, where it can also be seen that;

- B_x and B_y are approximately 90° out of phase.
- B_z also has a high frequency oscillation, at around 0.4 Hz.

These results can be translated into angles between the magnetometer axes and the magnetic field, by using the fact that the component of the magnetic field measured perpendicular to the field direction should be zero (Figure 29). For example, the magnetic field measured perpendicular to \mathbf{M} (the magnetometer z-axis) is given by,

$$B_{\perp} = \sqrt{B_x^2 + B_y^2}$$

and the requirement that the components in the horizontal plane cancel gives,

$$\begin{aligned} B_z \sin(v_z) &= -B_{\perp} \cos(v_z) \\ \Rightarrow v_z &= -\arctan\left(\frac{B_{\perp}}{B_z}\right) \end{aligned}$$

This has been done in Figure 30, where the results are shown as the three angles v_z, v_x', v_y' . From this plot some possible explanations can be proposed.

6.2 Possible Interpretation of the Results

Initially a number of assumptions were made concerning the expected results, based on other rocket experiments, which turned out to lead to an incorrect interpretation of the results for Auroral Turbulence. Although a correct solution was eventually reached, the incorrect model is presented in Appendix D as an example of the problems introduced by not taking all the data into account.

Comparison of the results shown in Figure 30 with the simulations of Figure 22 shows a number of similarities and differences. The most significant difference is that there are two frequencies present in the results for v_z , whereas simulations suggest that only the coning frequency affects this angle. Assuming for the moment that the smaller, low frequency (0.1 Hz) oscillation is of less significance than the larger oscillation, the conclusion must be that the latter is caused by coning.

The gradual increase in the mean level for v_z can then be explained in two ways,

- an increase in θ , with κ very small.
- an increase in κ , with θ smaller than κ .

Given that the approximately linear increase in this mean level continues throughout the flight, it can be seen that the second interpretation is the more likely. The first requires an opening of the coning angle (which can occur if energy is converted from the rotational kinetic energy into other forms such as heat (through friction), or oscillations of the rocket), but also requires that the angle between the background field, and the total angular momentum vector remains small through out the flight. This is less believable than the second alternative, since the rocket moves a significant distance through the magnetic field, where it is highly unlikely that the direction of this field remains fixed relative to an inertial frame. For this reason, it was assumed that κ was around 0.07 radians, and increasing, whilst the amplitude of these oscillations (about 0.008 radians) was taken to be θ .

With these values for θ and κ , how does one explain the results for v_x' and v_y' ? Again, neglecting the smaller effect (the periodic change in amplitude of the oscillations), the result is very close to that which would be expected in the case of no spinning at all. However, coning but no spinning is impossible as this violates the law of conservation of momentum. In the case where external torques act on the system this would be possible, but if the torques are small it is doubtful that the motion would differ greatly from torque free motion.. Therefore, one assumes that the result is as indicated in Figure 22c, where the dominant frequency is the difference between coning and spinning; i.e. the rocket is spinning, but very slowly.

The deployment of the FRA was known to have a major effect on the spin frequency of the rocket, so the plan was for the ACS to spin the rocket up to about 2.5 Hz before deployment. During the deployment the spinning would be slowed by the increasing moment of inertia about the spin axis, so that by the time the FRA was fully deployed, the spin frequency would be decreased to of the order of 0.5 Hz. This is not slow enough to produce the effects seen in the data (compared to an assumed coning frequency of 0.4 Hz), so the argument given above must be in error somewhere.

The other alternative suggested by the simulations is that the v_x' and v_y' results do oscillate at the sum of the spin and coning frequencies, but this time the coning frequency

is assumed to be the lower. This can be done by assuming that the largest oscillations in v_z are connected to the spin frequency, and the smaller oscillations are due to the coning.

6.2.1 Misalignment of the Magnetometer

A requirement for this model to work is a means for the spin frequency to affect v_z , contrary to the theory presented in Section 4. This is provided by the third assumption made at the start of Section 4; namely that the magnetometer z-axis is perfectly aligned with the rocket's spin axis.

It may be thought that this alignment with the spin axis (assumed to be the longest symmetry axis) could be made as accurately as the angles between the axes of the sensor. However, compared to the need to have orthogonal axes for the magnetometer, this is a much harder requirement to fulfil. The magnetometer sensor was built by a single institution (Danish Space Research Institute). The rocket contained instruments built by a number of different groups, which were mounted at separate times. Even if the shell of the rocket was built precisely enough to define a spin axis for it during flight, the addition of these instruments would have caused a small change.

The boom used for the deployment of the sensor must also be taken into consideration. It is unlikely to be completely straight, and will probably flex slightly. There is also the fact that, as will be shown, misalignment of this type is fairly easily dealt with (and hence not a critical design feature), whereas the errors in knowledge of the non orthogonality of the sensor axes will be shown to be a limiting factor in the analysis.

Finally one may question whether a spin axis can be defined at all since it relies on a high degree of symmetry for the rocket. Even if the fixed payloads were placed precisely, the fact that the FRA was only attached to the rocket at a few points, means that the optic fibre between these points is fairly free to move. With a rapidly spinning rocket this should not be a problem, and centrifugal forces will keep the fibre taut, and symmetrical. However, there is evidence to suggest that the fibres were undergoing quasi-periodic oscillations at around 2.4 Hz (Peria, private communication, 1995), which will upset the symmetry of the moments of inertia.

Assuming that a spin axis can be defined, Figure 31 illustrates how misalignment between this and the z-axis, by an angle χ , may be used to explain the results for v_z . Figure 32 shows the result of a simulation made using this angle (*sim2*). The values chosen for this simulation are so that χ is about twice as big as θ , which is the situation suggested by the results for Auroral Turbulence. The similarity with the Auroral Turbulence results (neglecting the slow increase in κ) is obvious. Note in particular how the number of short period oscillations of v_z in a ten second period is one less than that for v_x' and v_y' . This is indicative of the beating between the spinning and coning i.e v_z at ω_{spin} , v_x' and v_y' at $\omega_{\text{spin}} + \omega_{\text{cone}}$.

Misalignment in this fashion requires the use of one more angle to define it completely. Although χ represents the angle that the axis rotated by from the spin axis, it gives no information about which direction for this rotation. Another angle τ , representing how much the x and y- axes have been rotated about the magnetometer's z-axis, is required. This is illustrated in Figure 33. This angle is not immediately apparent in the data, as it just represents a shift in time for the signals. If the origin is defined to be

at a point where the spin angle ψ is zero, then correction for τ will result in the x-axis pointing directly away from the magnetic field.

6.3 Fitting of Parameters to the Data

Having described how the results may be explained, the next step is to estimate values for the angles involved in this description, in order to see how well it fits to the data.

6.3.1 Parameters Required for Fitting

In order to correct for the motion of the rocket the six angles shown below are required,

Angles	Reason
χ and τ	For the misalignment of the magnetometer (relative to rocket's z and x axes respectively).
ψ	To describe how far the rocket has spun about its symmetry axis.
θ	The half-coning angle
ϕ	An angle describing how far the spin axis has moved in the coning motion about the total angular momentum axis J .
κ	The angle between J and the field direction B

Thus, at all times, six parameters describe the state of the rocket. However, of these only χ and τ are actually constant in time. Hence, a number of additional parameters are required to define the time dependence of the other angles.

As a first approximation, it was assumed that θ was also a constant, as would be expected for free flight, when energy is (almost) conserved. The variation of κ with time was shown in Figure 30 to be approximately linear, thus allowing it to be described by two parameters. Although, for historical reasons in the development of the program for doing the fitting, three parameters were used so that;

$$\kappa(t) = k_1 + k_3(t - k_2)$$

This should not introduce any additional complications into the fitting, since the number of independent parameters is not increased, but was computationally inefficient.

The other two angles can be described by two terms each, one for the frequency of the motion, and another for the phase. In fact it would be possible to combine the two phases with τ (since they all depend solely on the definition of an origin in time). Again, this should result in computational advantages, but was not implemented for reasons of

clarity in developing the programs. Similarly, it is in theory possible to combine the spin and the coning frequencies, if the moments of inertia are known, since the ratio of these frequencies is fixed by Equations (3.1.8).

However, such a combination could not be done due to;

- Initially no data on the moments of inertia
- When the data was made available it turned out to be only approximate, in that the FRA was deployed during the measurements, but since they were performed on a non-spinning rocket, the fibre optics were simply dangling (Peria, private communication, 1995)
- This would assume that the spinning and coning are constant i.e. momentum and energy conservation

Despite the fact that the FRA was known to be oscillating, and thus likely to affect both of the frequencies and θ , these were taken to be constant over short time scales (less than a coning period), which the results will show to be a reasonable approximation.

Hence, a total of ten parameters were used for describing the six angles necessary to define the orientation of the magnetometer relative to **B**. These are summarised below;

Parameter	Reason
k_1, k_2, k_3	Linear variation of κ with time
$\omega_{\text{spin}}, \omega_{\text{cone}}$ spin and coning phase	Spin and coning frequencies and phases to define ψ and ϕ
τ and χ	Misalignment of magnetometer with spin axis
θ	Half coning angle

6.3.2 Program for Determining the Parameters (*fit_10*)

This section describes the method used for fitting the parameters defined above to the data. The basic idea was to use the same equations developed for the simulations (although note that τ did not feature in those equations, where the time origin was arbitrary, so had to be introduced, again using Sophia to perform the simple rotation). These equations were used with estimates of the parameters, to produce a "guess" of what the data should look like. The quality of this "guess" was subsequently evaluated by calculating the standard deviation between the calibrated data and the simulated results for all three angles v , and then improved iteratively.

The iteration was implemented using *amoeba*, as described in Section 5.5. The parameters being varied in such a way as to minimise the standard deviation (or rather, in practice the variance). The main problems with this were;

- This trial and error method is computationally expensive.
- If the initial guesses are too inaccurate the *amoeba* will 'ooze' its way towards an incorrect minima.

The former of these disadvantages was not deemed to be a problem, due to the finite size of the data set, and the time available for the data reduction to be performed. In addition it should be added that the programs supplied here are still in the form used for development, with no attempts made to optimise the code. Although not necessary, it is recommended that this be done if the programs are to be used in the future.

The decision to disregard the need for computational efficiency suggested a way of overcoming the second problem; that of needing to start relatively close to the solution. It was decided to run the program a number of times, initially only allowing a small number of parameters to vary at a time, until the fit was approached.

The implementation of this required maximum permissible variations of the parameters as input to the program, i.e. the Δ s described in Section 5.5.1. Reasonable estimates for θ , χ , and the frequencies can be made directly from Figure 30. Assuming that the high frequency part of v_z is due to spinning with amplitude χ , and the lower frequency part due to coning with amplitude θ , allows one to estimate values such as;

$$\theta \approx 0.005 \text{ rad},$$

$$\chi \approx 0.01 \text{ rad.},$$

$$\text{spin period} \approx 2.5 \text{ seconds } (\omega_{\text{spin}} \approx 2.4 \text{ rad/s}),$$

$$\text{and coning period} \approx 10 \text{ seconds } (\omega_{\text{cone}} \approx 0.6 \text{ rad/s}).$$

Note that the estimate of the spin frequency as being the "dominant" one for v_z in this case is actually an error. As discussed previously, it is in fact the sum of the spin and the coning frequencies, and should be corrected to $\omega_{\text{spin}} \approx 2.4 - 0.6 = 1.8 \text{ rad/s}$ above. This was overlooked the first time of running the fitting routine, yet the *amoeba* quickly realised this mistake on the part of the programmer, and approached the correct solution.

The values for k_1 , k_2 and k_3 can be calculated quite accurately using a technique such as linear regression, although in *fit_10* the routine used was the non-linear fitting routine *mrqmin* (Press *et al.*, 1986, p. 526). The reason for this was that despite being fractionally slower than other methods, it was easy to change for fitting higher polynomials (Section 6.5). This provides a good estimate for k_1 , k_2 and k_3 and it was originally believed that these parameters should require no further adjustment. However, fitting a straight to an oscillating function can result in a fitted line which passes above the mean level at one end, and below at the other, i.e. linear regression will not necessarily come up with the optimal solution in the case of non-Gaussian errors. This was demonstrated quite clearly with *fit_10*, where allowing the *amoeba* to vary k_1 , k_2 , and k_3 typically improved the fit by a factor of two. The reason for this being that the oscillatory measurements are accounted for by the other parameters, allowing the linear fit to be concentrated on the mean level (rather than being distracted by non-Gaussian errors). However, this was done as the last step of the iterative fitting, as the computer fitting routines provide better estimates than those made by eye for the other parameters.

The number of parameters remaining to be estimated has been reduced to three; τ and the phases for coning and spinning. It was not obvious how to estimate these easily, so they were input to the routine as zero, with an allowed variation Δ of $\pm 5 \text{ rad}$. This is more than enough to cover the possible range of $\pm \pi$. It was found that the routine was not that good at finding these angles, and required some forcing, by not allowing any of the other parameters to vary on the first run of *fit_10* (i.e. inputs of $\Delta=0$ for these). This

initial estimation could easily be done by hand, and may prove necessary in some cases. It is believed that it was unnecessary in this case as good estimates of the spinning and coning frequencies were available from the routines described in Appendix D.

The next stage was to allow some variation in the frequencies, with the three phase parameters already found allowed a reasonable amount of freedom (e.g. about 1 radian). It was found necessary to allow this variation in the phases as these are related to the frequencies by the time. The three phase and two frequency parameters only enter the simulation equations as three angles (ψ , ϕ and τ), so are dependent on each other and must be adjusted simultaneously to improve the fit already found..

Through out the next stages the parameters estimated so far were still allowed to change by amounts which, from experience, were deemed reasonable (Appendix E). Next the angles θ , and χ , were given some freedom, and finally k_1 , k_2 and k_3 added to the list of parameters to be fitted. The program was written so that each time it was run, the user was offered a choice of inputting the angles manually, or using the results from a file, which would then be updated with the new, improved fitting parameters. Appendix E contains results files (in a formatted form, with input parameters specified as well as outputs), obtained from running *fit_10* six times on the data between 290 and 300 seconds.

Note that the standard deviation referred to in these results, is not a true standard deviation. It was calculated using the square of the differences between the fitted curves, and the data, summed over all points, for all three angles v , and then divided by the number of points in the time period. This is therefore equal to three times the variance for each angle (assuming the errors in the fitting are the same for each angle), resulting in an error of $\sqrt{3}$ in the standard deviation. This is not a major error, as the values output from the program are still a reasonable estimate of the errors (depending on the confidence level assumed), but it should be remembered that they are calculated somewhat differently from usual, and the incorrect terminology applied.

6.4 Errors in Parameter Fitting

The data and the functions recreated using the final fitted parameters are shown in Figure 34 for the period between 290 and 300 seconds, with the difference between the fitted curves and the data, plotted in the upper panel. These show clearly the result indicated by the text in Appendix E, namely that the error in the fit is of the order of 10^{-4} radians.

Given the errors associated with the calibration discussed in Section 5, and the fact that the *noise* due to the aurora itself are of this order of magnitude, it is not believed that this routine can be made better than this, and to do so would require the addition of terms into the model which could obscure the effects of the aurora which were trying to be studied.

6.5 Extension to Longer Time Periods

In the case where the motion of the body is uniform, improvements in the calculation of the rocket motion could be obtained by using more data for the fitting (with the usual \sqrt{n} improvement in signal to noise ratio). However, the variation of parameters with time prohibits the use of this technique here, unless additional parameters are used to try and describe this variation in time.

This was attempted in a very simplistic way by introducing terms to allow higher order variations in κ , and θ (programs *fit_13* and *fit_18*). However, these did not give significant improvements over the results obtained with ten parameters. The reason for this is not clear, but may have been simply that wrong assumptions were made concerning the form of these variations, too many parameters for the fitting routine, or simply too poor estimates of this initial values

A possible improvement that was considered, but not implemented due to time constraints, was to use smaller, overlapping windows for the fitting, and then see how the parameters vary over time (in the manner of the calibration parameter fitting). Perhaps fitting functions to this variation, or using some implementation of the Kalman filter (Sorenson, 1985) would be beneficial.

Another method which may be useful would be to filter the data to remove more of the noise due to the auroral disturbances at this stage (although obviously this information will be need at the end). This should highlight the signal due to the motion of the rocket, especially if one considers time periods outside of the arc traversal, and then performs some interpolation.

6.6 Removing the Motion of the Rocket from the Data

The results produced in this project were done using 10 second windows for the fitting, at ten second intervals (with no overlap), from 250 to 320 seconds after launch. Using these parameters, the six angles were recreated at every time, and then the following rotations were performed on the magnetometer to get it into a reference frame determined by the background field. The order of doing this rotations is described in Bolin (1994) and is repeated here (c.f. Section 4.4).

Rotate by angle τ about magnetometers z-axis \mathbf{M}	To align the x-axis so that it points away from the spin axis \mathbf{S} , with y-axis perpendicular to \mathbf{x} and \mathbf{S}
Rotate by angle χ about the y-axis	Aligns magnetometer with \mathbf{S}
Rotate by angle ψ about \mathbf{S} (z-axis)	Despin the rocket
Rotate by θ about the y-axis	This aligns the magnetometer with the total angular momentum \mathbf{J} , i.e. closes up the coning angle. The rotation is about the y-axis, since the definition used for the spin phase ensures that once despun, the x-axis is pointing radially outwards from \mathbf{J} .
Rotate by ϕ about \mathbf{J} (now equal to the magnetometer's z-axis)	Removes the motion of the x- and y- axes due to coning.
Rotate by κ around the y-axis	Aligns the z-axis with the magnetic field \mathbf{B} . Again, definition of the coning phase is such that before this rotation, the x-axis is pointing away from \mathbf{B}

These rotations, are represented graphically in Figure 35. To see the effects they have on the data, *do_rot_whole_arc* plots the results obtained from each rotation. These plots are overlayed on each other, and are unfortunately not in a form that can be presented here, although the program highlights the different effects quite well.

6.7 Final Corrections to the Results

As mentioned in the previous section, results were obtained using the rough method of non-overlapping windows. Attempts to use the parameters for more than a few seconds on either side of their associated window produced rather poor results, with oscillations of increasing amplitude being introduced with distance from the period for which the parameters were originally obtained. Results after 320 seconds in Figure 36 demonstrate this (fitting of parameters was done only up to 320 seconds after launch).

Hence, it was necessary to use a different set of parameters for each window. Although the differences between these are small, they are significant, and the magnetic field measurements showed discontinuities at the boundary of each window.

These were most apparent in the y-axis data, the reason for which is not clear. To correct for these jumps of up to 20 nT in the mean level between windows, a final correction was added to the data. This assumed that the results from the first period (250 to 260 seconds), were quite accurate (as they showed small oscillations around a mean close to zero; i.e. similar to the x-axis). The jump in level for each window was then calculated by comparing the last record of one period, with the first one of the next, and this shift applied to all points in the window. This was repeated for all 7 windows from 250 to 320 seconds.

The results from this are shown in Figure 36, and before discussing the interpretation of these, a few comments should be made concerning the errors introduced by the data reduction.

6.8 Errors due to Data Reduction

Unfortunately, the technique of using ten second windows produces a number of distortions into the data. It should not be too difficult to reduce the effect of these, by the methods described in Section 6.5, but time restrictions prevented any significant progress being made in this direction.

Firstly, the gradients of the magnetic field that are commonly observed in connection with the aurora are impossible to distinguish in Figure 36. The level shifting associated with each window obscures any signal that might be present.

Secondly, any peaks or steep gradients near the edges of the windows, are quite likely to be artefacts produced by the fitting, in particular the straight line fitting to κ c.f. discussion of fitting k_1 , k_2 and k_3 in Section 6.3.2.

Thirdly, the results during the arc traversal are likely to be somewhat distorted, because the use of the magnetic field direction as a slowly varying reference is no longer such a valid assumption. In the event of "random" deviations from the field that would be present without the aurora, this should be averaged out, but the possibility of extended disturbances in a single direction will cause incorrect interpretation of the results.

If the techniques described here can be extended to account for longer time periods, it should be possible to correct for these errors, by determining the trends of the motion of the rocket outside of the arc traversal time, and then interpolating. The problem with this may be that the arc was encountered before the rocket had settled into stable motion; if such a state is ever reached during a short duration rocket flight.

7 Interpretation of Results

The results presented in Figure 36 can be interpreted from two different viewpoints; one focusing on the motion of the rocket, and magnetometer, the other looking at the aurora.

7.1 Rocket Dynamics

The fact that a good fit to the data was obtained over a complete coning cycle, with quite basic assumptions concerning the motion, indicates that on this time scale the motion is fairly stable. This would suggest that oscillations of the magnetometer boom, and the FRA (both expected to have higher resonant frequencies) are negligible. Over the 10 second periods, the fit is as good as could be expected given the problems of calibrating the magnetometer.

The difficulties in extending the fitting beyond 10 seconds could be due to one or more of the following;

- Increases in half-coning angle, due to energy loss,
- Changes in spin and coning frequencies
- Drifts in calibration parameters
- Changes in the orientation of the magnetometer relative to the spin axis.
Possibly due to differential heating and expansion of the boom, or changes in the mass distribution of the rocket.

There is not enough evidence here to distinguish between these ideas, but the changes suggested in Section 6.5 for extending the fit may yield some benefits here.

7.2 The Auroral Arc

As described in Section 2, there are a number of problems associated with magnetic field auroral measurements, one of which is the data reduction, the other is that on their own, magnetic field data are quite ambiguous.

To proceed for studies of the aurora, the rocket should be oriented into a known frame (using data from the ACS, and a magnetic field model, at one point, and then using the rotations developed here for despinning the rocket). This, if the time shift reported in Appendix C is taken into account, would allow the interpretation of the magnetic field results in a wider context.

Unfortunately, a number of setbacks meant that such an orientation of the magnetometer was not possible in the time of the project, and only a limited amount of electric field data was available. It was suggested that the magnetometer be aligned with the arc, on the assumption that rotations about its z-axis may produce a result where the perturbations of the magnetic field are almost entirely restricted to one axis. This is based on the fact that inside arc structures the perpendicular magnetic field disturbances are generally parallel to the arc, whilst electric field disturbances are across the arc.

However, given the need to perform the *ad hoc* shifts in level for the y axis data, it was felt that such a process would be quite unreliable, due to the fact that this should be done on time scales comparable to the arc crossing time.

In the absence of a means of orienting the magnetometer, it was decided to use simply the components parallel and perpendicular to the field. In fact, the measurements

parallel to the field show signals which are comparable to the noise in the data showing some correlation with the perpendicular data (Figure 37). This 'signal' is then assumed to be just due the errors in the rotations' correction for the motion (or in other words, the perturbations are too small to be separated from the noise).

There was also some three axis electric field data made available for the period between 270 and 300 seconds, although little confidence was placed in the parallel components of this data as well (Liou, private communication). For these reasons it was decided to concentrate on the magnitudes of the perpendicular and electric fields.

Figure 38 shows these results for the whole arc traversal where a few interesting phenomena can be seen;

- The electric field decreases sharply on entering the arc.
- The disturbance in the magnetic field is much greater inside the arc than outside (remember that the large increase after 320 seconds is due to the use of parameters fitted to data before that time).
- An number of peaks seem to appear in both the measurements, in particular a broad maxima between 281 and 285 seconds, and two sharp peaks shortly after 290 seconds. This interpretation is based purely on matching similar features by eye, as the times are not likely to correspond exactly between the two data sets. The reasons for this relate to their relative positions on the rocket, and the way in which they were analysed. The former because it may take half a spin period (i.e. about a second) for the electric field booms to be oriented to measure an effect previously registered by it's magnetic signature.

These observations are very dubious on their own, but comparison with other rocket flights suggests that these are significant occurrences.

In particular one should note that the ratio of electric field to magnetic field perturbations in the peaks is of similar order of magnitude to the Alfvén speed v_A . This may be estimated from the formula,

$$v_A = 2.2 \times 10^{11} \frac{B}{\sqrt{n}}$$

(Chen, 1974) where B is the magnetic field strength, and n is the electron density in cm^{-3} . At 280 seconds the electron density was estimated to be $2.5 \times 10^4 \text{cm}^{-3}$ (Labelle, in Peria, private communication). This gives an Alfvén velocity of about $7 \times 10^6 \text{m/s}$.

This should be equal to the ratio of the disturbances in the electric and magnetic fields, which can be estimated from these peaks (where one assumes they are related due to their similar shape) as shown below (see Figure 39)

Time of Peak (approximate in magnetic field data)	ΔE [mV]	ΔB [nT]	Estimate of v_A [m/s]
273.8	70	12	6×10^6
276.2	50	20	3×10^6
283.2	40	15	3×10^6
284.1	45	15	3×10^6

These values are of the right order of magnitude to suggest that the disturbances may be due to Alfvén waves, although this data is by no means conclusive, however it does suggest something to look for in the other data from the flight

8 Summary

This project has presented a technique for the reduction of sounding rocket magnetometer data. The key points to note are:

The data reduction should take notice of the data from all three axes

In the case of Auroral Turbulence the limiting factor in the measurements over a short period, appears to be the calibration.

The offsets of the magnetometer appear to drift substantially during the flight (perhaps due to heating effects).

Oscillations of the FRA and magnetometer boom appear to have a negligible effect.

The limiting factor on time scales longer than the coning period could be one of a number of effects, including loss of energy of the rocket through friction or vibration, and drift of the calibration parameters.

The motion of the rocket, over a coning period, can be described quite simply.

The coning angle in this flight was very small (about 0.2 degrees) compared to a misalignment of the z-axis with the spin axis of about twice this value

The final magnetic field data shows clearly the disturbances associated with the arc, in a direction perpendicular to the magnetic field.

There is a hint that Alfven waves may be present in the arc.

9 Further Work

The next stage of the data reduction would be to extend the fit to longer time periods, perhaps using some of the suggestions from Section 6.5. Following this the data should be transformed into a known co-ordinate system to allow investigations of the polarisation of the disturbances.

Development of a model to describe the arc, could allow estimates of the current density flowing (which could be compared with particle measurements, and the FRA data).

If Alfven waves really are present in the data it would be of interest to try and determine the distance from the rocket to the ionospheric E-layer, where waves would be reflected. This allows a calculation of the bounce time for these disturbances, which, with more information on the arc size and speed of motion, could be used to see if it was possible for the currents carried by these postulated waves to close in the ionosphere, or whether the time scales were too short, indicating that the dominate closure mechanism for these currents was in the Alfven wave front.

•

References

- International Auroral Atlas, International Union of Geodesy and Geophysics, Edinburgh University Press, 1963.
- Akasofu, S-I., The development of the auroral substorm, *Planetary Space Science*, 12, 273, 1964.
- Bolin, O., A data reduction algorithm for sounding rocket electric and magnetic field data, TRITA ALP-1994-107, Alfvén Laboratory, Royal Institute of Technology, Stockholm, Sweden, 1994.
- Borovsky, J. E. and Suszcynsky, D. M., Optical measurements of the fine structure of auroral arcs. Auroral Plasma Dynamics, Geophysical Monograph, 80, 25, American Geophysical Union, 1993.
- Brown, R. R., Electron precipitation in the auroral zone, *Space Science Review*, 5(3), 311, 1966.
- Boyd, J. S., Belon, A., and Romick, G. J., Latitude and time variations in precipitated electron energy inferred from measurements of auroral heights, *Journal of Geophysical Research*, 76, 7694, 1971.
- Burch, J. L., Diagnosis of auroral acceleration mechanism by particle measurements, in Meng, C.-I., Rycroft, M. J., and Frank, L. A. (editors), Auroral Physics, Cambridge University Press, 1991.
- Chen, F. F., Introduction to plasma physics, D. Reidel Publishing, New York, 1974.
- Chrzanowski, P., Greene, G., Lemmon, K. T., and Young, J. M., Travelling pressure waves associated with geomagnetic activity, *Journal of Geophysical Research*, 66, 3727, 1961.
- Friis-Christensen, E., and Lassen, K., Large scale distribution of discrete auroras and field-aligned currents, in Meng, C.-I., Rycroft, M. J., and Frank, L. A. (editors), Auroral Physics, Cambridge University Press, 1991.
- Fälthammar, C.-G., Physics of the aurora, *Geofisica International*, 30/4, 197, 1991.
- Galperin, Y. I., and Feldstein, Y. I., Auroral luminosity and its relationship to magnetospheric plasma domains, in Meng, C.-I., Rycroft, M. J., and Frank, L. A. (editors), Auroral Physics, Cambridge University Press, 1991.
- Ijima, T., Field-aligned currents during northward IMF. Magnetospheric Currents, Geophysical Monograph, 28, 115, American Geophysical Union, 1984.
- Jursa, A. S. (editor), Handbook of geophysics and the space environment, Air Force Geophysics Laboratory, Air Force Systems Command, United States Air Force, 1985.
- Lemaire, J., and Roth, M., Non-steady-state solar wind- magnetosphere interaction, *Space Science Review*, 57(1/2), 59, 1991.
- Lyons, L. R., and Walterscheid, R. L., Feedback between neutral winds and auroral arc electrodynamics, *Journal of Geophysical Research*, 91, 13506, 1986.

Newell, P. T., Meng, C.-I., and Hardy, D. A., Overview of electron and ion precipitation in the auroral oval., in Meng, C.-I., Rycroft, M. J., and Frank, L. A. (editors), *Auroral Physics*, Cambridge University Press, 1991.

Perreault, P., Akasofu, S.-I., A study of geomagnetic storms, *Geophysical Journal of the Royal Astronomical Society*, 54, 547, 1978.

Potemra, T. A., Birkeland currents, recent contributions from satellite measurements, *Physica Scripta*, T18, 152, 1987.

Potemra, T. A., Source of large scale Birkeland currents, in Holtet, J. A., and Egeland, A. (editors), *Physical Signatures of Magnetospheric Boundary Layer Process*, Kluwer Academic Publishers, Dordrecht, 1994.

Reiff, P. H., Spiro, R. W., and Hill, T. W., Dependence of polar cap potential on interplanetary parameters, *Journal of Geophysical Research*, 86, 7639, 1986.

Rostoker, G., Overview of observations and models of the auroral substorms, in Meng, C.-I., Rycroft, M. J., and Frank, L. A. (editors), *Auroral Physics*, Cambridge University Press, 1991.

Rostoker, G., The roles of direct input of energy from the solar wind, *Space Science Review*, 46(3), 93, 1987.

Sorenson, H. W., Kalman Filtering: Theory and Application, IEEE Press, New York, 1985.

Vallance Jones, A., *Aurora*, Plenum Publishing, New York, 1974.

Vasyliunas, V. M., Fundamentals of current description. *Magnetospheric Currents*, Geophysical Monograph, 28, American Geophysical Union, 1984.

Appendix A - Data Storage

The data was supplied in nine compressed files (mom4_*.zip; *=1,2,...,9). To enable direct reading of these with the minimum of memory space required, the files were somewhat modified.

Firstly they were unzipped, and it was discovered that the formatting of the files was not as efficient as it might be. To improve this the files were read, and then written as unformatted data files. To compress the data even more, yet still retain it's usefulness, it was written in the minimum number of bytes possible using standard FORTRAN data structures.

Each line of information originally contained;

- a time for the measurement, given to 3 decimal places in seconds after launch.
- 6 decimal numbers between 0 and 255, representing the most and least significant bytes of the 16 bit output from each axis of the magnetometer.

The first step was to convert the two bytes for each axis from two bytes of an offset binary, to a single integer two's complement form. The time measurements were given from around -5.000 to 700.000 seconds. These numbers were first converted to integers by using multiplying by 1000, and using the NINT (convert to nearest integer) command. This yielded a range of 705 000, requiring a minimum of 20 bits. It was decided to store the data as one 16 bit integer and a byte, rather than employing the slightly larger long integer format. These functions were performed by the routine *datst*, which was used to get the data into a single file (aurturb_mag.dat).

The result of this was that the data occupied slightly less than double the memory it required in the compressed form, but it was readily accessible, and almost a factor of five smaller than the plain expanded files.

Appendix B - Missing and Repeated Records

Originally a mistake was made in reformatting the data supplied (Appendix A). This was traced to a problem in converting the times to integers, in that the FORTRAN function IFIX (convert to integer) was used rather than NINT (convert to **nearest** integer). This meant that every fourth value was rounded to the next lowest integer (i.e. 5.00000 was converted to 4). The investigation into this problem, highlighted the fact that it was very hard to tell if there was any data missing from the files provided.

Another problem was that the magnetometer sampling frequency of 1562.5 Hz corresponds to a time resolution of 0.00064 seconds, whilst the data was only given to three significant figures. The consequences of this are indicated by Table B1, where it can be seen that occasionally two data records are assigned the same time. This is obviously incorrect, so when analysing the data the following strategy was adopted.

Table B1

'Real' time of sample	Time recorded in data file
0.00000	0.000
0.00064	0.001
0.00128	0.001
0.00192	0.002
0.00256	0.003
0.00320	0.003
0.00384	0.004
0.00448	0.004
0.00512	0.005
0.00576	0.006
0.00640	0.006
0.00704	0.007
0.00768	0.008
0.00832	0.008
0.00896	0.009
0.00960	0.010
0.01024	0.010
0.01088	0.011

In most cases, one is not interested in the full data set, so although the routines have to read all the data before the time of interest, (it being stored sequentially in the file), it is not necessary to keep that data available. Thus, it was possible to use the times given in the data file to decide when the start time for a particle program run was reached.

The advantages of this is twofold,

- it reduces the possibility of incorporating errors due to missed or repeated data records
- it reduces the errors that accumulate if the instrument time resolution differs from the assumed 0.00064s.

In theory therefore, there should be a linear relationship between the index for each data record, and the associated time (with a slope of 0.00064 seconds). To investigate the accuracy of the assumed times between measurements, a straight line was fitted to the data. Originally linear regression (Press et al., 1986, p.508) was used, but this indicated a time resolution of ~0.00062 seconds (*check_times*).

An alternative program to for this is *chk10*, which uses ten samples at a time, and checks if they are all separate by the appropriate time gap (an input to the program). This has the advantage that it notes exact times of errors, and attempts to give an indication of the type of error occurring (whether records have been missed or repeated). The results found from this were found to be very good, although there was the problem that the repeated sections of data were only indicated by a start time, so had to be checked manually to search for the length of the repeated block. Note also that the program frequently records two errors at a single point.

The results from running *chk10* are included with this report on the following pages. The errors indicated by *recmiss* being records which have been missed; those labelled *RECREP* the start time of a repeated block of data. The simplest way of dealing with these problems was to edit the files manually before running *datst* (Appendix A). Note that, in view of the useful period of data indicated by Figure 26, results before 182 seconds and after 660 were not deemed worth the effort of correcting.

1562.500	=SAMPLE FRE
recmiss	1279
recmiss	1285
recmiss	1285
recmiss	1290
recmiss	1315
recmiss	1353
recmiss	1353
recmiss	1371
recmiss	1371
recmiss	1389
recmiss	1462
recmiss	1462
recmiss	1478
recmiss	1478
recmiss	1485
recmiss	1498
recmiss	1498
recmiss	1547
recmiss	1547
recmiss	1556
recmiss	1565
recmiss	1565
recmiss	1591
recmiss	1591
recmiss	1642
recmiss	1646
recmiss	1665
recmiss	1676
recmiss	1676
recmiss	1683
recmiss	1687
recmiss	1757
recmiss	1775
recmiss	1775
recmiss	1790
recmiss	2884
recmiss	2884
recmiss	2889
recmiss	2934
recmiss	2934
recmiss	8495
recmiss	17158
recmiss	17158
recmiss	18027
recmiss	18027
recmiss	24370
recmiss	24371
recmiss	24404
recmiss	24404
recmiss	24417
recmiss	41146
recmiss	41146
recmiss	41226
recmiss	41226
recmiss	41364
recmiss	41364
recmiss	41416
recmiss	41416
recmiss	42035
recmiss	91959
recmiss	91959
recmiss	92073
recmiss	92073
recmiss	92293
recmiss	92293
recmiss	98107
recmiss	98107

RECREP	119491
RECREP	361170
recmiss	446331
RECREP	446330
RECREP	459491
RECREP	459491
recmiss	603860
recmiss	603860
recmiss	684104
recmiss	684104
recmiss	684114
recmiss	684114
recmiss	684119
recmiss	684449
recmiss	684449
recmiss	684453
recmiss	684467
recmiss	684467
recmiss	684479
recmiss	684479
recmiss	684486
recmiss	684486
recmiss	684504
recmiss	684504
recmiss	684509
recmiss	684522
recmiss	684522
recmiss	684530
recmiss	684530
recmiss	684539
recmiss	684543
recmiss	684723
recmiss	684723
recmiss	684728
recmiss	684747
recmiss	684747
recmiss	684755
recmiss	684755
recmiss	684761
recmiss	684772
recmiss	684779
recmiss	684792
recmiss	684908
recmiss	684908
recmiss	684917
recmiss	684917
recmiss	684923
recmiss	684927
recmiss	684932
recmiss	684976
recmiss	684976
recmiss	685009
recmiss	685009
recmiss	685218
recmiss	685224
recmiss	685233
recmiss	685239
recmiss	685239
recmiss	685247
recmiss	685247
recmiss	685252
recmiss	685257
recmiss	685327
recmiss	685327
recmiss	685519
recmiss	685519
recmiss	685524
recmiss	685529

recmiss 685544
recmiss 685544
recmiss 685551
recmiss 685556
recmiss 685670
recmiss 685674
recmiss 685695
recmiss 685695
recmiss 685808
recmiss 685808
recmiss 685823
recmiss 685823
recmiss 685850
recmiss 685850
recmiss 685860
recmiss 685863
recmiss 685880
recmiss 685894
recmiss 685902
recmiss 685910
recmiss 685910
recmiss 685926
recmiss 685932
recmiss 685932
recmiss 685940
recmiss 685950
recmiss 685950
recmiss 685961
recmiss 685968
recmiss 685984
recmiss 685984
recmiss 685999
recmiss 686003
recmiss 686019
recmiss 686023
recmiss 686029
recmiss 686043
recmiss 686049
recmiss 686053
recmiss 686060
recmiss 686065
recmiss 686070
recmiss 686084
recmiss 686126
recmiss 686126
recmiss 686129
recmiss 686140
recmiss 686140
recmiss 686144
recmiss 686151
recmiss 686164
recmiss 686164
recmiss 686167

THAT'S THAT ONE DONE

LAST 2RECORDS NOT CHECKED

LAST RECORD CHECKED WAS 686184

Appendix C - Filtering

The magnetometer used on Auroral Turbulence, had a cut-off frequency of around 300-400 Hz. This means that, with a sampling rate of 1562.5 Hz, almost twice as many measurements as necessary were made. This gave the opportunity for some averaging of the data, which improved the signal-to-noise ratio.

The details of filter the data were investigated in much depth, as it was not deemed to be the most crucial part of the data reduction. In particular, the digital filter to be used was prepared using IDL (Interactive Data Language) with the DIGITAL-FILTER function. The input parameters to this were as follows:

Property of filter	Chosen Value for Parameter
Pass band lower frequency	0 Hz (all signals from d.c.)
Pass band upper frequency	50 Hz (see below)
Size of Gibb's Phenomena in -dB	50 (recommended in manual)
No of coefficients for the filter	512 (excessively large, but as the data set was of finite size, it was decided that the slight gain in accuracy was worth the extra computing time).

The upper limit for the pass band was chosen to 50 Hz arbitrarily. This figure allows a larger improvement of signal-to-noise ratio, than does a cut off of 400 Hz. The argument given in Section 2 for the improved resolution of rockets over satellites, indicates that 50 Hz should be sufficient to resolve the features of the arc structure (especially when one considers the fact that the rocket and arc are moving in approximately the same direction, thus reducing their relative velocity and increasing the resolution even more).

The filtering was done using the command file *filt_mag.idl*, which uses a number of subroutines written for the purpose.

The frequency responses of the filter, over the range of interest, are shown in Figures C1 and C2. These were calculated from the filter coefficients in the program *calc_filt_resp.pro*. This algorithm employed the following equations:

The filter transfer function $H(\omega)$ is given by

$$H(\omega) = \sum_{k=0}^{M-1} b_k e^{-j\omega k} = \sum_{k=0}^{M-1} b_k \cos(\omega k) - j \sum_{k=0}^{M-1} b_k \sin(\omega k) = H_{\Re}(\omega k) + H_{\Im}(\omega k)$$

where ω is the angular frequency,
 M = number of coefficients in the filter
 and b_k represents the filter coefficients

From this the gain and phase responses are respectively,

$$\text{Gain} = |H(\omega)| = \sqrt{H_{\Re}(\omega)^2 + H_{\Im}(\omega)^2}$$

$$\text{Phase} = \theta(\omega) = \arctan\left(\frac{H_{\Im}(\omega)}{H_{\Re}(\omega)}\right)$$

From these the time delay caused by the filter can be calculated, by taking the gradient of the phase response with respect to ω . This was done numerically, by simply taking the difference between adjacent points in the pass band of the response (where the phase is linear). The results of this are shown in Figure C3, note that in the pass band the time delay is constant at a value of 0.32768 seconds (the peaks are the results of uncompensated discontinuities, resulting from the fact that the arctan function returns a results limited to between 0 and π radians).

Note that although the gain of the filter in the pass band appears close to 0 dB through most of the pass band, a closer inspection of the results indicated a departure from unity gain of around one part in 10 000. This is a minor effect, but the nature of the problem means that such distortions will introduce noise of a few nanoteslas into the results.

It should also be added that, despite calculating the delay introduced by the filter, no attempt to correct for this was done in the analysis. When it becomes necessary to compare the magnetic field results with other measurements, this should be taken into account.

Appendix D - Incorrect Modelling of the Rocket Motion

Bolin (1994) describes a method for rocket borne magnetometer data reduction, which provided the basis for this investigation. However, it turned out that attempts to apply these ideas, without investigating the validity of the assumptions, turned out to be quite misleading.

The basic idea of this technique is that the z-axis data is dominated by coning, but shows a small, low frequency oscillation due to a small misalignment with the spin axis, as described in Section 6.2.1. This was applied successfully in the case of the CRIT II rocket experiment flown from Wallops Island in 1989, using a magnetometer identical to the one used on Auroral Turbulence (the latter originally being the spare for CRIT II).

The problem with Auroral Turbulence was the somewhat unusual situation of a coning angle less than the misalignment between the z-axis and the spin axis. Not realising that this was the case, the coning frequency was assumed to be about 0.4 Hz, with the spin frequency close to this (resulting in the low frequency beating due to misalignment, Section 6.2.1).

Applying this model resulted gave somewhat erroneous results when attempts were made to remove the lower frequency oscillations, by calculating the misalignment angles χ and τ . It was then assumed that the misalignment was negligible compared to some other effect causing the low frequency oscillations.

Without the benefit of the simulation routines, it was mistakenly assumed that the x- and y- axes oscillations were due to spinning, and a program *find_frequencies* was written to investigate this. This worked by finding the peaks of the data in the magnetic field measurements for each axis, and then the period between adjacent maxima (and also adjacent minima, as a check). These peaks were found using a sliding window, and looking for the point where the gradient (found by linear regression), changed sign.

The results indicated that the spin frequency itself was oscillating slightly (now known to be due to beating between spinning and coning), which, along with the oscillations in coning motion were assumed to be indicative of low frequency oscillations of the FRA, causing the opening angle of the coning to oscillate (nutation).

Routines were developed to fit sine waves to these two oscillations in v_z , (added on to a linear fit to represent the change in κ), as it was believed that even if the exact form of the motion was unknown, at least by finding the average form of v_z the components parallel and perpendicular to the magnetic field could be obtained. In conjunction with this, Sophia was used to develop models in an attempt to explain the motion of the rocket as an oscillation of the FRA.

The routines developed for this used empirical parameters which were in some ways similar to those used in *fit_10* (Section 6.3), i.e. a linear fit corresponding to k_1 , k_2 and k_3 , two amplitudes for the sine waves (χ and θ), two frequencies (similar to ω_{spin} and ω_{cone}) and two phases (c.f. discussion of non-independence of τ , and the spin and coning phases)

The results obtained were slightly worse than obtained with *fit_10* (an oscillation of around 20 nT remained after fitting to 10 seconds of data), lacked a physical explanation, and only produced results for two of the three quantities required to define the magnetic field relative to the background. The one advantage of this routine is that the simpler equations (not involving arccosines) allowed the derivatives to be used to speed up the fitting by using *mrqmin* (Press et al., 1986, p526).

It was not until the simulation routines were written, and compared to the x- and y- axis data that the mistakes made became clear, and it is recommended that future analyses do not neglect the results from these axes as they provide vital clues which are necessary for the data reduction.

Appendix E Text Files Output From *Fit_10*

The following pages are the text files output from *fit_10* when it was run six times in order to get a fit between 290 and 300 seconds. The first file shows, in the following order

- The time and date the program was run over
- The input data file (i.e. output from *datst* which was then filtered)
- The file containing the calibration parameters (i.e. output from *f*
ind_param_amoeba (*fpam9* short for using nine parameters) or in this case, the average values found using *plot_fpam_out*) between 255 and 310 seconds.
- The values of those calibration parameters
- The period used for fitting a linear function to κ .
- The flight times over which the fit is done.
- The file used for outputting the parameters
- The input parameters to the program for the fitting. (i.e. initial guess)
- The variations allowed in them (Δ)
- The parameters after fitting was completed
- The number of data points in the time interval (i.e. number of different times read from the data file)
- The variance and "standard deviation" (remember the factor of $\sqrt{3}$)
- The file to which the *pgplot* graphs made were written

The other files are similar but use the parameters written out by the first routine (hence the fitting of κ from 0.00 to 0.00)!

These are the results from fit_10_1.for
Which was run from 22:16:19 on 26-SEP-95
until 22:18:44 on 26-SEP-95

Run with the magnetometer data from
[SMITH.AT.RAWDATA]AURTURB_MAG_FILT.DAT

Using calibration from
[smith.at.odata]FPAM9_MEAN_255_310.dat

i.e. s1= -1.831299
s2= 1.829067
s3= -1.819369
o1= 1510.620
o2= -724.5208
o3= -400.8999
alpha= 6.8333215E-06
beta= -5.6341430E-04
gamma= 6.4311484E-06

The fit to kappa was done from 250.0000 to 350.0000

Whilst the whole fitting of all 10 parameters
was done from 290.0000 to 300.0000

The parameters after fitting were written to
[smith.at.odata]290_300_10.DAT

The input parameters were
CHI= 8.0000004E-03
THETA= 4.0000002E-03
OMEGA_CONE= 0.6100000
OMEGA_SPIN= 1.830000
PHASE_CONE= 0.0000000E+00
PHASE_SPIN= 0.0000000E+00
TAU= 0.0000000E+00
K1= 0.0000000E+00
K2= 0.0000000E+00
K3= 0.0000000E+00

With allowed variations of

Max. allowable change in CHI IS 0.0000000E+00
Max. allowable change in THETA IS 0.0000000E+00
Max. allowable change in OMEGA_CONE IS 0.0000000E+00
Max. allowable change in OMEGA_SPIN IS 0.0000000E+00
Max. allowable change in PHASE_CONE IS 5.000000
Max. allowable change in PHASE_SPIN IS 5.000000
Max. allowable change in TAU IS 5.000000
Max. allowable change in K1 IS 0.0000000E+00
Max. allowable change in K2 IS 0.0000000E+00
Max. allowable change in K3 IS 0.0000000E+00

After the fitting the parameters were

chi= 8.0000004E-03
theta= 4.0000002E-03
omega_cone= 0.6100984
omega_spin 1.830000
phase_cone 0.7820795
phase_spin -2.220591
tau= 1.092738
k1= 7.7076487E-02
k2= 294.1768
k3= 2.2099103E-04

And the sumsq is 5.9996573E-03
With the number of points being 1563
This is a standard deviation of 1.9592224E-03

The output device (at the end) was
[SMITH.AT.FIT_10_PLOTS]290_300_1.PS/PS

These are the results from fit_10_1.for
Which was run from 22:18:45 on 26-SEP-95
until 22:27:28 on 26-SEP-95

Run with the magnetometer data from
[SMITH.AT.RAWDATA]AURTURB_MAG_FILT.DAT

Using calibration from
[smith.at.udata]FPAM9_MEAN_255_310.dat

i.e. s1= -1.831299
s2= 1.829067
s3= -1.819369
o1= 1510.620
o2= -724.5208
o3= -400.8999
alpha= 6.8333215E-06
beta= -5.6341430E-04
gamma= 6.4311484E-06

The fit to kappa was done from 0.0000000E+00 to 0.0000000E+00

Whilst the whole fitting of all 10 parameters
was done from 290.0000 to 300.0000

The parameters after fitting were written to
[smith.at.udata]290_300_10.DAT

The input parameters were

CHI= 8.0000004E-03
THETA= 4.0000002E-03
OMEGA_CONE= 0.6100984
OMEGA_SPIN= 1.830000
PHASE_CONE= 0.7820795
PHASE_SPIN= -2.220591
TAU= 1.092738
K1= 7.7076487E-02
K2= 294.1768
K3= 2.2099103E-04

With allowed variations of

Max. allowable change in CHI IS 0.0000000E+00
Max. allowable change in THETA IS 0.0000000E+00
Max. allowable change in OMEGA_CONE IS 9.9999998E-03
Max. allowable change in OMEGA_SPIN IS 9.9999998E-03
Max. allowable change in PHASE_CONE IS 0.2000000
Max. allowable change in PHASE_SPIN IS 0.2000000
Max. allowable change in TAU IS 0.2000000
Max. allowable change in K1 IS 0.0000000E+00
Max. allowable change in K2 IS 0.0000000E+00
Max. allowable change in K3 IS 0.0000000E+00

After the fitting the parameters were

chi= 8.0000004E-03
theta= 4.0000002E-03
omega_cone= 0.6142815
omega_spin 1.835106
phase_cone -0.2749522
phase_spin -3.879390
tau= 1.067518
k1= 7.7076487E-02
k2= 294.1768
k3= 2.2114608E-04

And the sumsq is 6.7450933E-04
With the number of points being 1563
This is a standard deviation of 6.5692305E-04

The output device (at the end) was
[SMITH.AT.FIT_10_PLOTS]290_300_2.PS/PS

These are the results from fit_10_1.for
Which was run from 22:27:29 on 26-SEP-95
until 22:34:44 on 26-SEP-95

Run with the magnetometer data from
[SMITH.AT.RAWDATA]AURTURB_MAG_FILT.DAT

Using calibration from
[smith.at.udata]FPAM9_MEAN_255_310.dat

i.e. s1= -1.831299
s2= 1.829067
s3= -1.819369
o1= 1510.620
o2= -724.5208
o3= -400.8999
alpha= 6.8333215E-06
beta= -5.6341430E-04
gamma= 6.4311484E-06

The fit to kappa was done from 0.0000000E+00 to 0.0000000E+00

Whilst the whole fitting of all 10 parameters
was done from 290.0000 to 300.0000

The parameters after fitting were written to
[smith.at.udata]290_300_10.DAT

The input parameters were

CHI= 8.0000004E-03
THETA= 4.0000002E-03
OMEGA_CONE= 0.6142815
OMEGA_SPIN= 1.835106
PHASE_CONE= -0.2749522
PHASE_SPIN= -3.879390
TAU= 1.067518
K1= 7.7076487E-02
K2= 294.1768
K3= 2.2114608E-04

With allowed variations of

Max. allowable change in CHI IS 1.0000000E-03
Max. allowable change in THETA IS 1.0000000E-03
Max. allowable change in OMEGA_CONE IS 9.9999998E-03
Max. allowable change in OMEGA_SPIN IS 9.9999998E-03
Max. allowable change in PHASE_CONE IS 0.2000000
Max. allowable change in PHASE_SPIN IS 0.2000000
Max. allowable change in TAU IS 0.2000000
Max. allowable change in K1 IS 0.0000000E+00
Max. allowable change in K2 IS 0.0000000E+00
Max. allowable change in K3 IS 0.0000000E+00

After the fitting the parameters were

chi= 8.2249008E-03
theta= 4.4374447E-03
omega_cone= 0.6142938
omega_spin= 1.835093
phase_cone= -0.2775489
phase_spin= -3.876148
tau= 1.066912
k1= 7.7076487E-02
k2= 294.1768
k3= 2.2114607E-04

And the sumsq is 1.2649313E-04
With the number of points being 1563
This is a standard deviation of 2.8448147E-04

The output device (at the end) was
[SMITH.AT.FIT_10_PLOTS]290_300_3.PS/PS

These are the results from fit_10_1.for
Which was run from 22:34:44 on 26-SEP-95
until 22:42:53 on 26-SEP-95

Run with the magnetometer data from
[SMITH.AT.RAWDATA]AURTURB_MAG_FILT.DAT

Using calibration from
[smith.at.udata]FPAM9_MEAN_255_310.dat

i.e. s1= -1.831299
s2= 1.829067
s3= -1.819369
o1= 1510.620
o2= -724.5208
o3= -400.8999
alpha= 6.8333215E-06
beta= -5.6341430E-04
gamma= 6.4311484E-06

The fit to kappa was done from 0.0000000E+00 to 0.0000000E+00

Whilst the whole fitting of all 10 parameters
was done from 290.0000 to 300.0000

The parameters after fitting were written to
[smith.at.udata]290_300_10.DAT

The input parameters were

CHI= 8.2249008E-03
THETA= 4.4374447E-03
OMEGA_CONE= 0.6142938
OMEGA_SPIN= 1.835093
PHASE_CONE= -0.2775489
PHASE_SPIN= -3.876148
TAU= 1.066912
K1= 7.7076487E-02
K2= 294.1768
K3= 2.2114607E-04

With allowed variations of

Max. allowable change in CHI IS 1.0000000E-03
Max. allowable change in THETA IS 1.0000000E-03
Max. allowable change in OMEGA_CONE IS 9.999998E-03
Max. allowable change in OMEGA_SPIN IS 9.999998E-03
Max. allowable change in PHASE_CONE IS 0.2000000
Max. allowable change in PHASE_SPIN IS 0.2000000
Max. allowable change in TAU IS 0.2000000
Max. allowable change in K1 IS 0.0000000E+00
Max. allowable change in K2 IS 0.0000000E+00
Max. allowable change in K3 IS 0.0000000E+00

After the fitting the parameters were

chi= 8.2246885E-03
theta= 4.4283122E-03
omega_cone= 0.6142956
omega_spin 1.835093
phase_cone -0.2779091
phase_spin -3.876710
tau= 1.067152
k1= 7.7076487E-02
k2= 294.1768
k3= 2.2114607E-04

And the sumsq is 1.2618721E-04
With the number of points being 1563
This is a standard deviation of 2.8413726E-04

The output device (at the end) was
[SMITH.AT.FIT_10_PLOTS]290_300_4.PS/PS

These are the results from fit_10_1.for
Which was run from 22:42:54 on 26-SEP-95
until 23:14:23 on 26-SEP-95

Run with the magnetometer data from
[SMITH.AT.RAWDATA]AURTURB_MAG_FILT.DAT

Using calibration from
[smith.at.udata]FPAM9_MEAN_255_310.dat

i.e. s1= -1.831299
s2= 1.829067
s3= -1.819369
o1= 1510.620
o2= -724.5208
o3= -400.8999
alpha= 6.8333215E-06
beta= -5.6341430E-04
gamma= 6.4311484E-06

The fit to kappa was done from 0.0000000E+00 to 0.0000000E+00

Whilst the whole fitting of all 10 parameters
was done from 290.0000 to 300.0000

The parameters after fitting were written to
[smith.at.udata]290_300_10.DAT

The input parameters were

CHI= 8.2246885E-03
THETA= 4.4283122E-03
OMEGA_CONE= 0.6142956
OMEGA_SPIN= 1.835093
PHASE_CONE= -0.2779091
PHASE_SPIN= -3.876710
TAU= 1.067152
K1= 7.7076487E-02
K2= 294.1768
K3= 2.2114607E-04

With allowed variations of

Max. allowable change in CHI IS 9.9999997E-05
Max. allowable change in THETA IS 9.9999997E-05
Max. allowable change in OMEGA_CONE IS 1.0000000E-03
Max. allowable change in OMEGA_SPIN IS 1.0000000E-03
Max. allowable change in PHASE_CONE IS 2.0000000E-02
Max. allowable change in PHASE_SPIN IS 2.0000000E-02
Max. allowable change in TAU IS 2.0000000E-02
Max. allowable change in K1 IS 1.5415298E-02
Max. allowable change in K2 IS 58.83535
Max. allowable change in K3 IS 4.4229215E-05

After the fitting the parameters were

chi= 8.2406010E-03
theta= 4.4546486E-03
omega_cone= 0.6145740
omega_spin= 1.835367
phase_cone= -0.3531191
phase_spin= -3.961762
tau= 1.064592
k1= 7.9153098E-02
k2= 304.2909
k3= 2.2081303E-04

And the sumsq is 3.3391290E-05
With the number of points being 1563
This is a standard deviation of 1.4616289E-04

The output device (at the end) was
[SMITH.AT.FIT_10_PLOTS]290_300_5.PS/PS

These are the results from fit_10_1.for
Which was run from 23:14:23 on 26-SEP-95
until 23:27:23 on 26-SEP-95

Run with the magnetometer data from
[SMITH.AT.RAWDATA]AURTURB_MAG_FILT.DAT

Using calibration from
[smith.at.udata]FPAM9_MEAN_255_310.dat

i.e. s1= -1.831299
s2= 1.829067
s3= -1.819369
o1= 1510.620
o2= -724.5208
o3= -400.8999
alpha= 6.8333215E-06
beta= -5.6341430E-04
gamma= 6.4311484E-06

The fit to kappa was done from 0.0000000E+00 to 0.0000000E+00

Whilst the whole fitting of all 10 parameters
was done from 290.0000 to 300.0000

The parameters after fitting were written to
[smith.at.udata]290_300_10.DAT

The input parameters were

CHI= 8.2406010E-03
THETA= 4.4546486E-03
OMEGA_CONE= 0.6145740
OMEGA_SPIN= 1.835367
PHASE_CONE= -0.3531191
PHASE_SPIN= -3.961762
TAU= 1.064592
K1= 7.9153098E-02
K2= 304.2909
K3= 2.2081303E-04

With allowed variations of

Max. allowable change in CHI IS 9.9999997E-05
Max. allowable change in THETA IS 9.9999997E-05
Max. allowable change in OMEGA_CONE IS 1.0000000E-03
Max. allowable change in OMEGA_SPIN IS 1.0000000E-03
Max. allowable change in PHASE_CONE IS 2.0000000E-02
Max. allowable change in PHASE_SPIN IS 2.0000000E-02
Max. allowable change in TAU IS 2.0000000E-02
Max. allowable change in K1 IS 1.5830619E-02
Max. allowable change in K2 IS 60.85818
Max. allowable change in K3 IS 4.4162607E-05

After the fitting the parameters were

chi= 8.2349498E-03
theta= 4.4462900E-03
omega_cone= 0.6145782
omega_spin 1.835344
phase_cone -0.3508926
phase_spin -3.959568
tau= 1.065690
k1= 7.9467461E-02
k2= 305.5848
k3= 2.2349377E-04

And the sumsq is 3.2267486E-05
With the number of points being 1563
This is a standard deviation of 1.4368223E-04

The output device (at the end) was
[SMITH.AT.FIT_10_PLOTS]290_300_6.PS/PS

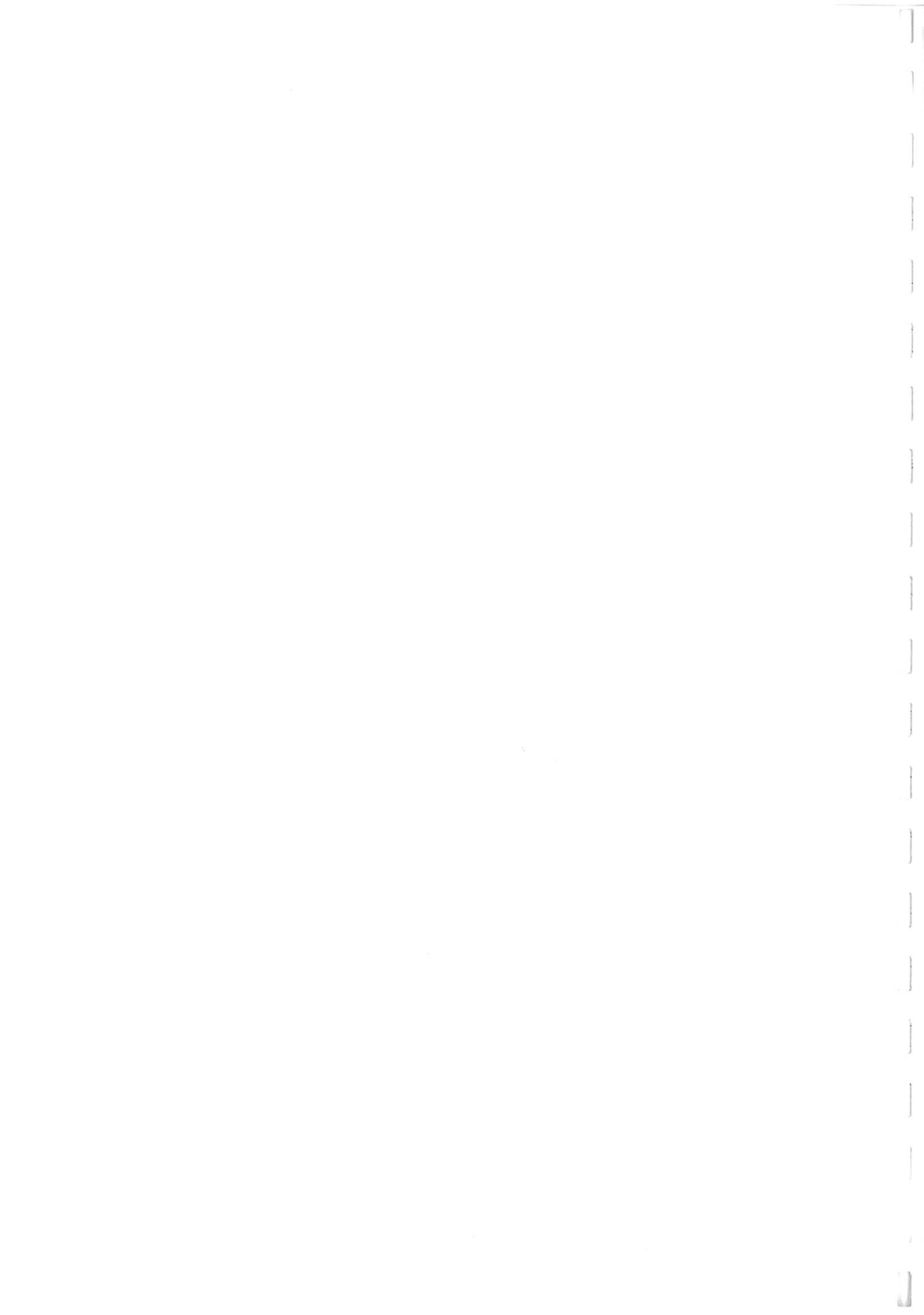


Figure 1

This shows the position of the auroral oval at four times throughout the day. Auroral Turbulence was launched from Poker Flats near Fairbanks, Alaska. This area is under the oval around 1200 UT (corresponding to near midnight magnetic local time). Notice how in this diagram the oval appears to rotate; in reality it is the Earth rotating, whilst the oval remains fixed with respect to the Sun. (Jursa, 1985)

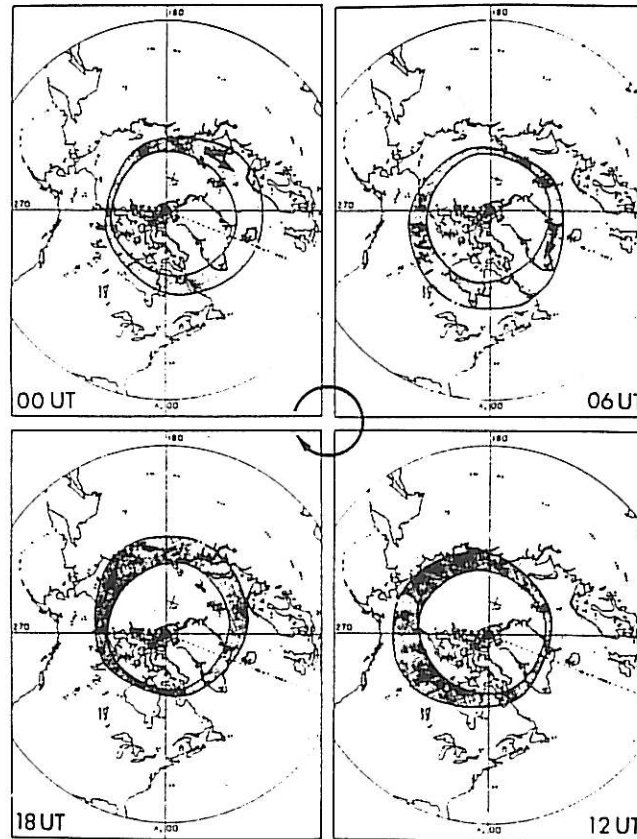
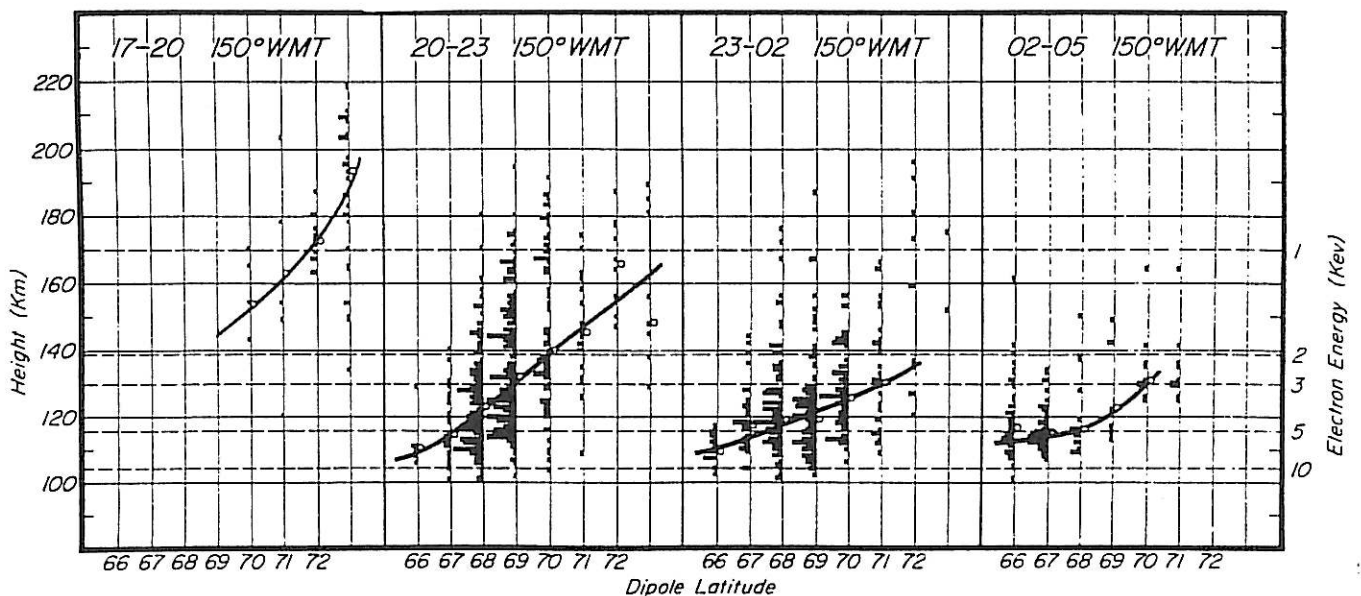


Figure 2

This diagram shows the height distribution of the peak auroral emission at 5557 Å. All charts are for 150° West magnetic latitude, and the four panels show different times. Local magnetic midnight is around 0115. The second and third panels indicate the increased occurrence of aurora around and just before midnight. The x-axis of each plot is the dipole latitude, whilst the y-axis shows either the height distribution of the aurora, or equivalently the energy of the electrons causing it (Section 1.16) (Boyd *et al.*, 1971)



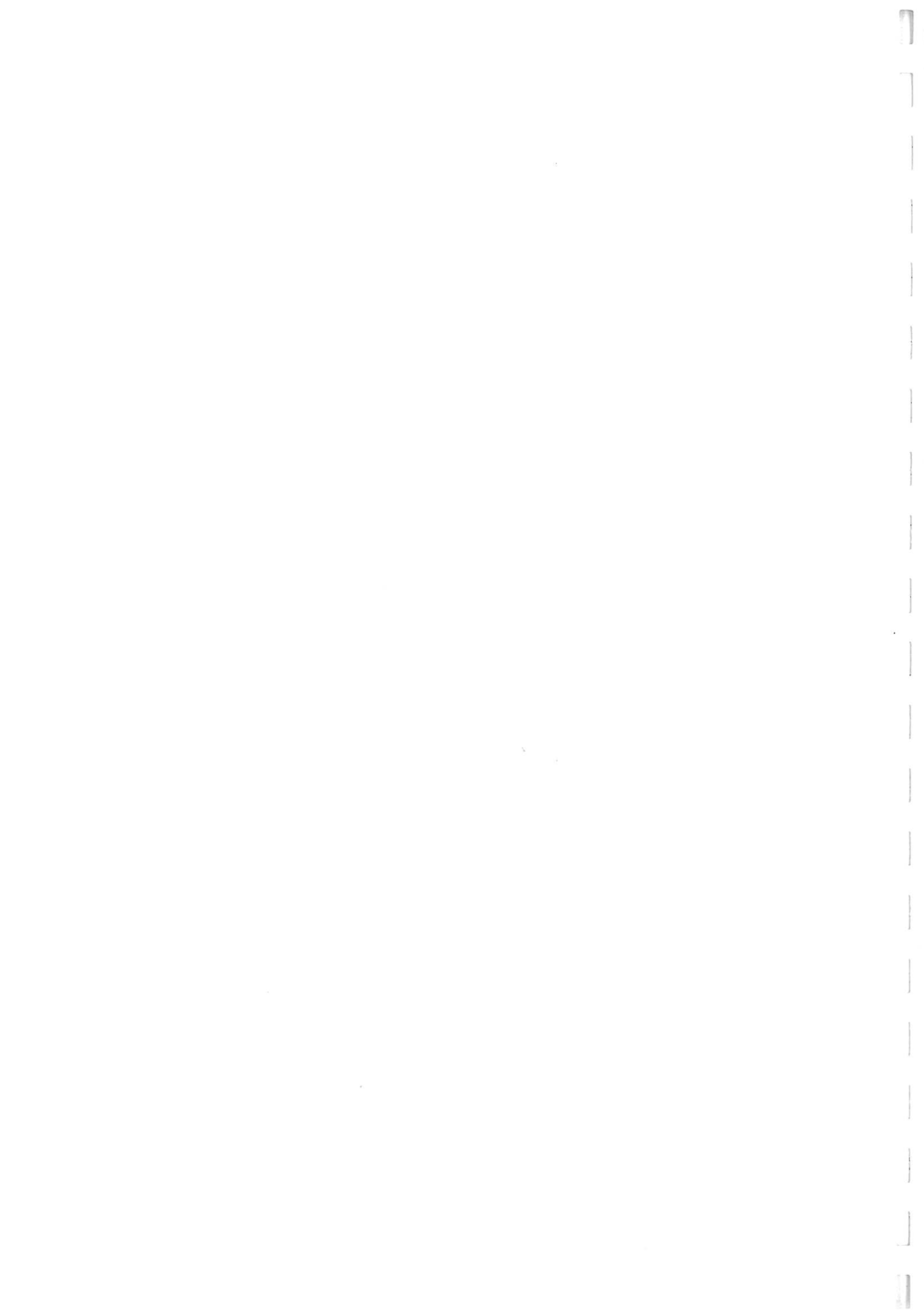


Figure 3

Plot showing the variation of electron density with height in the atmosphere, under various conditions. Auroral Turbulence was launched at night in March 1994, near solar minimum. The letters E, F1, F2 refer to the different layers of the ionosphere. Comparison with figure 2 shows that most visible aurora occurs in the E layer.

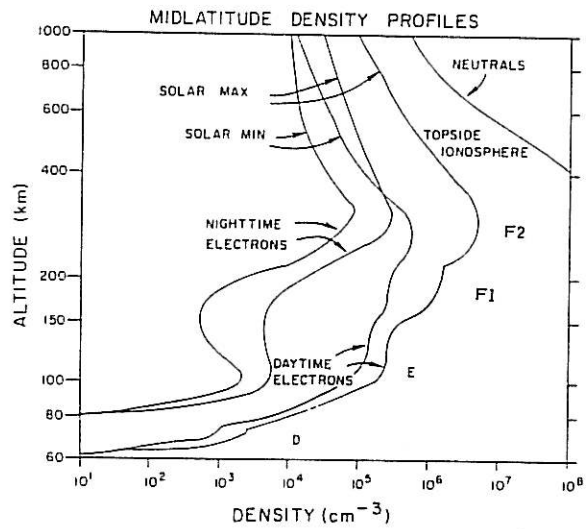
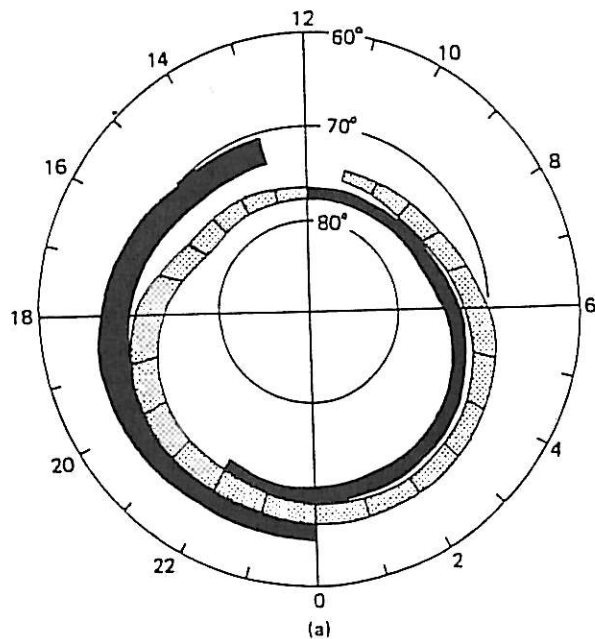


Figure 4

Showing the average distribution of field aligned currents as a function of magnetic latitude and local time. The dark areas indicate downward current, the light upward. The region one currents are the ones closer to the pole, with electrons flowing into the ionosphere on the night side (upward current), and away on the day side. The region two currents are nearer the equator, and flow in the opposite direction.



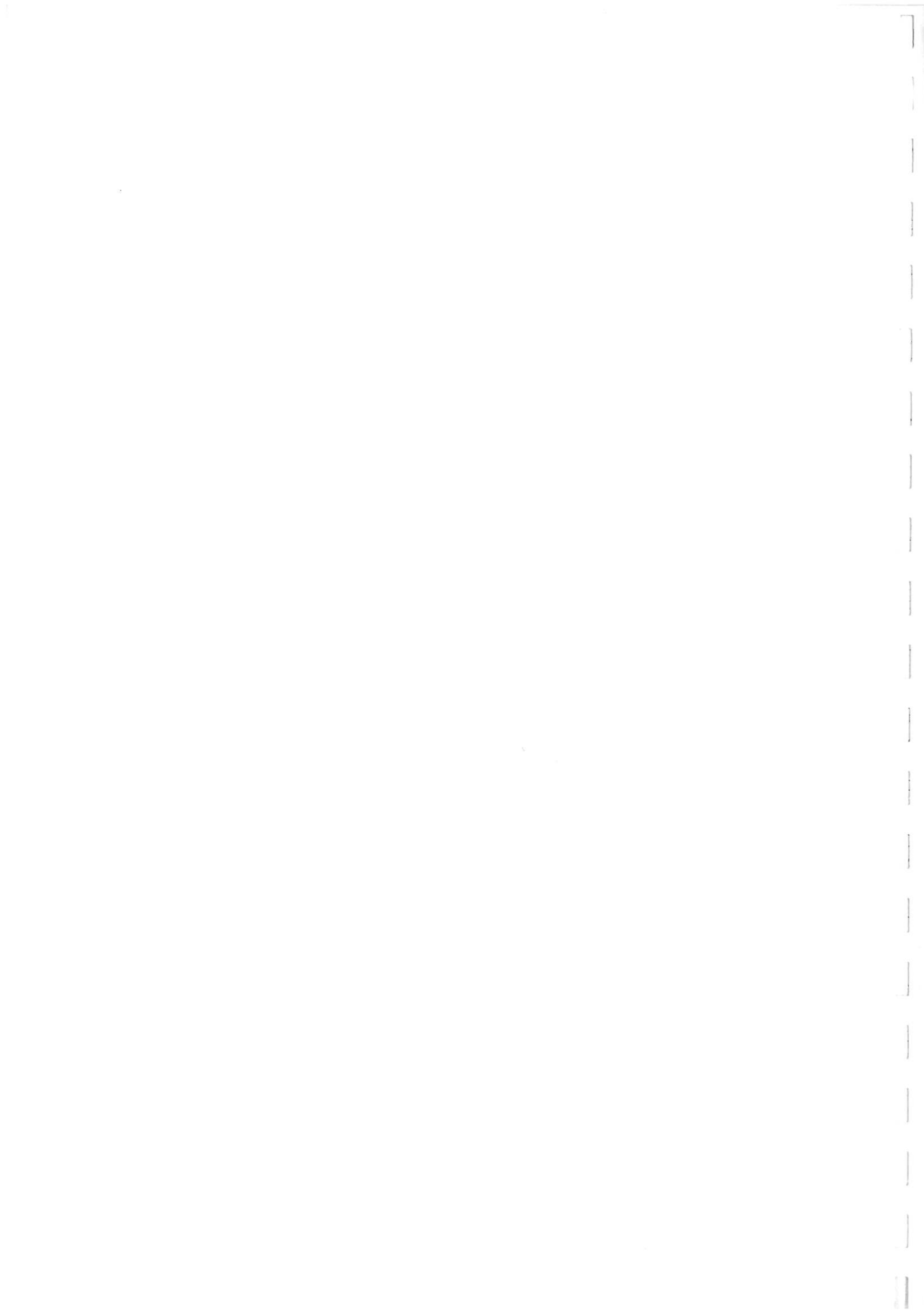


Figure 5

A cartoon showing different regions of the magnetosphere (after Siscoe, 1991), including;

- BPS- Boundary Plasma Sheet
- CPS- Central Plasma Sheet
- LLBL (LBL)- Low-Latitude Boundary Layer
- PSBL- Plasma Sheet Boundary Layer

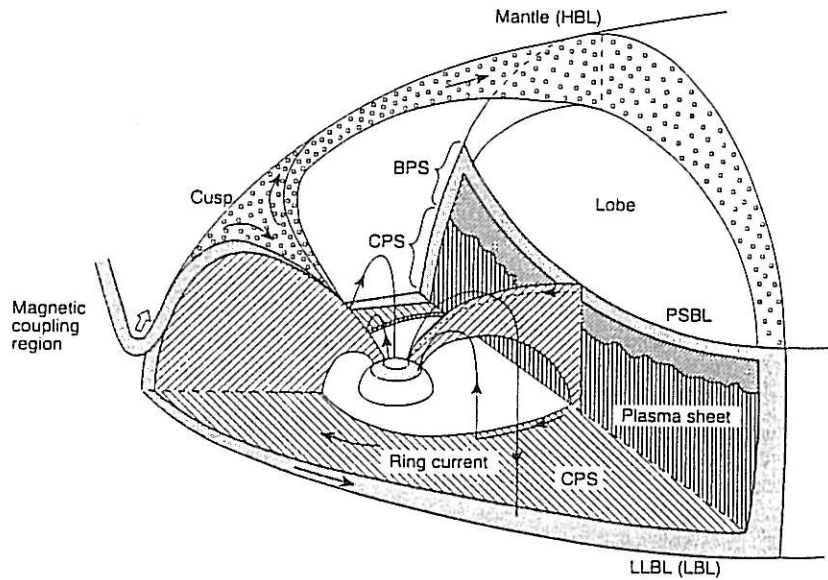
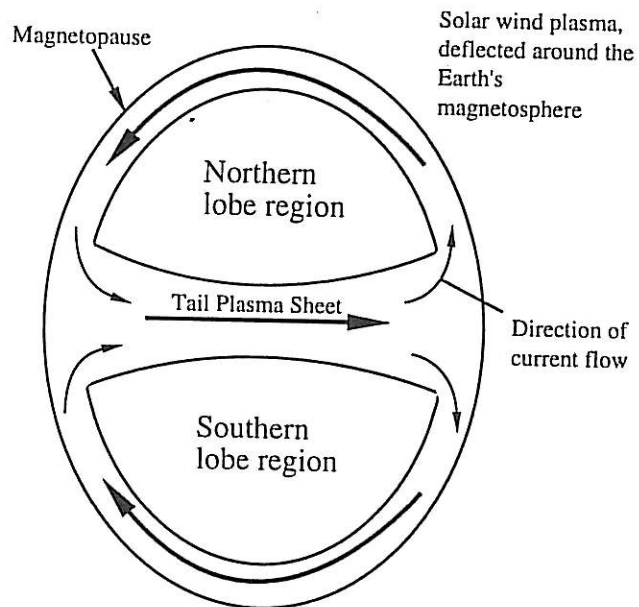


Figure 6

Large scale current flows in the Earth's magnetic tail. The diagram is a schematic of a cross-section of the Earth's tail, looking in the direction of the Sun (and Earth).



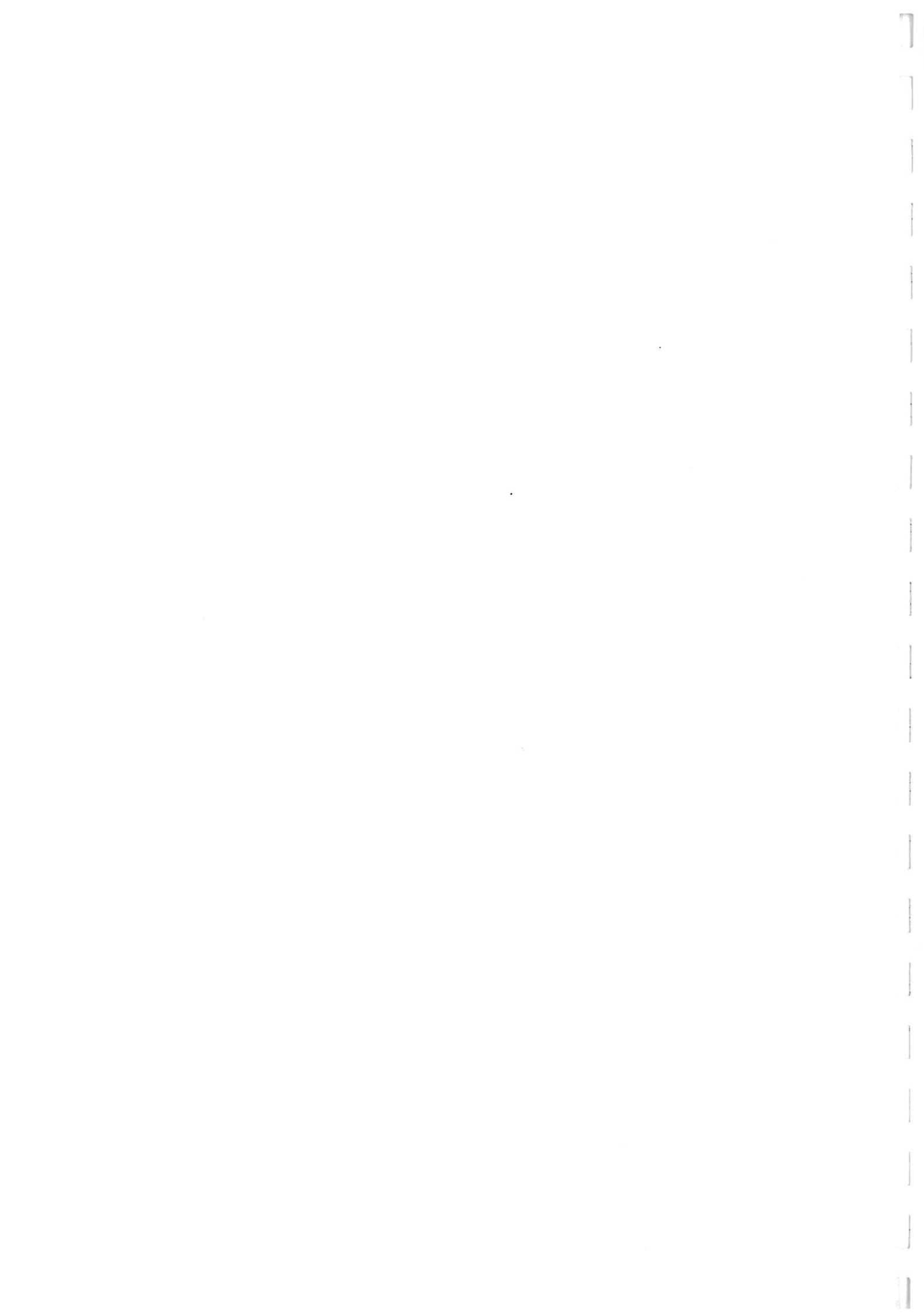


Figure 7

Illustrating the effects leading to the Auroral Electrojets. At high altitudes both the electrons and ions (mainly protons) drift in the same direction.

At lower altitudes, ion collisions result in their motion being in the electric field direction (across the oval), whilst electrons still drift around the oval, and form the Eastward and Westward electrojets in the morning and evening sectors respectively.

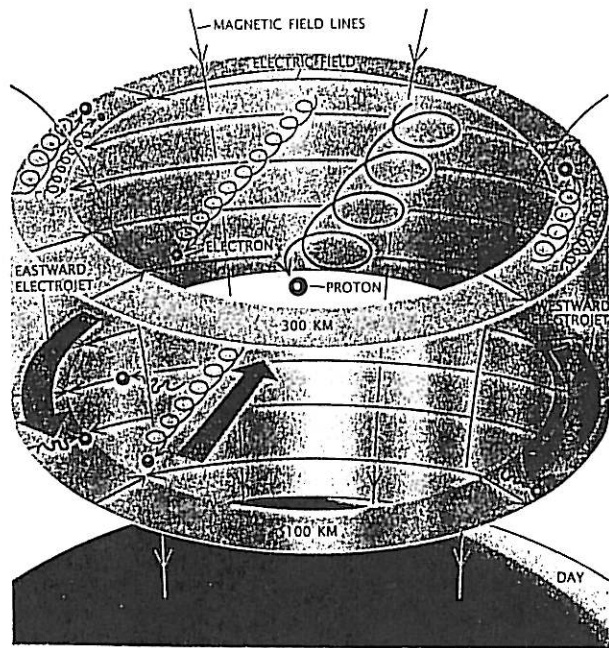


Figure 8

Showing the diffuse (unstructured) and discrete (structured) auroral statistic distributions, based on their heights in the ionosphere (the letters correspond to ionospheric layers; c.f. figure 3). Although the diffuse aurora is usually of sub-visual intensity, it occurs over as large an area (if not larger) as the more spectacular discrete aurora.

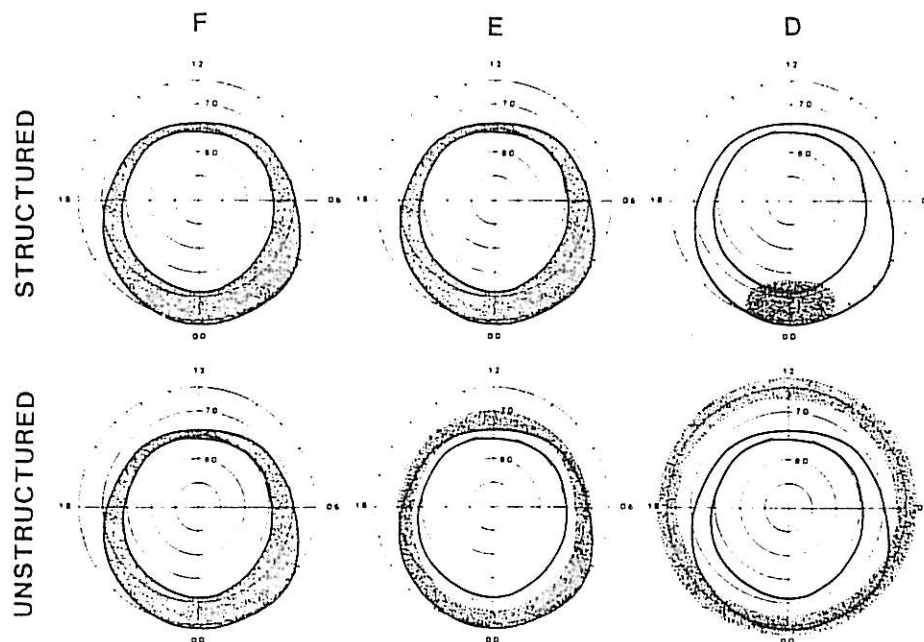


Figure 9

A contour plot showing the statistical occurrence of discrete aurora. The lines superimposed on these plots correspond to region one currents (thick lines) and region two currents (thin lines). Notice the increased auroral activity in the second plot, associated with a higher Kp value. Note also the strong correlation between region one currents and discrete aurora (darker shading on the contour plot).

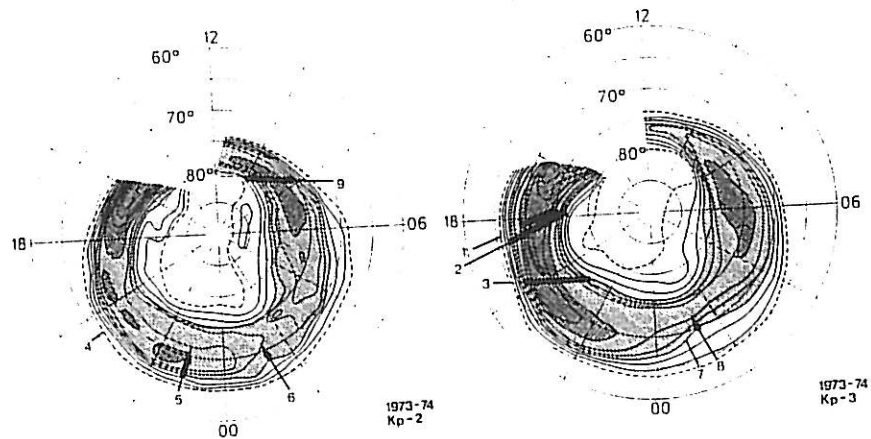
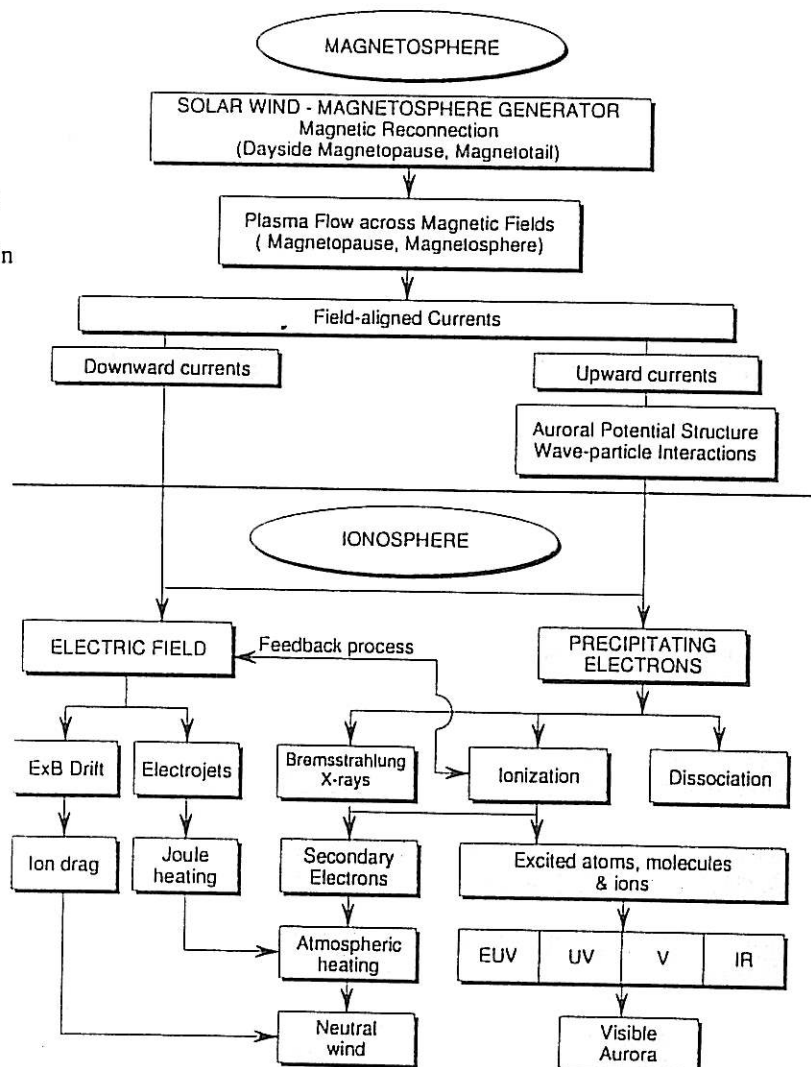


Figure 10

A summary diagram indicating relations between the effects and phenomena associated with the aurora, in both the ionosphere and magnetosphere.



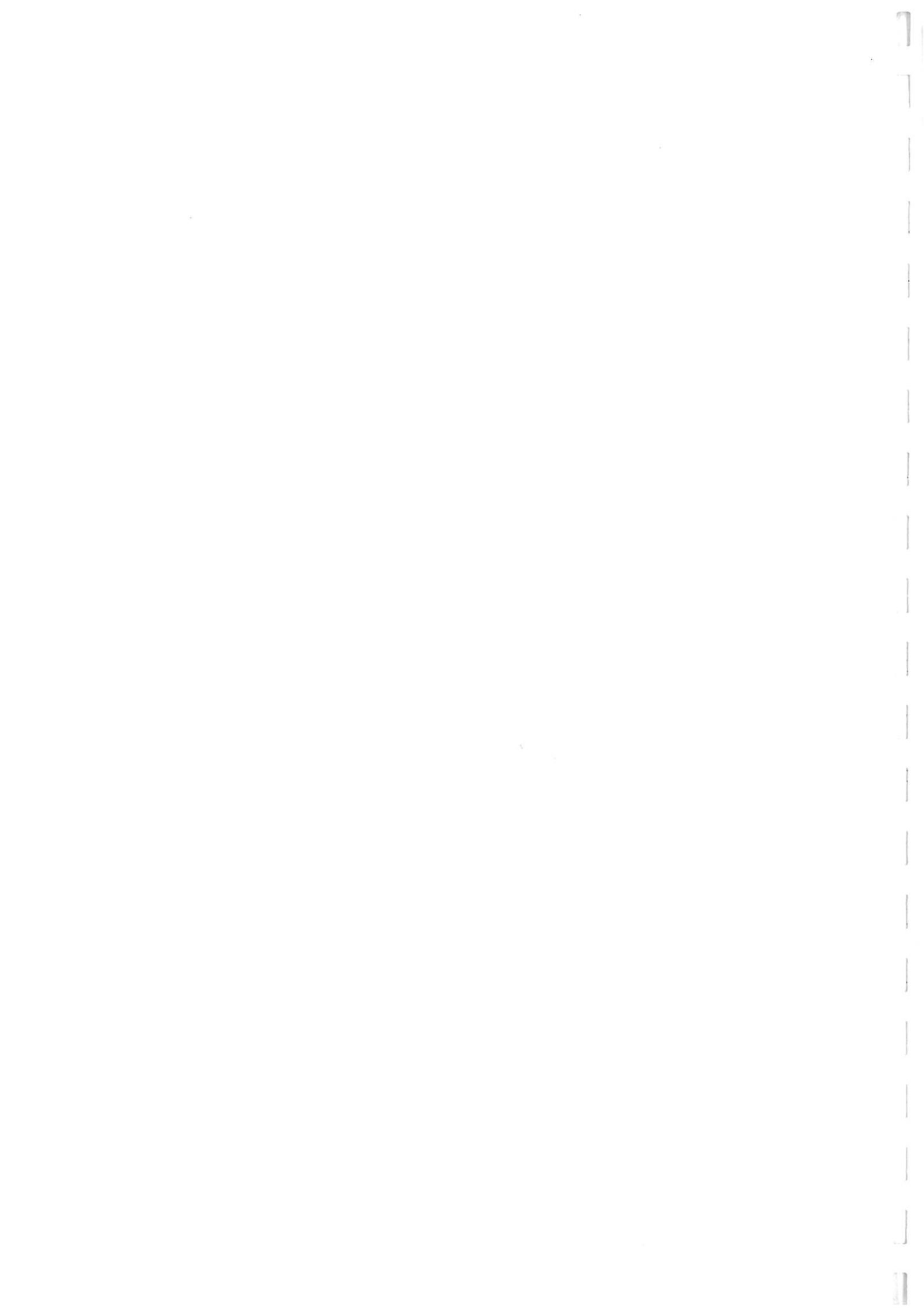


Figure 11

The diagrams shown below illustrate the evolution of a single substorm as described by Akasofu (1964). The starting condition is with some weak sun-aligned arcs over the pole, and limited nightside activity.

In B the most equatorward arc near midnight has intensified, and by C the beginnings of the wave shapey associated with the westward travelling surge have developed (note also the disappearance of the polar arcs).

As the storm progresses, the westward travelling surge starts to reverse its poleward motion, and patchy aurora develops in the morning sector. After one to two hours the activity has almost returned to the initial state, but to reach it completely, (with the redevelopment of sun-aligned arcs), takes a further hour or two.

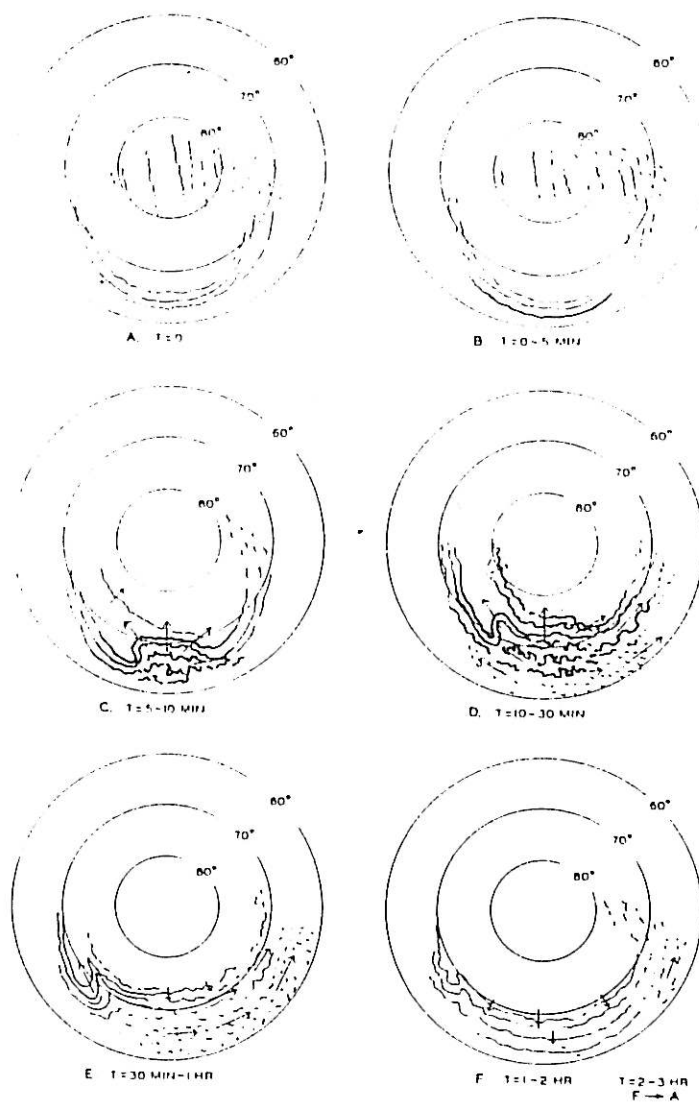




Figure 12a

Map showing the ground track of the rocket over Alaska, from its launch at Poker Flats, to the point of loss of signal over the Arctic Ocean. The numbers and crosses mark 100 seconds intervals in the flight.

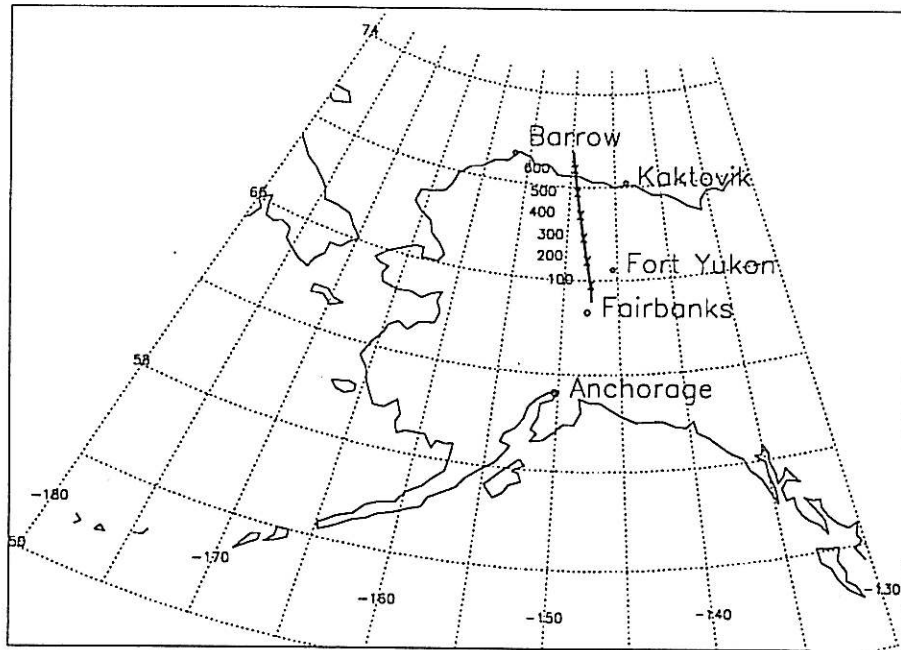
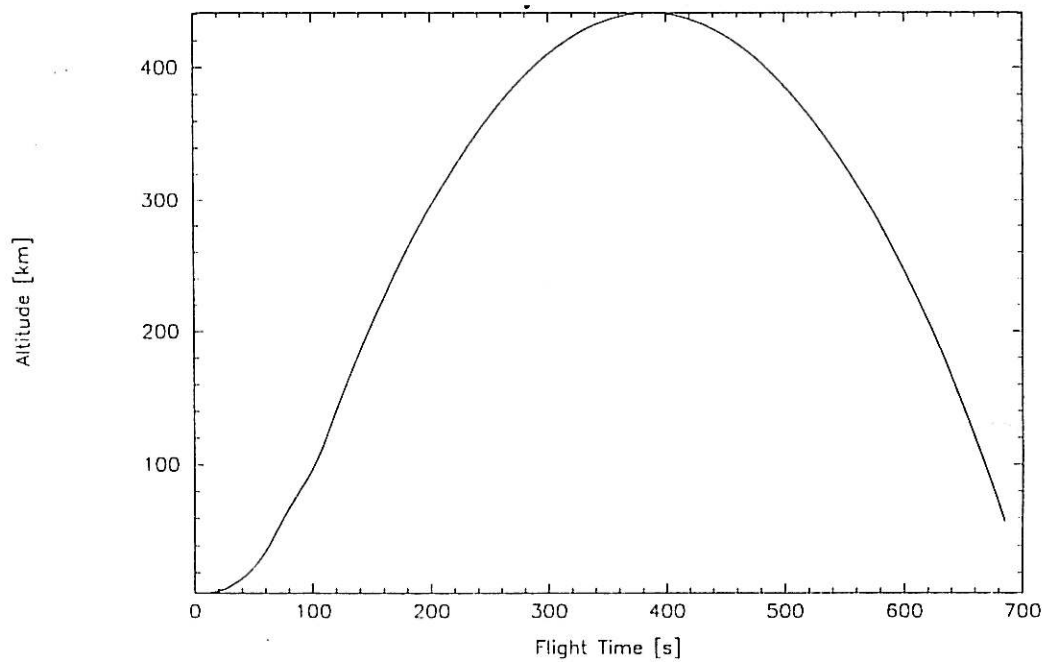


Figure 12b

Showing the altitude of the payload as a function of time. Note the abrupt changes of climb rate associated with rocket burns; and the following near ballistic trajectory.



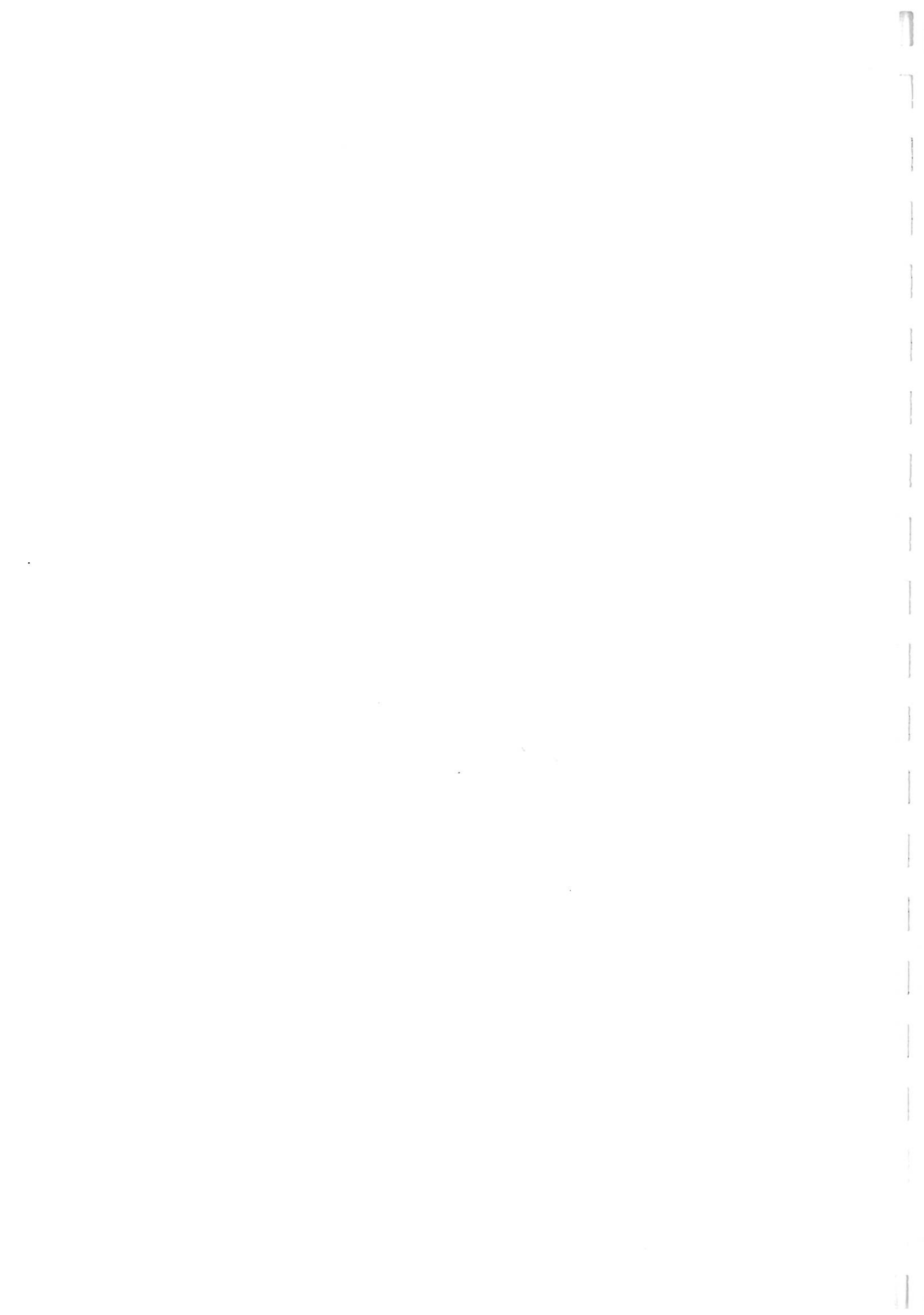


Figure 13

Electron Spectral Analyser Data (supplied by Peria. Note the intensified precipitation starting at times around 210 and 270 seconds after launch. The horizontal lines extending from these are beleived to be caused by instrument error (Peria, private communication)

Turbulence e- ESA 5A

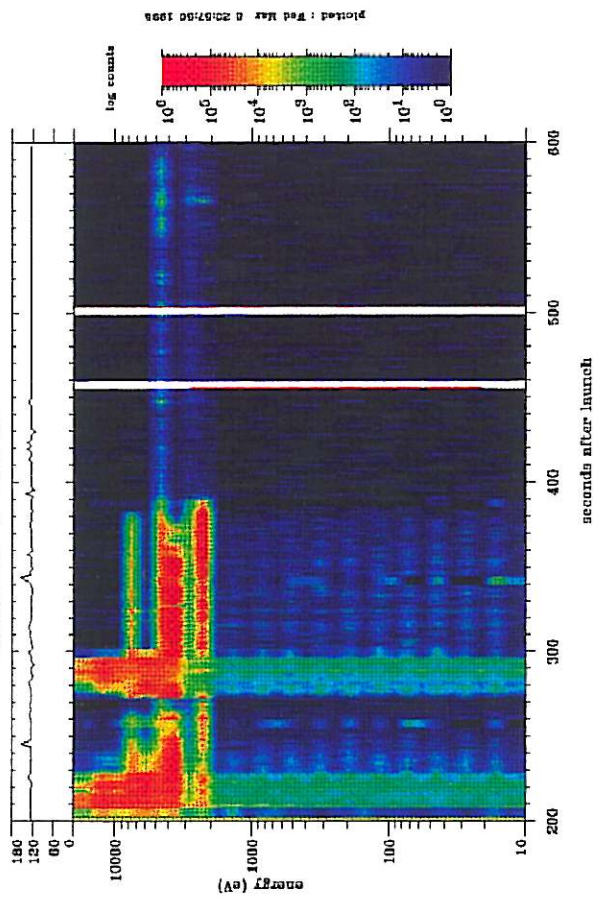
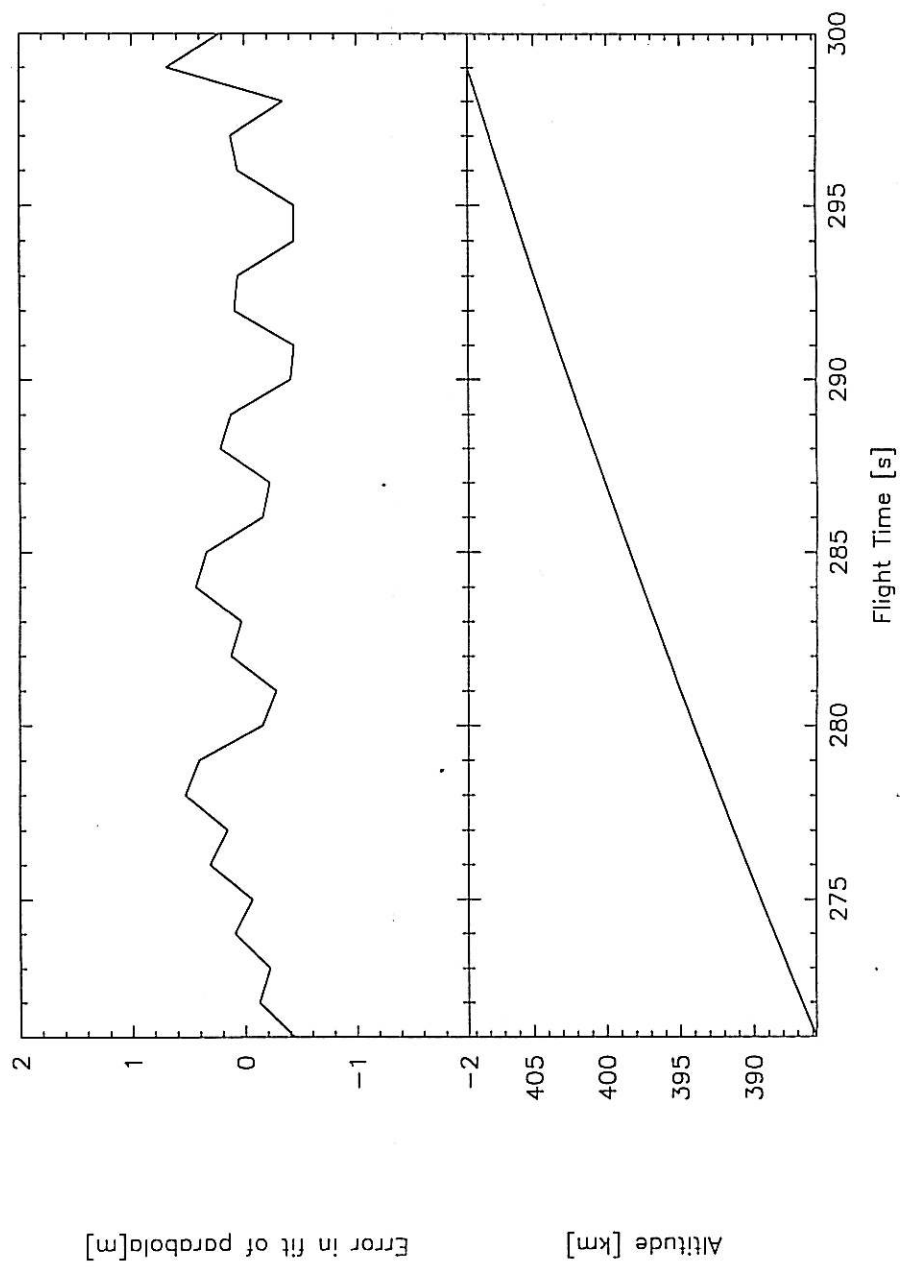


Figure 14 -- Altitude During Arc Traversal



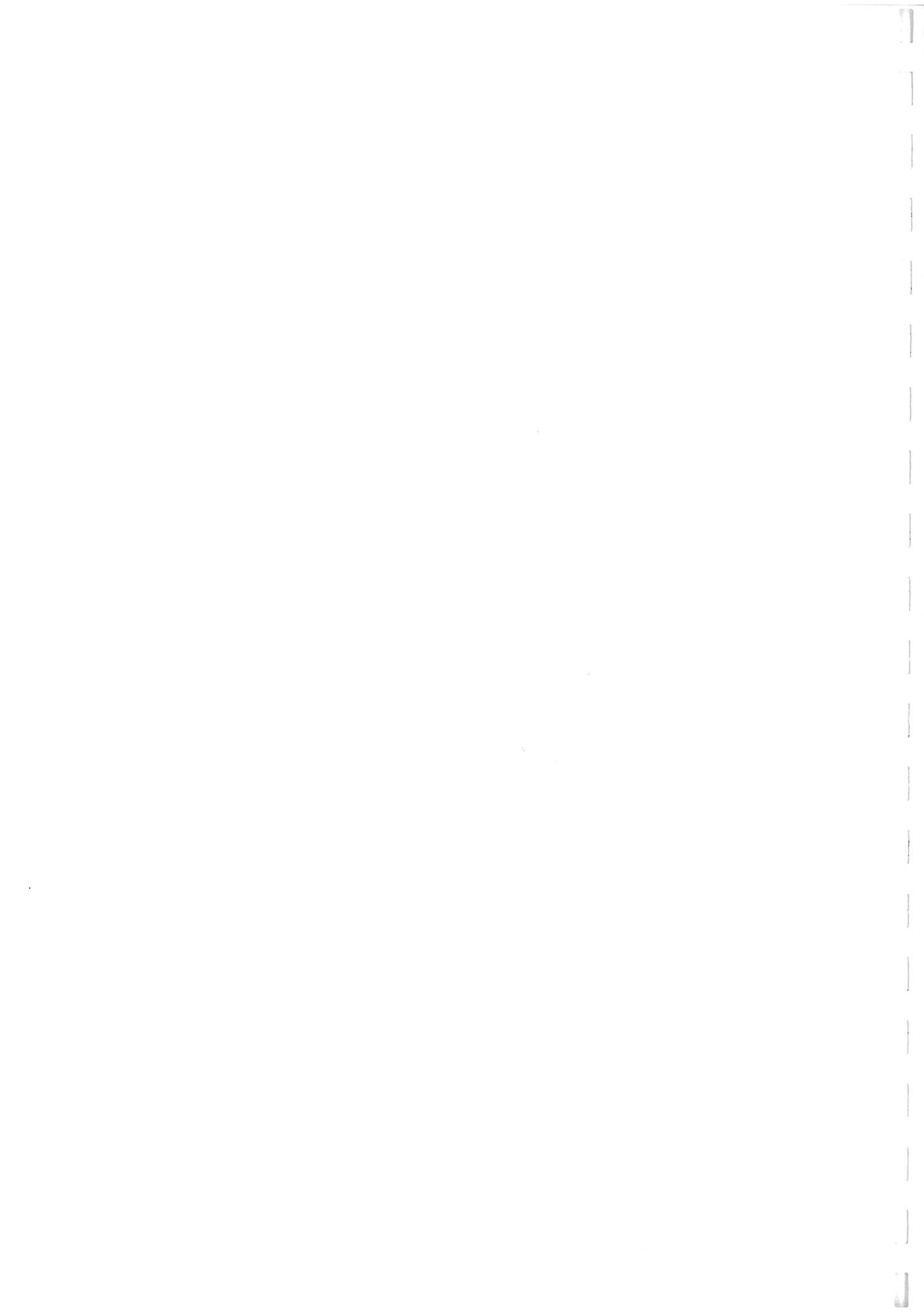


Figure 15 – Standard Deviations of Parabola Fitting

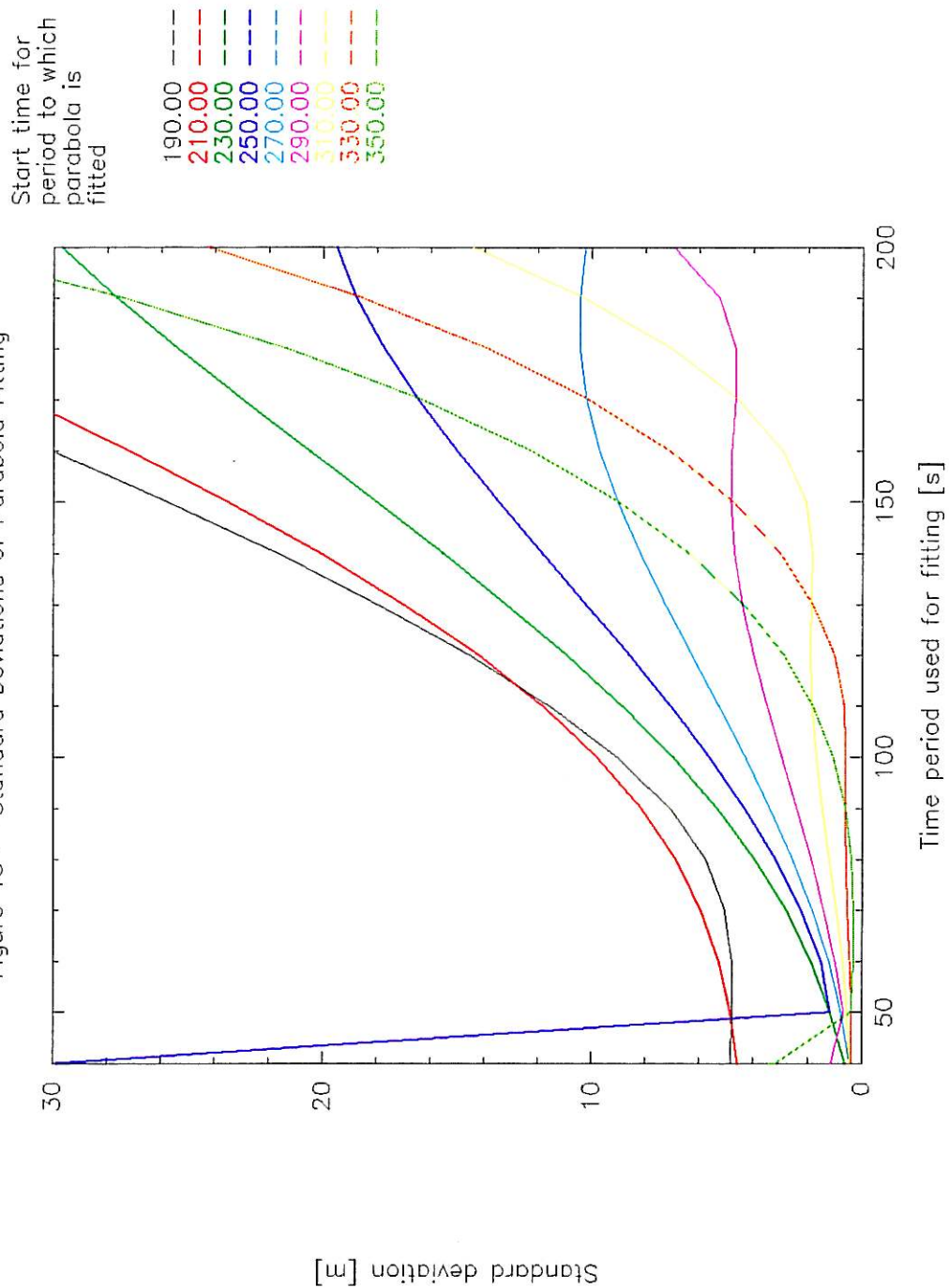


Figure 16 - Axis definitions for rocket

The rocket is shown by the cylinder, which is oriented in the inertial frame defined by the x , y and z -axes. In this frame the rocket's orientation is defined by the Euler angles θ , ϕ and ψ .

The principal axes of the rocket are denoted 1, 2 and 3, with the long axis represented by the 3 axis. The 1 axis is perpendicular to the 3 axis and lies in the plane defined by the z , and 3 axes. The 2 axis is so as to complete a right handed set.

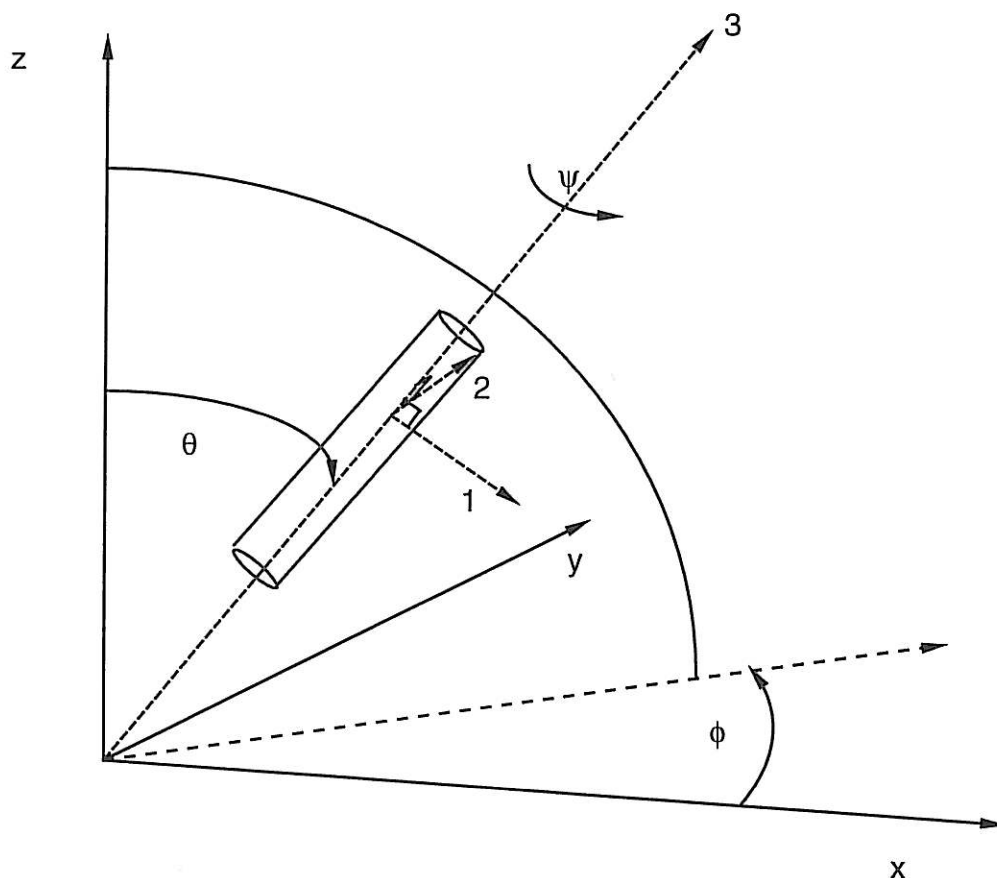
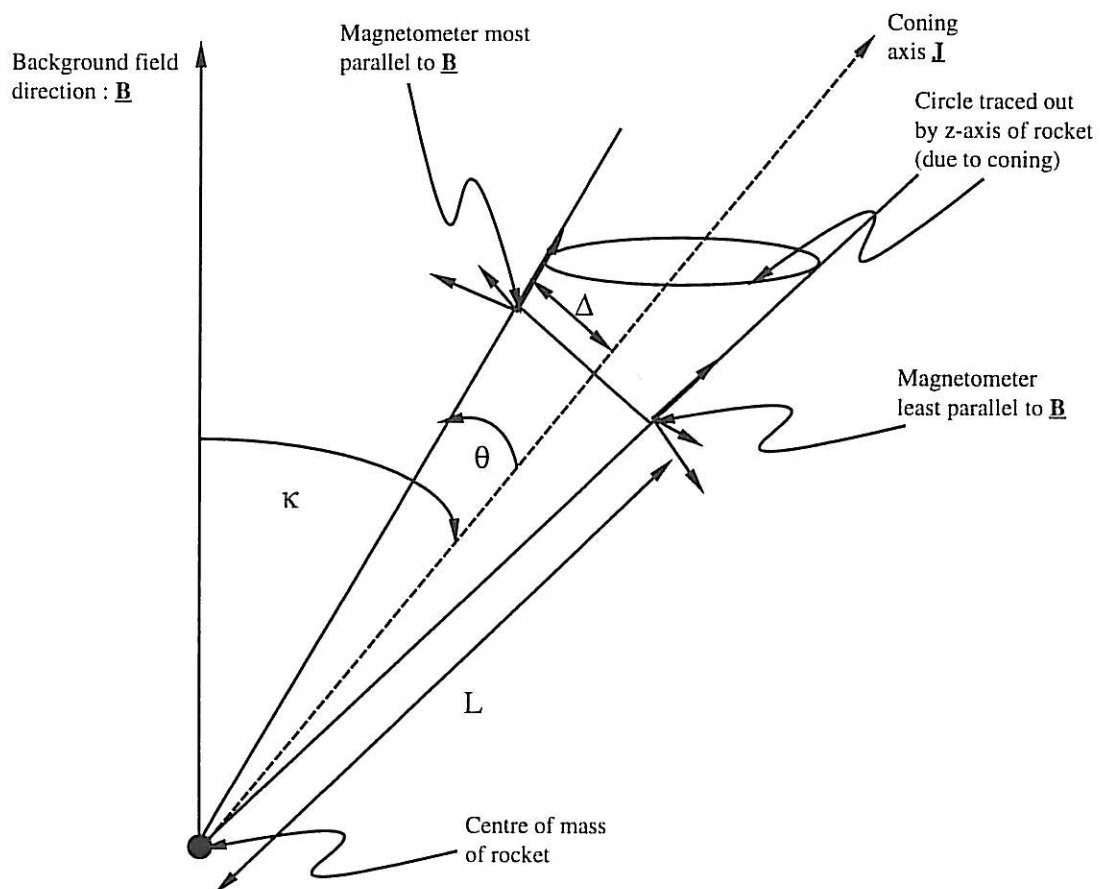


Figure 17 - Movement of magnetometer due to displacement from rocket centre of mass

This diagram illustrates the two extreme points of the coning motion, which causes the greatest movement of a point not at the centre of mass. Here the magnetometer is a distance L from the centre of mass, and undergoes a displacement of 2Δ . The magnetic field gradient referred to in the text (section 4.3) is directed along the line of Δ .



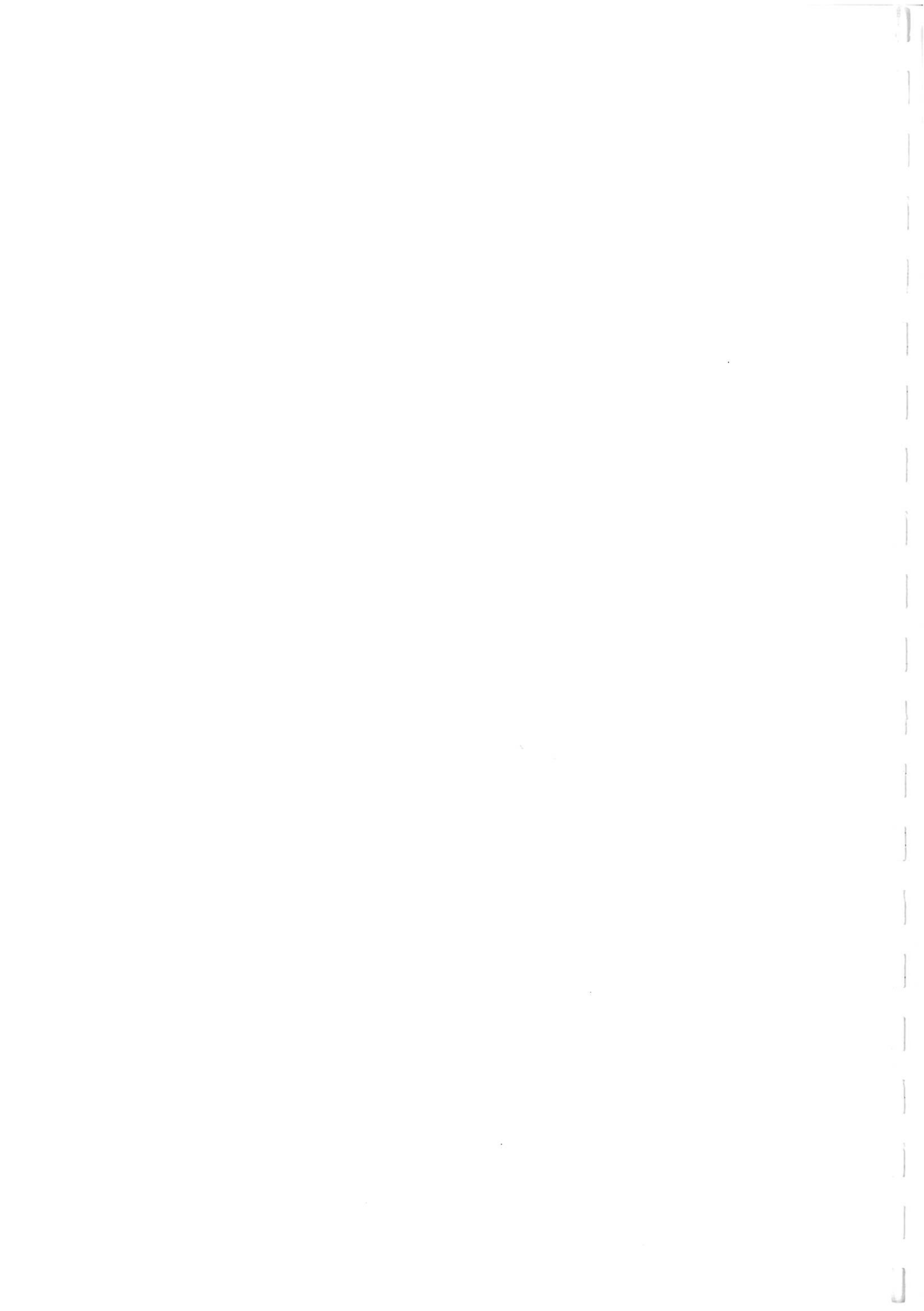
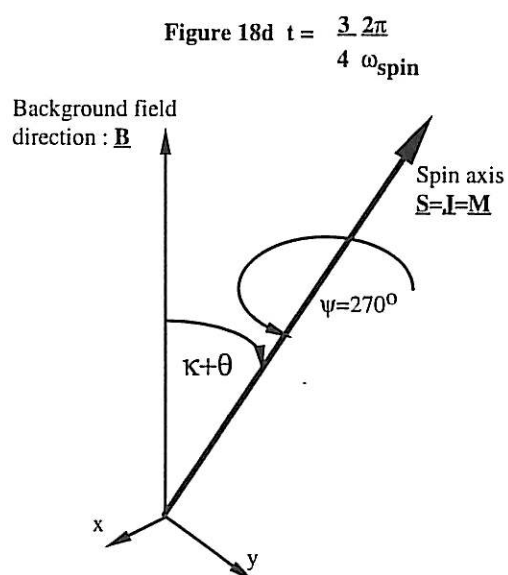
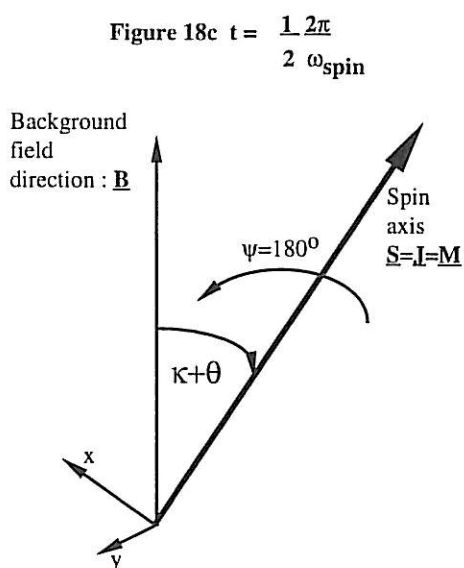
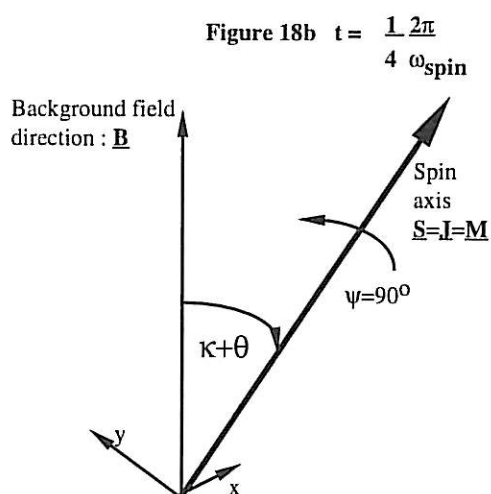
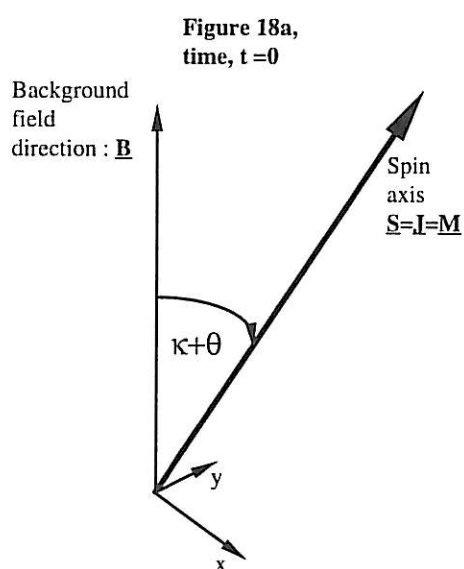


Figure 18 - Demonstration of spin motion

These figures show the orientation of the magnetometer in the case of spinning but no coning (section 4.4). The four diagrams show the situation at quarters of the spin period, where the spin frequency is ω_{spin} .



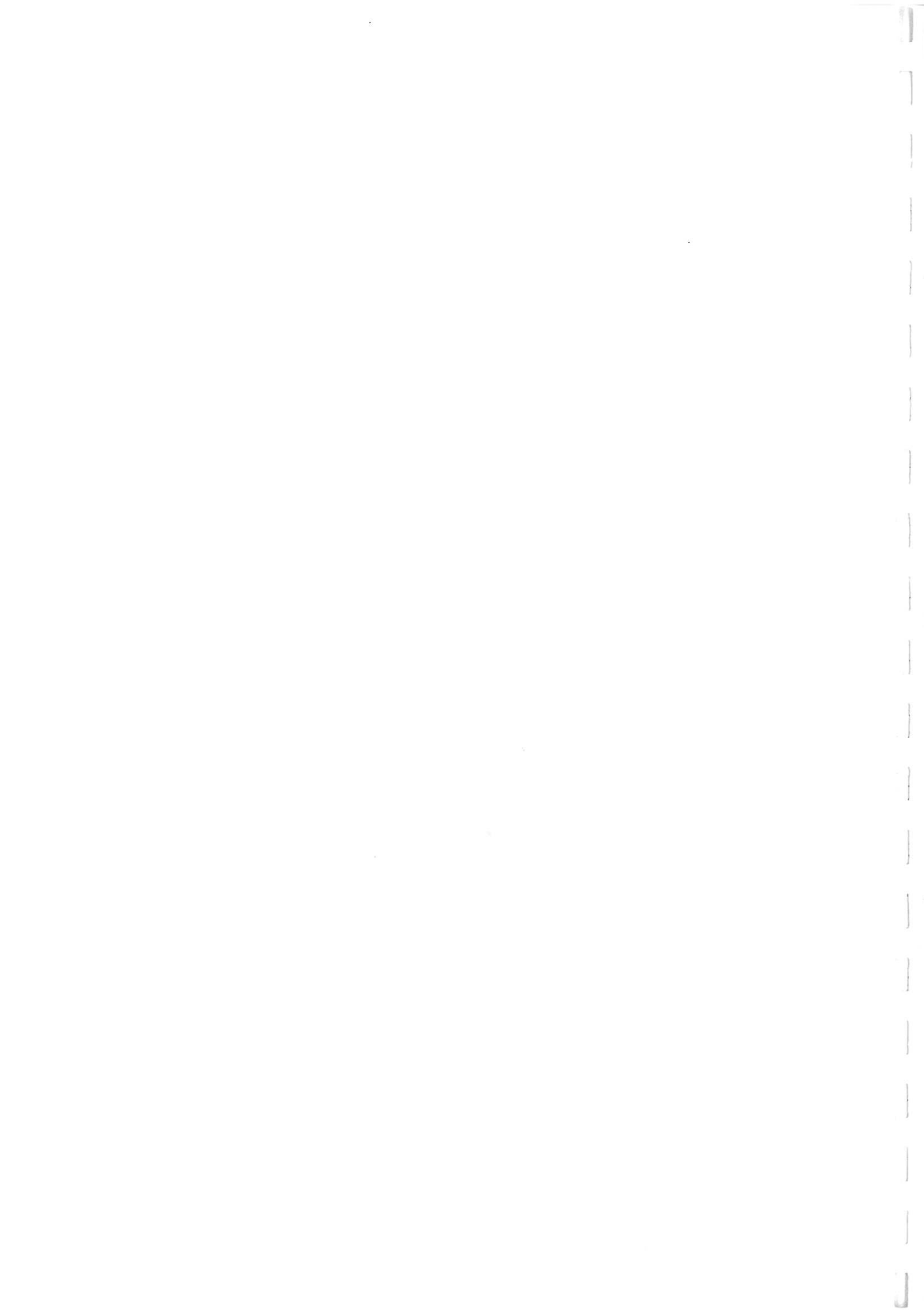


Figure 19 - Movement of magnetometer due to coning

These figures show the orientation of the magnetometer in the case of coning but no spinning (section 4.5). The four diagrams show the situation at quarters of the coning period, where the coning frequency is ω_{cone} .

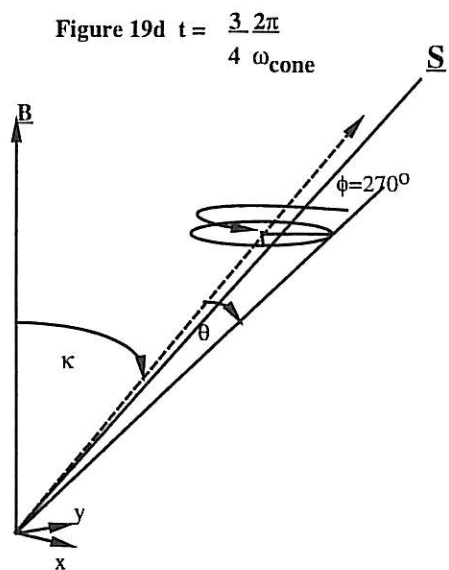
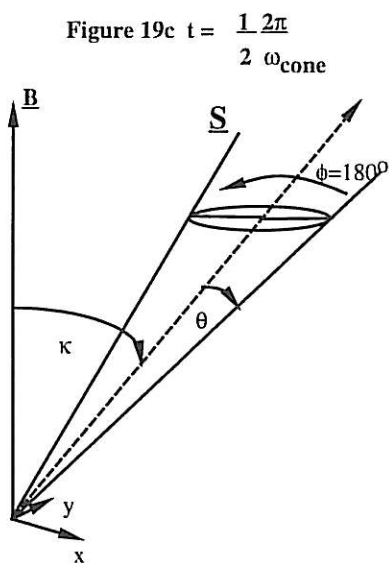
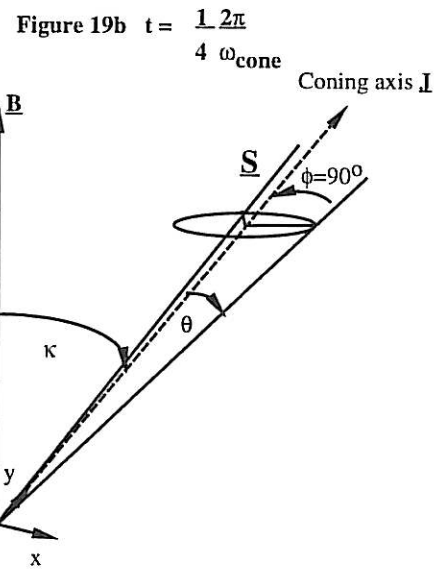
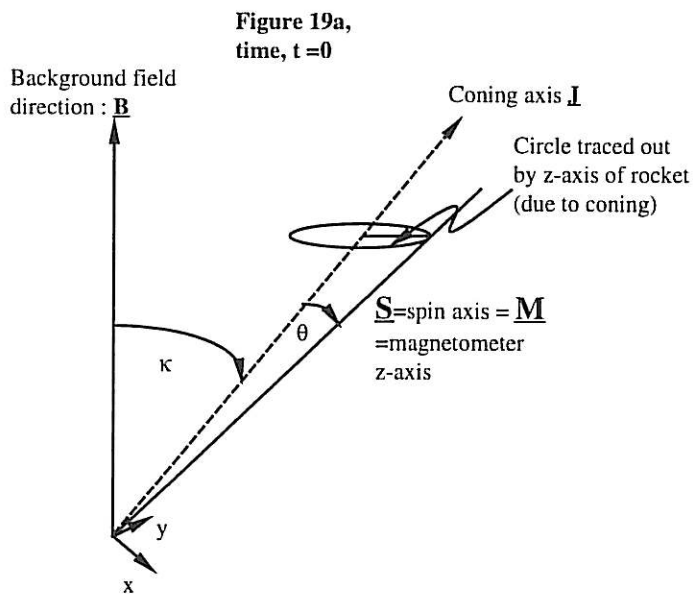


Figure 20 - Coning motion-projection into 2-dimensions

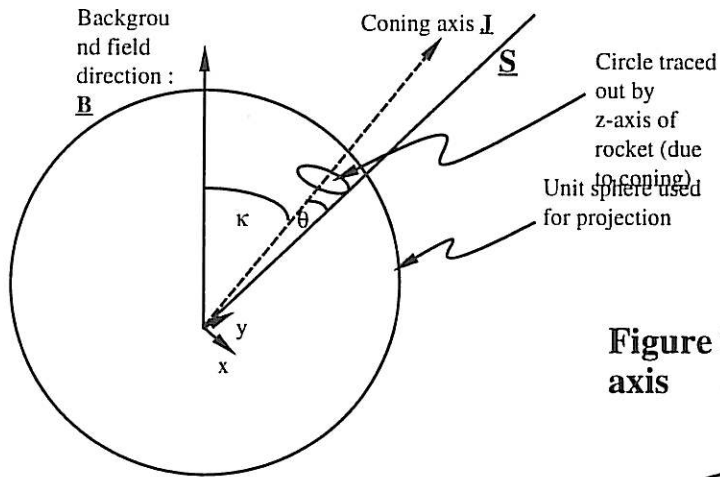


Figure 20a- Motion of the spin axis

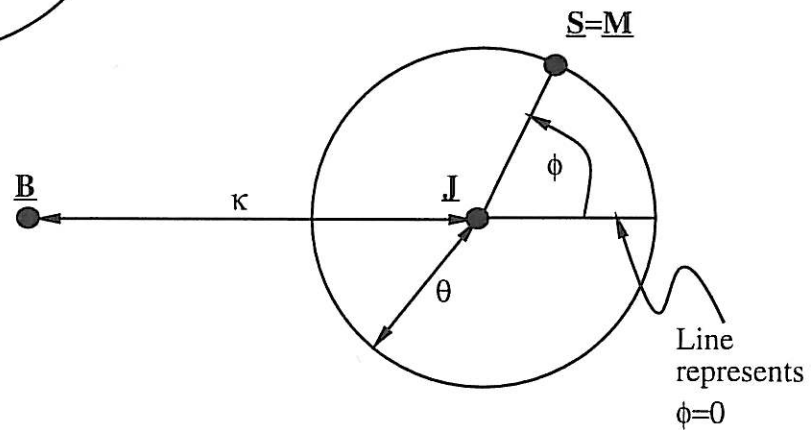
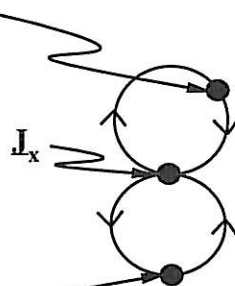


Figure 20b- Motion of the x axis

Instantaneous position of the x axis after just over half a coning period



Arrows indicate direction of motion of x-axis

Position of x-axis at $t=0$ (by definition of time origin)

Figure 21a -- Results from SIM1.FOR

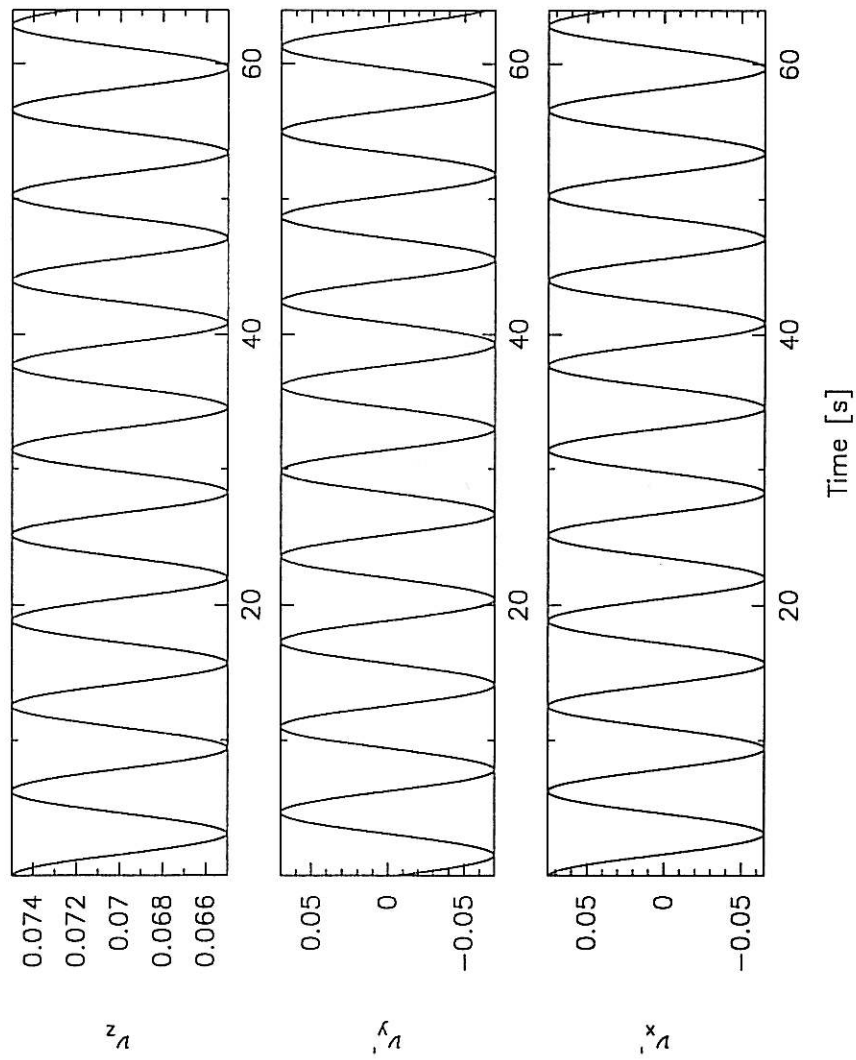




Figure 21b -- Results from SIM1.FOR

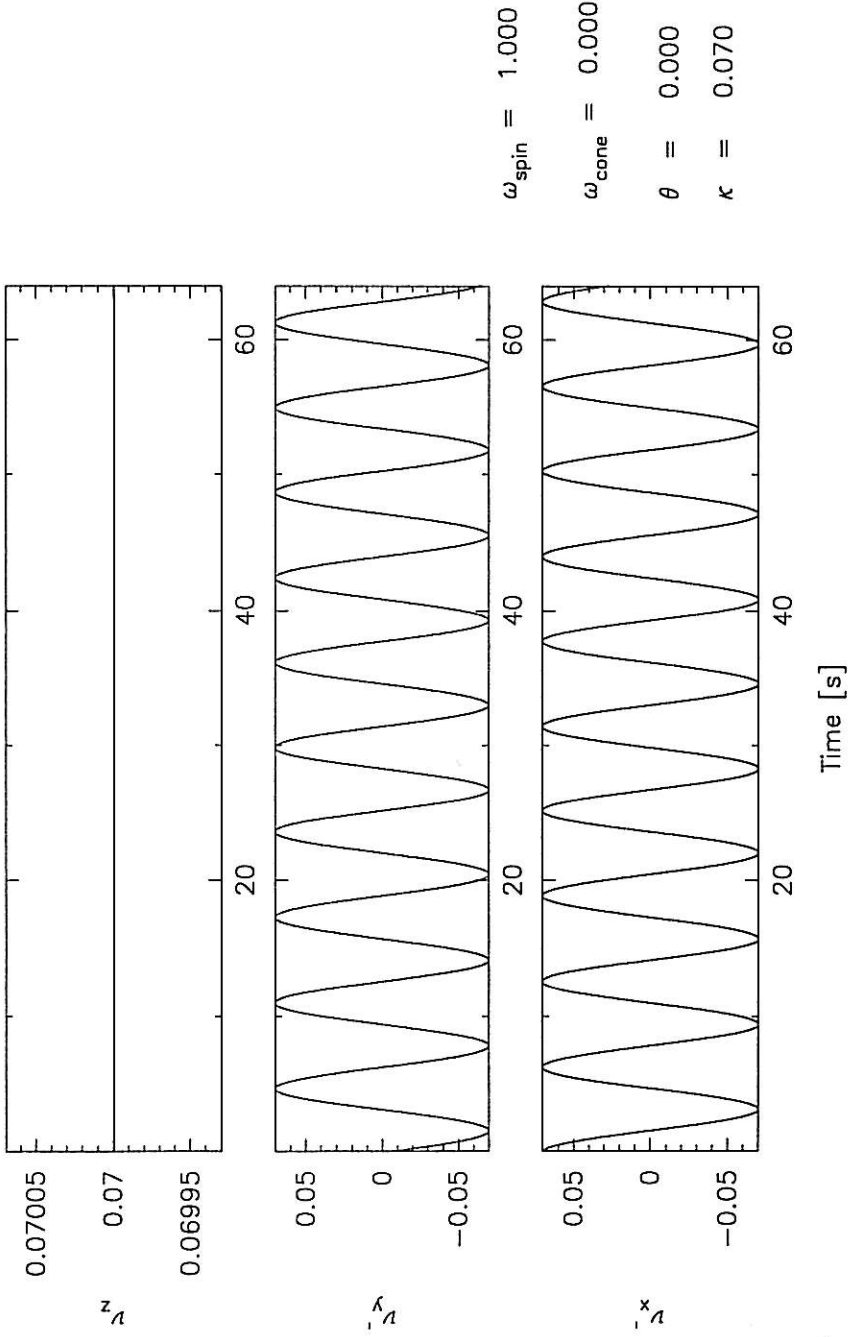
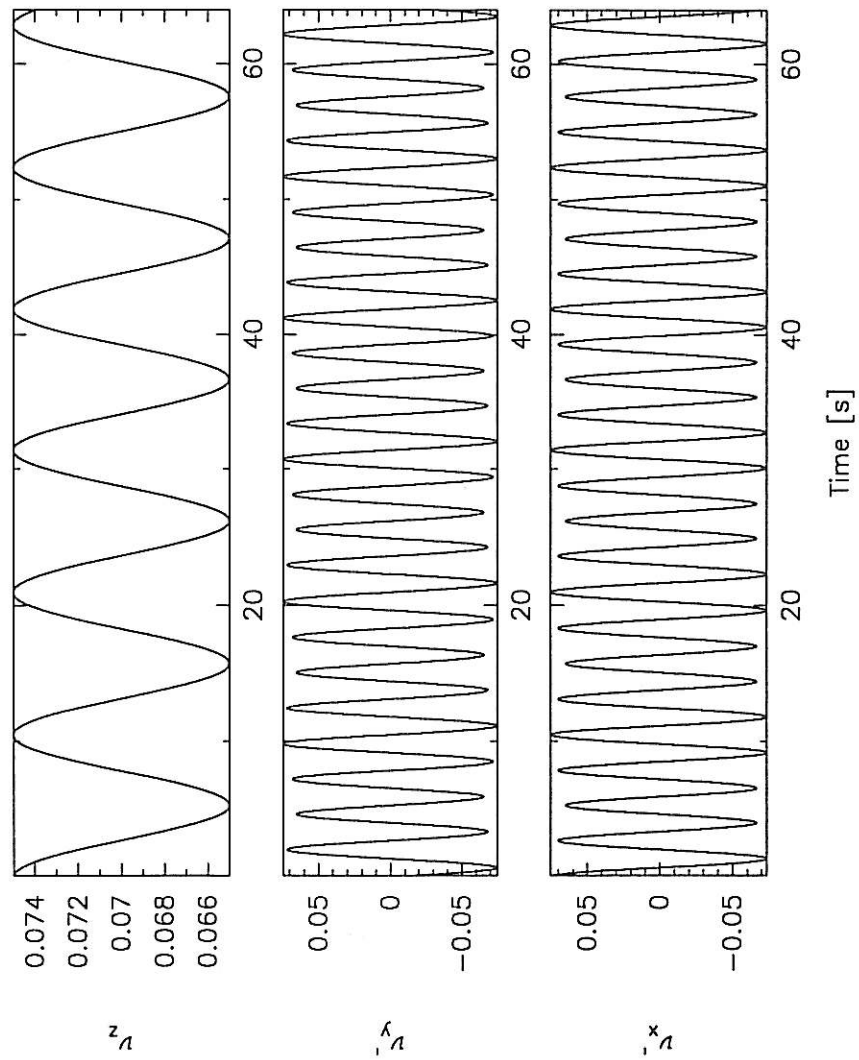


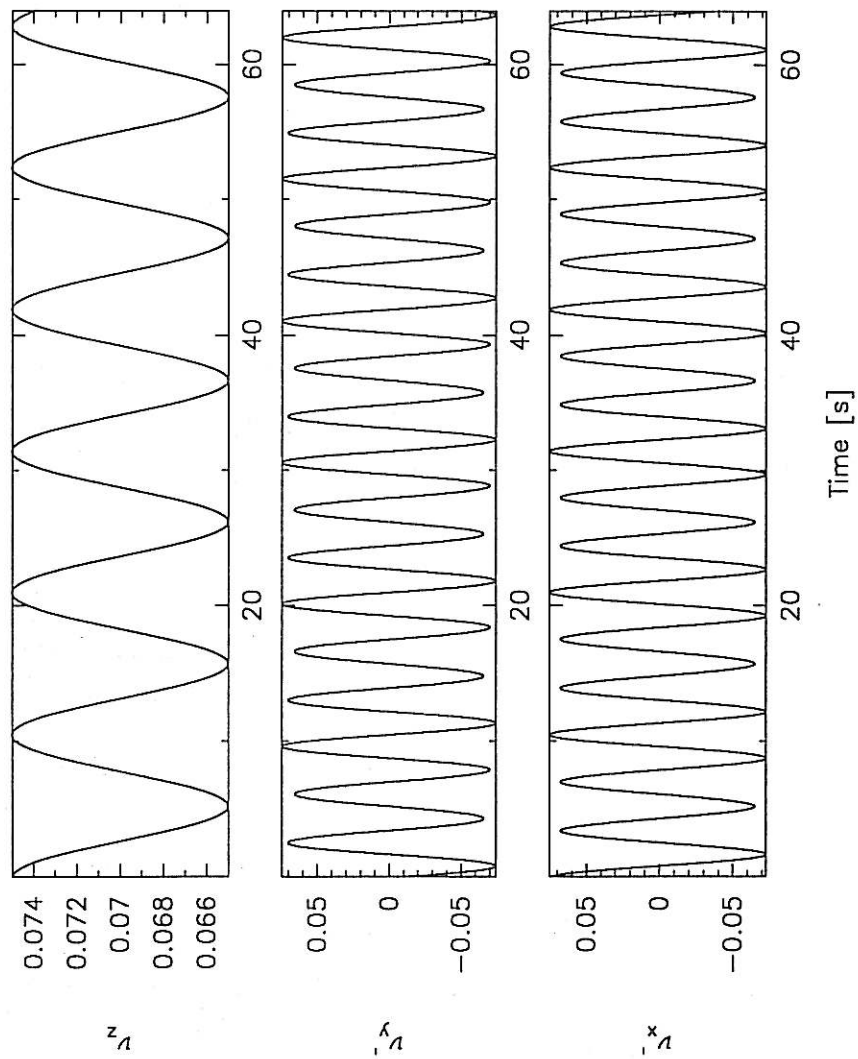


Figure 22a -- Results from SIM1.FOR



$\omega_{\text{spin}} = 1.800$
 $\omega_{\text{cone}} = 0.600$
 $\theta = 0.005$
 $\kappa = 0.070$

Figure 22b — Results from SIM1.FOR



$$\omega_{\text{spin}} = 1.800$$

$$\omega_{\text{cone}} = 0.600$$

$$\theta = 0.070$$

$$\kappa = 0.005$$

Figure 22c — Results from SIM1.FOR

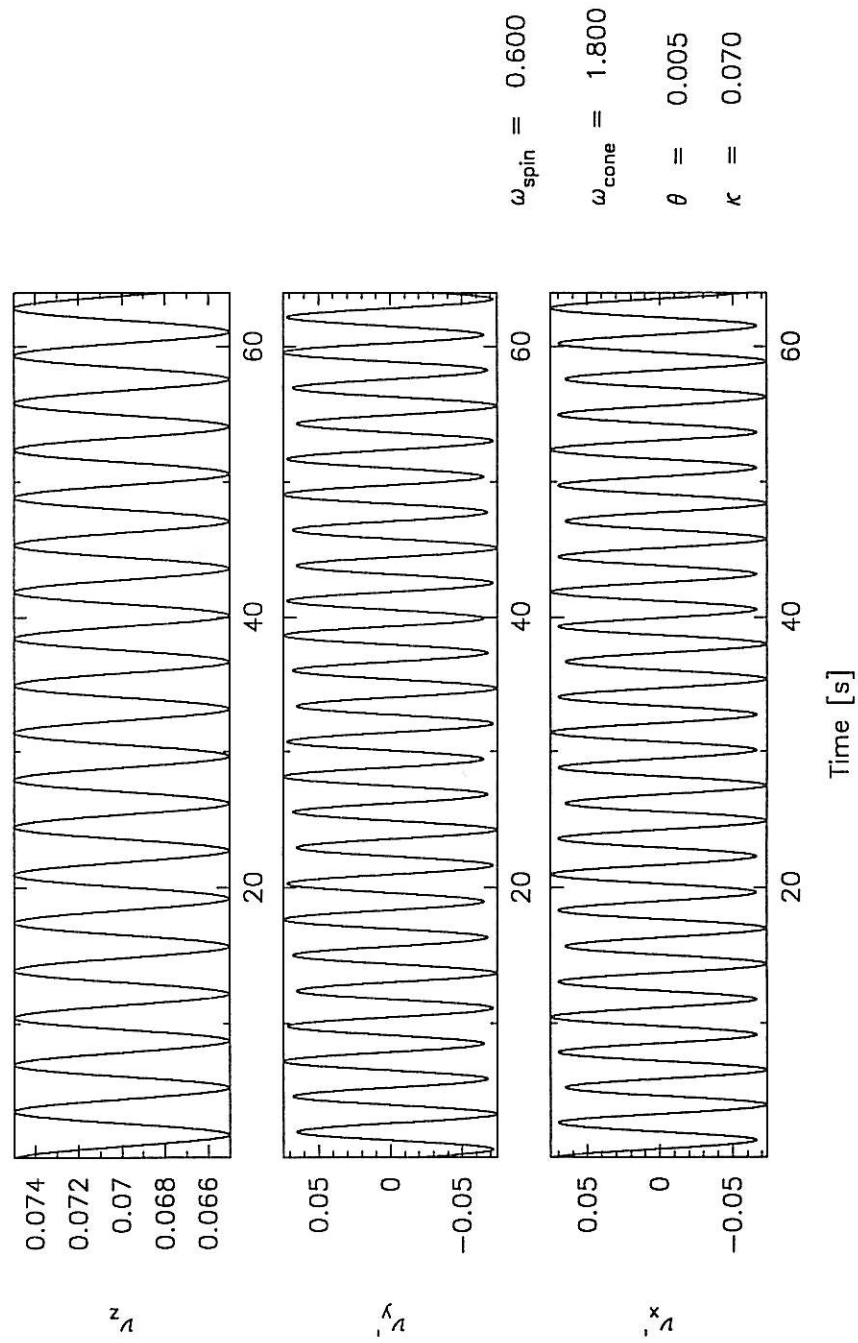
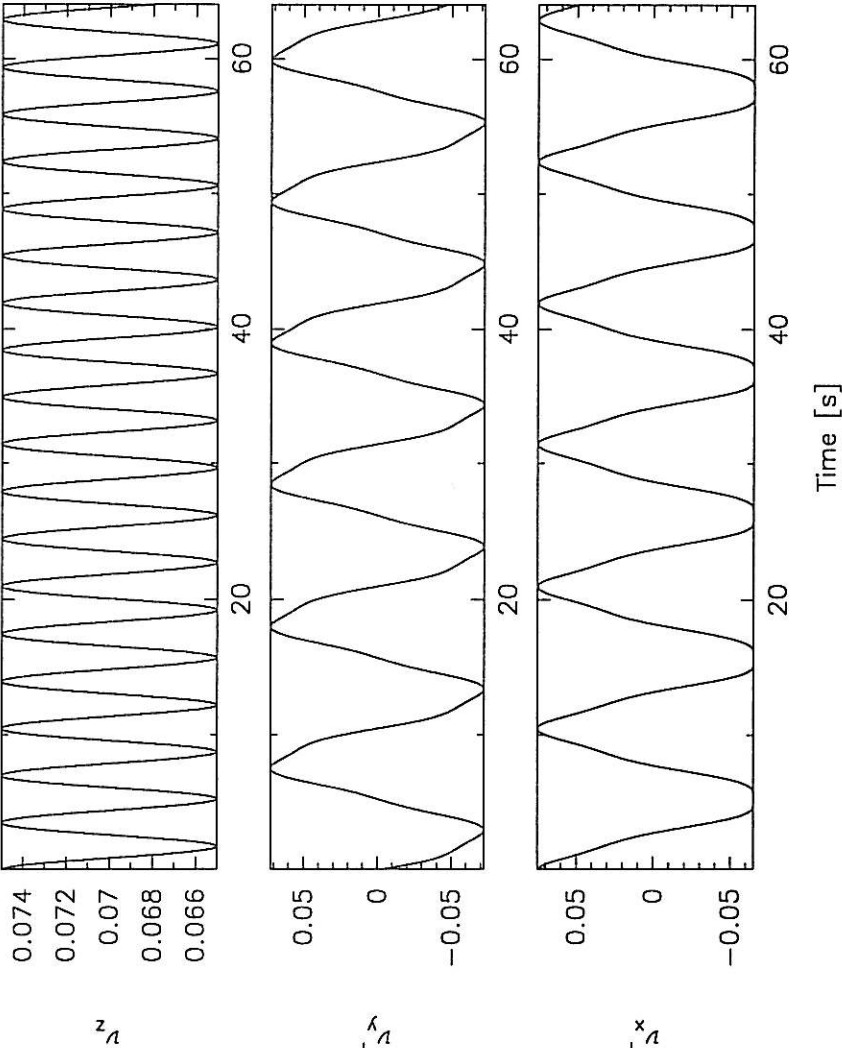


Figure 22d – Results from SIM1.FOR



$\omega_{\text{spin}} = 0.600$
 $\omega_{\text{cone}} = 1.800$
 $\theta = 0.070$
 $\kappa = 0.005$

Figure 23 - Definition of non-orthogonality angles

This diagram illustrates the definition of the three non-orthogonality angles α , β and γ (Bolin, 1994)

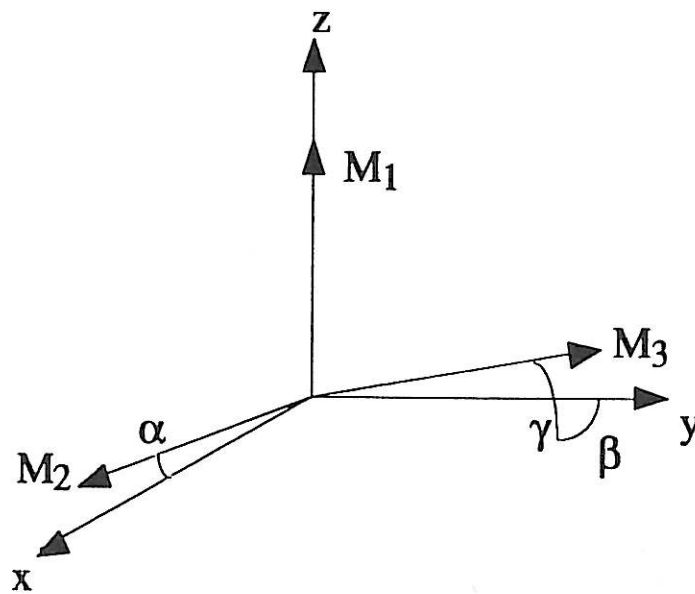
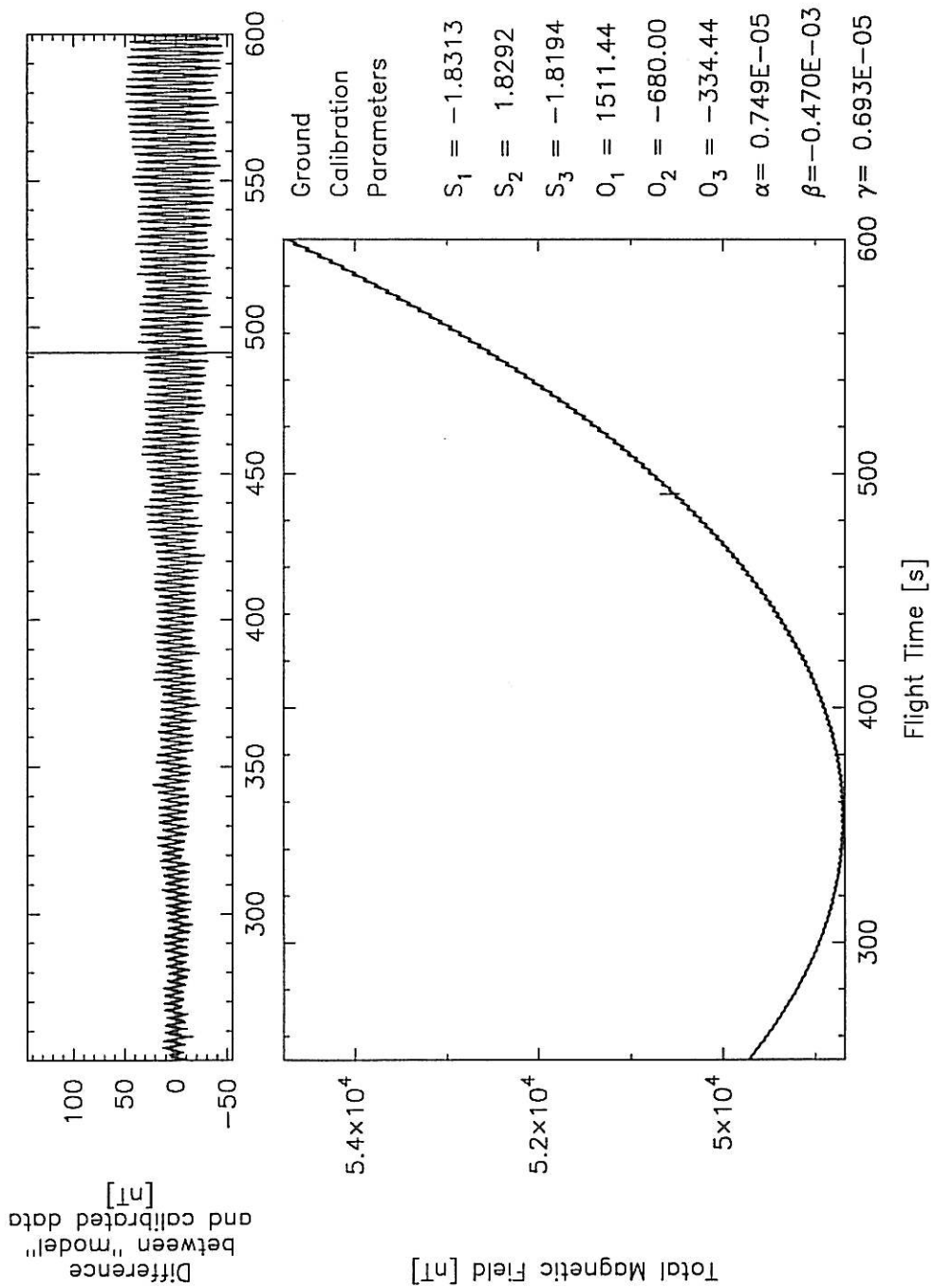


Figure 24 – Inputs to FPAM9.FOR



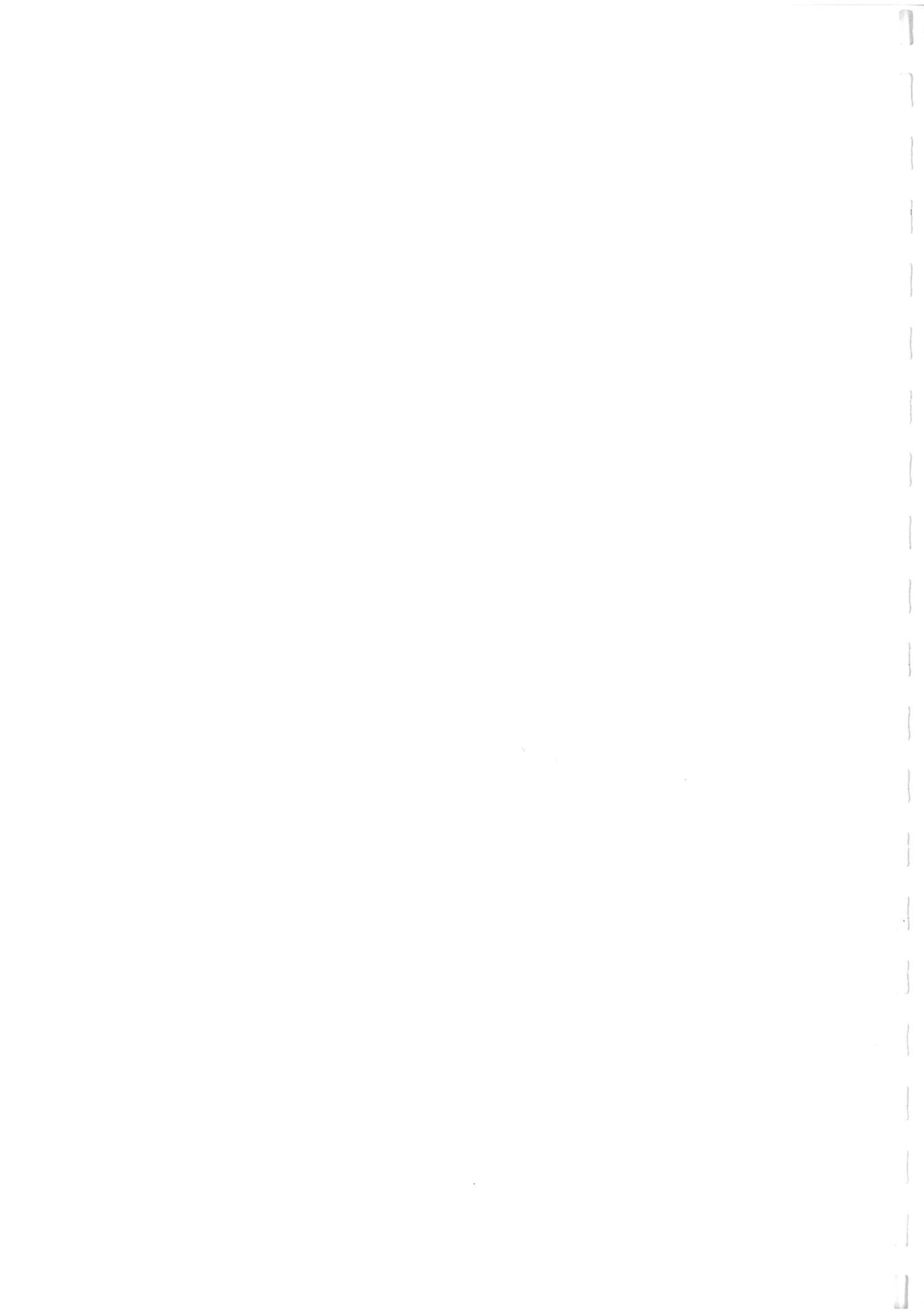
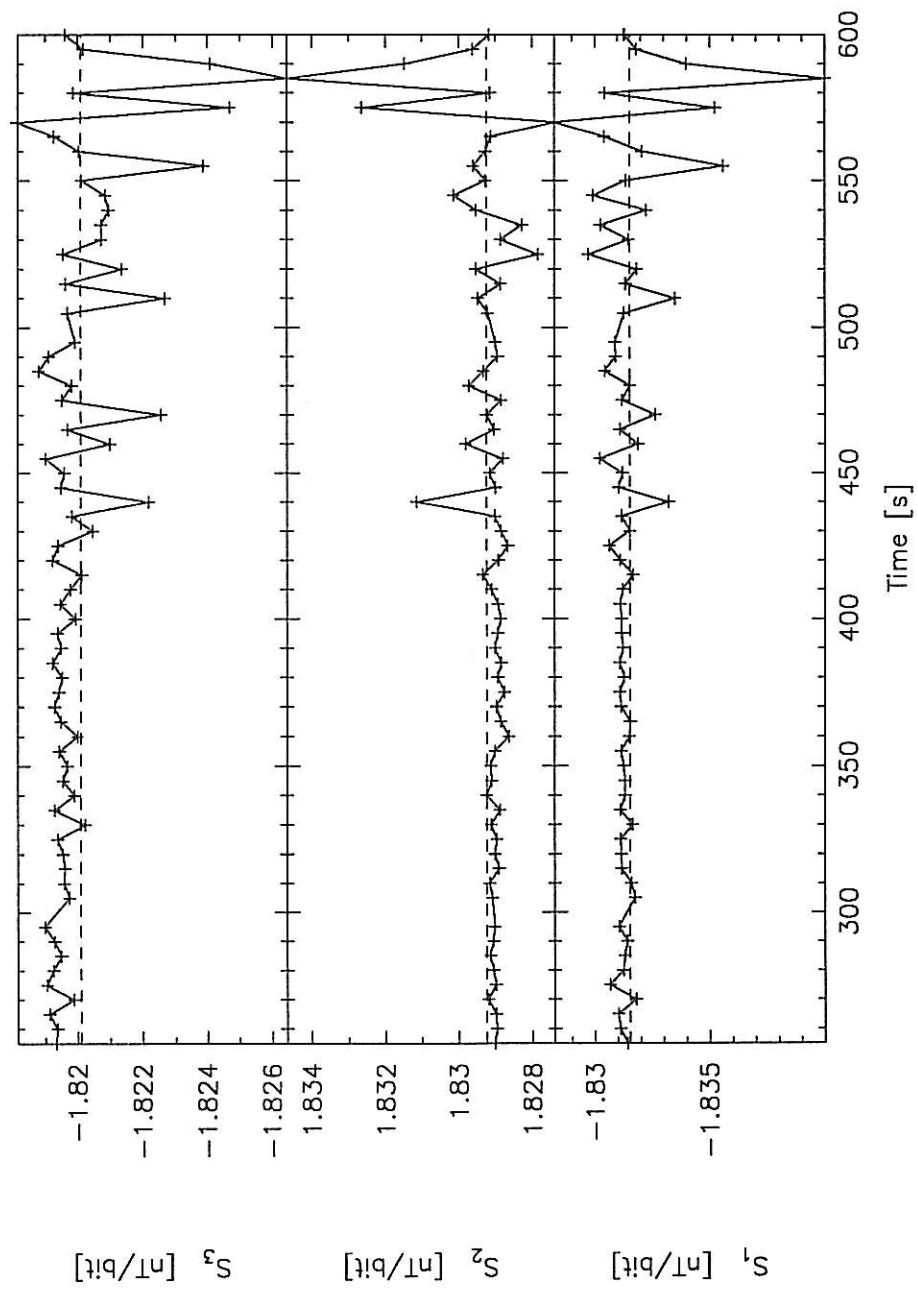


Figure 25a—Time Variation of Parameters Found by FPAM9



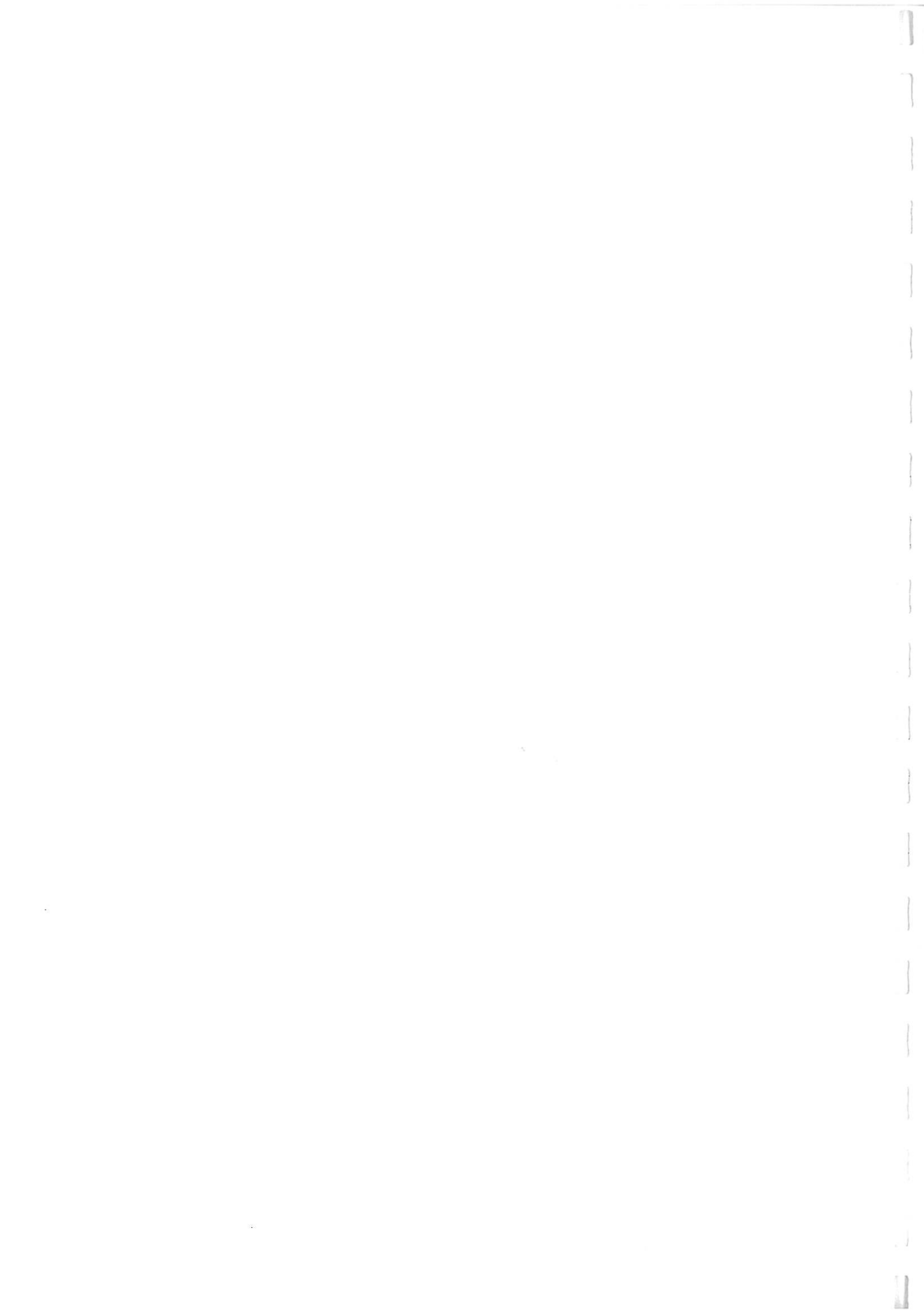
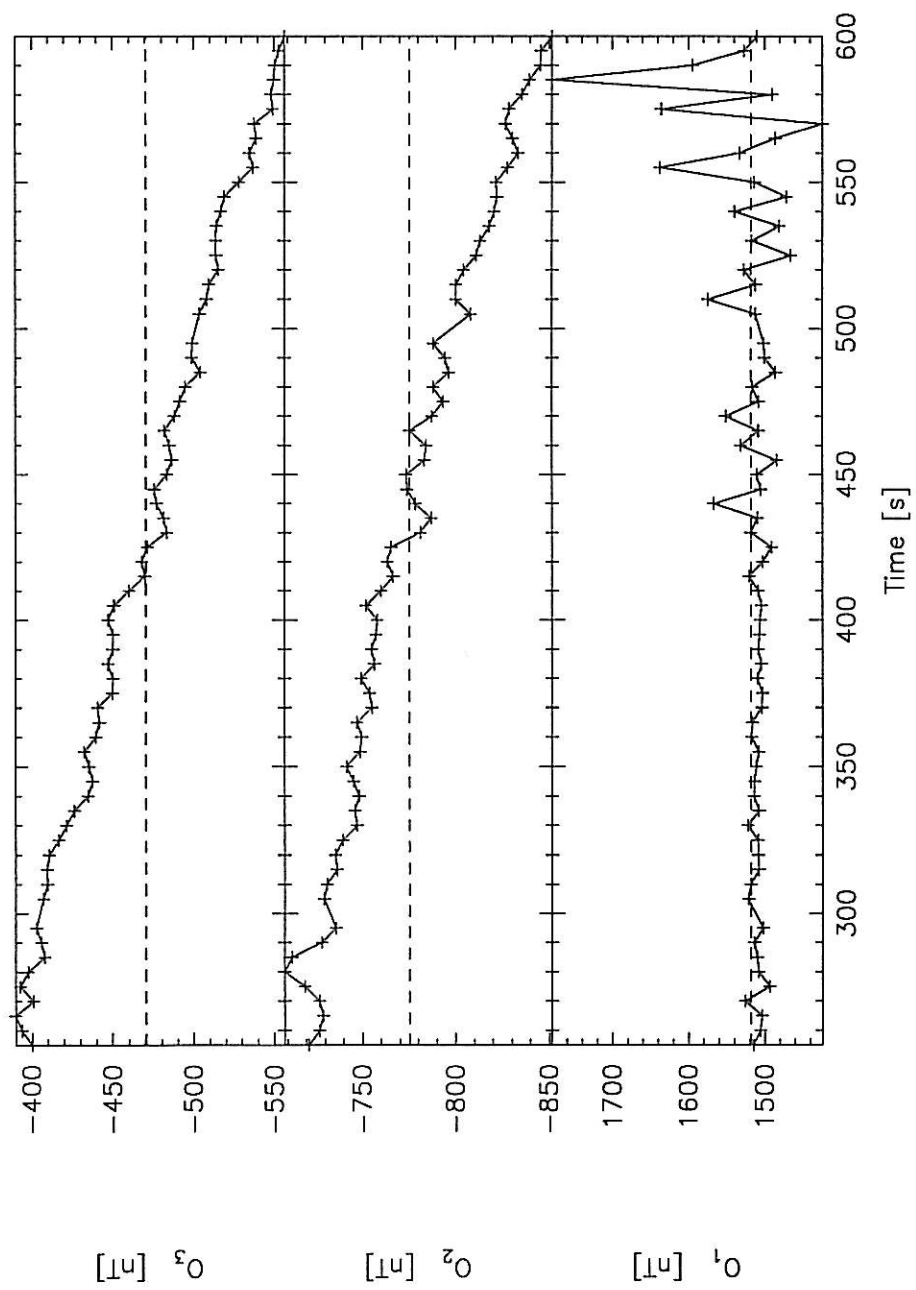


Figure 25b—Time Variation of Parameters Found by FPAM9



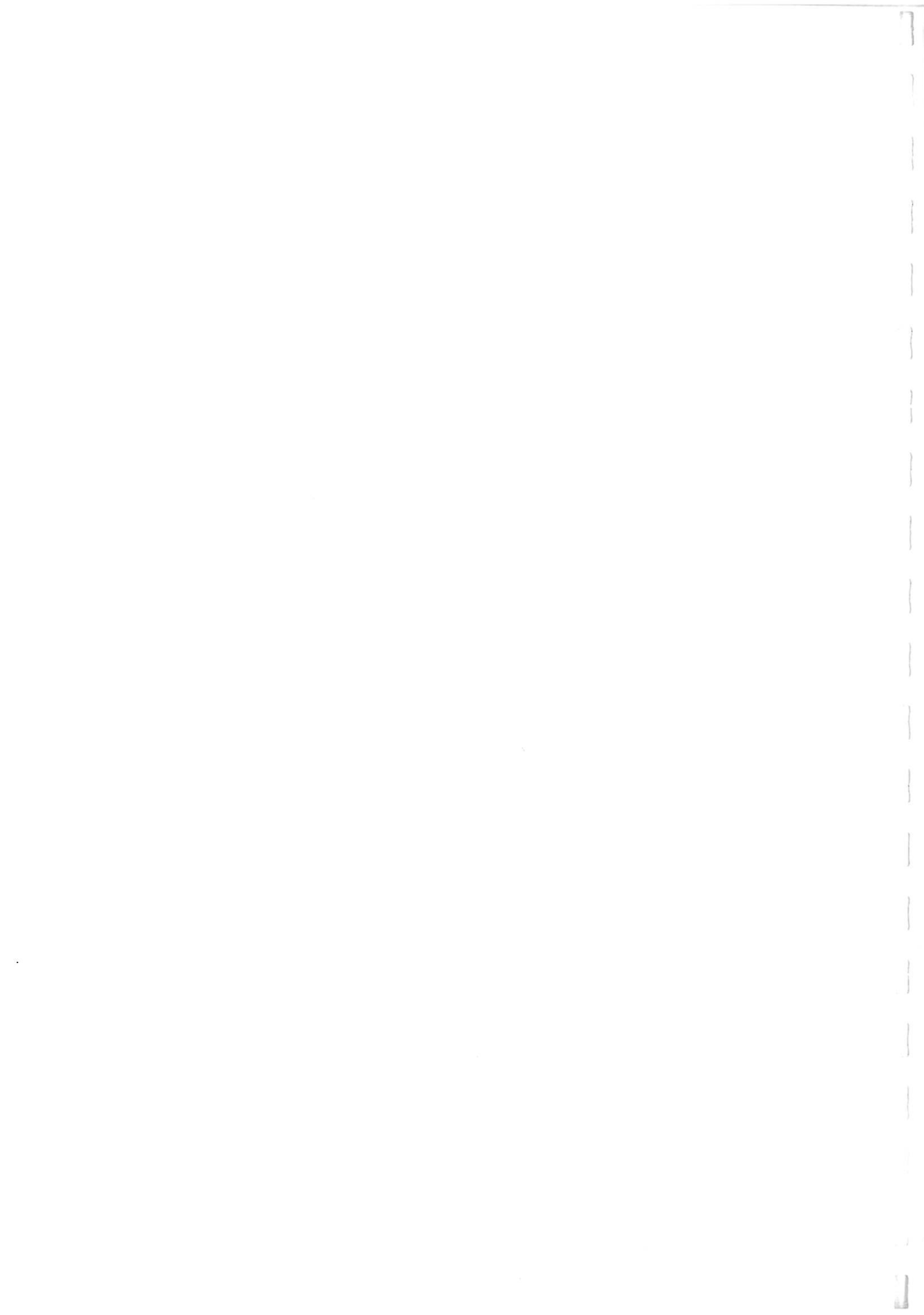
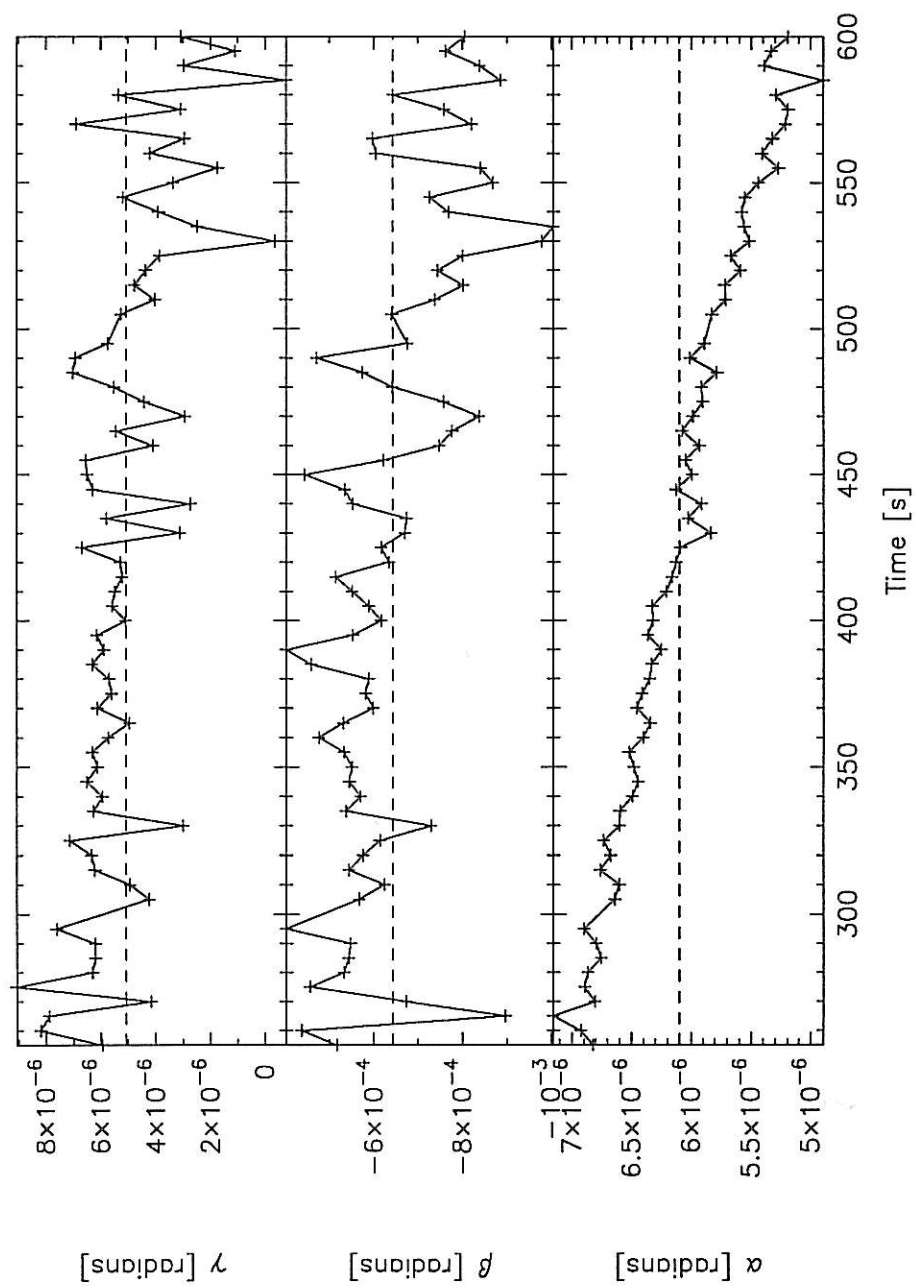


Figure 25c--Time Variation of Parameters Found by FPAM9



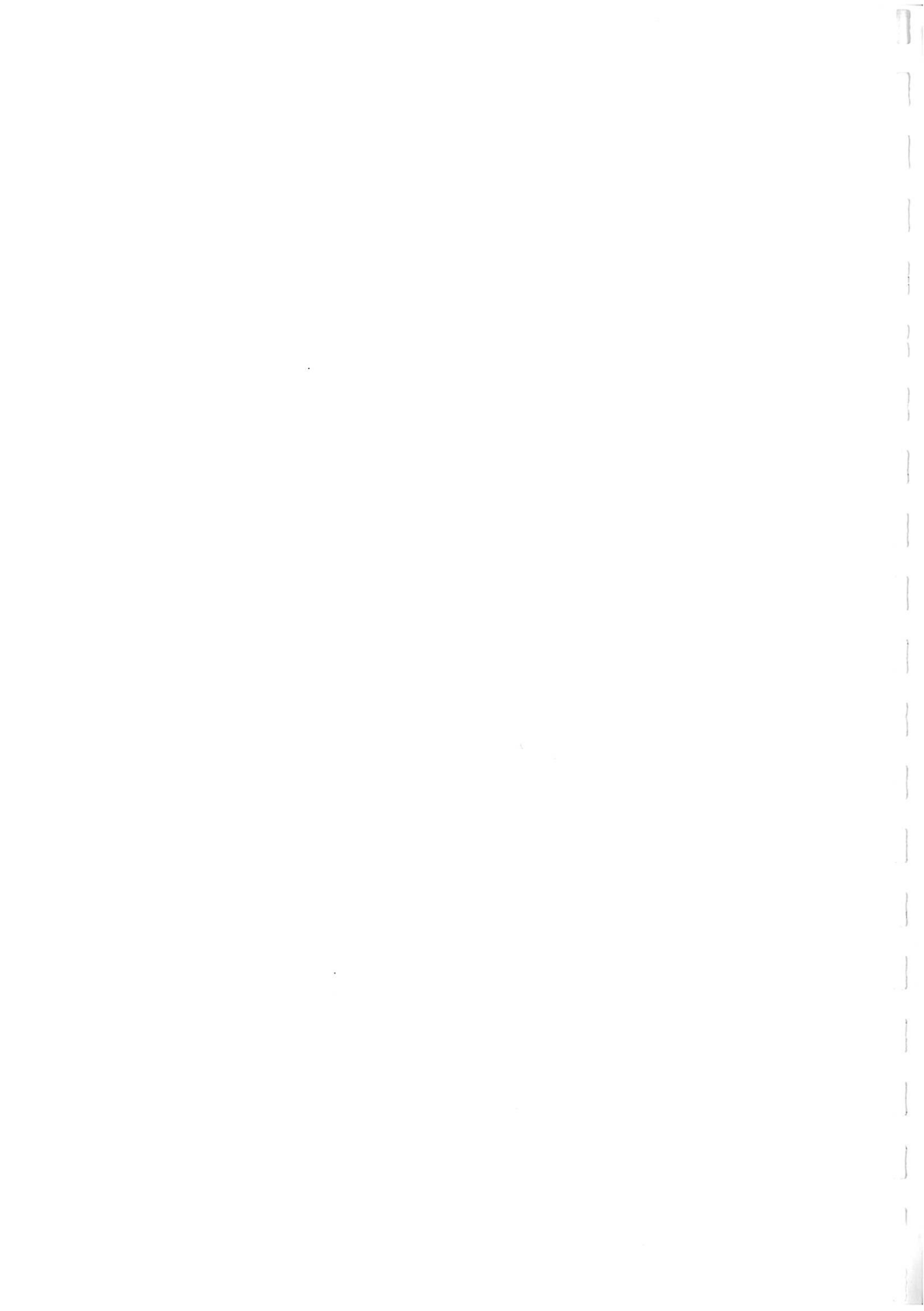
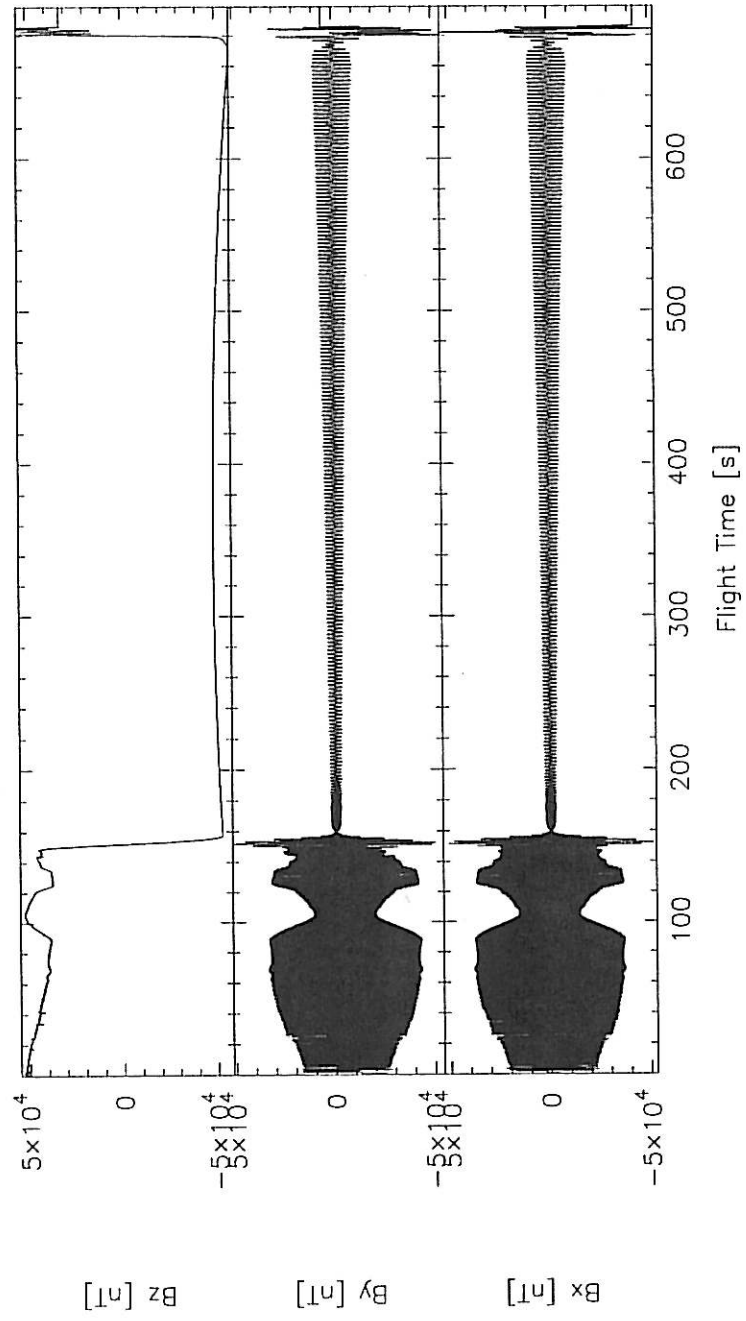


Figure 26



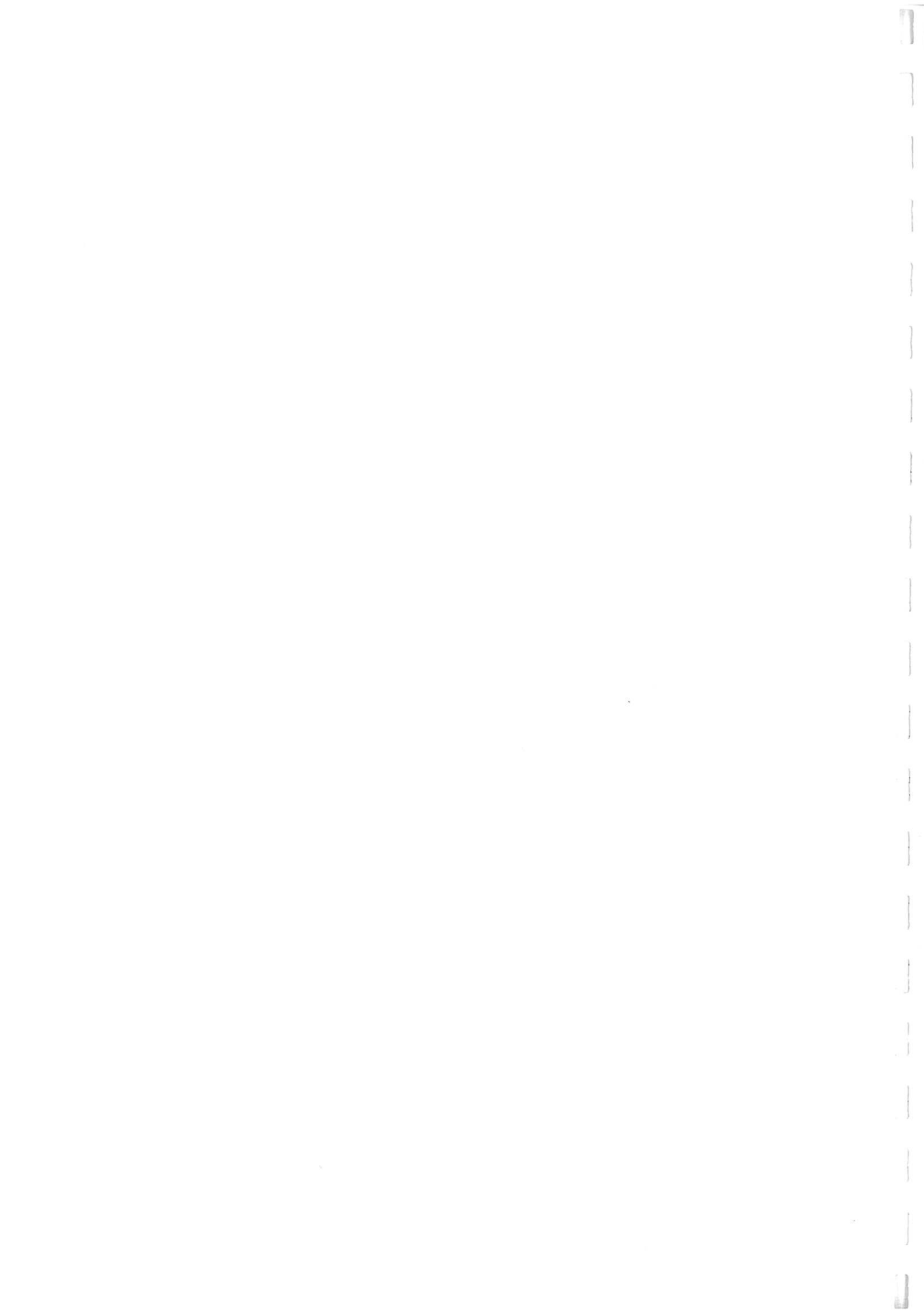
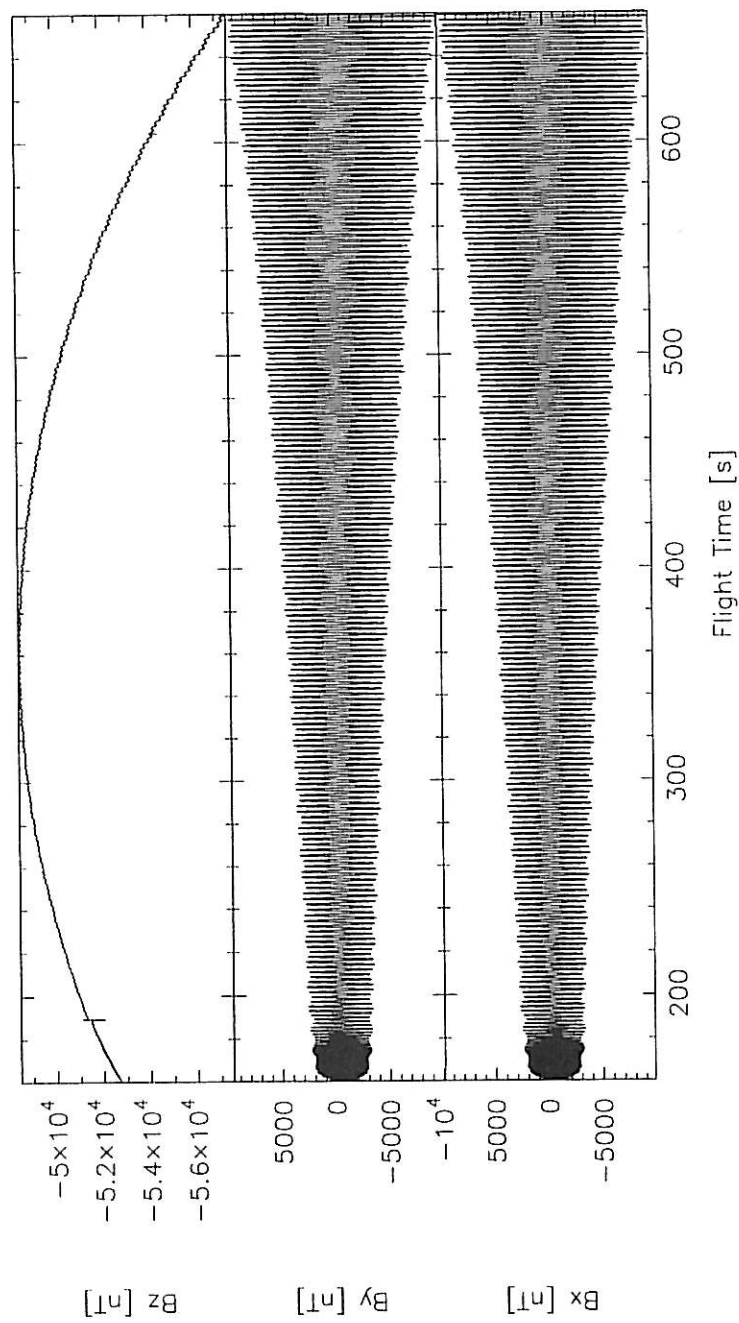


Figure 27



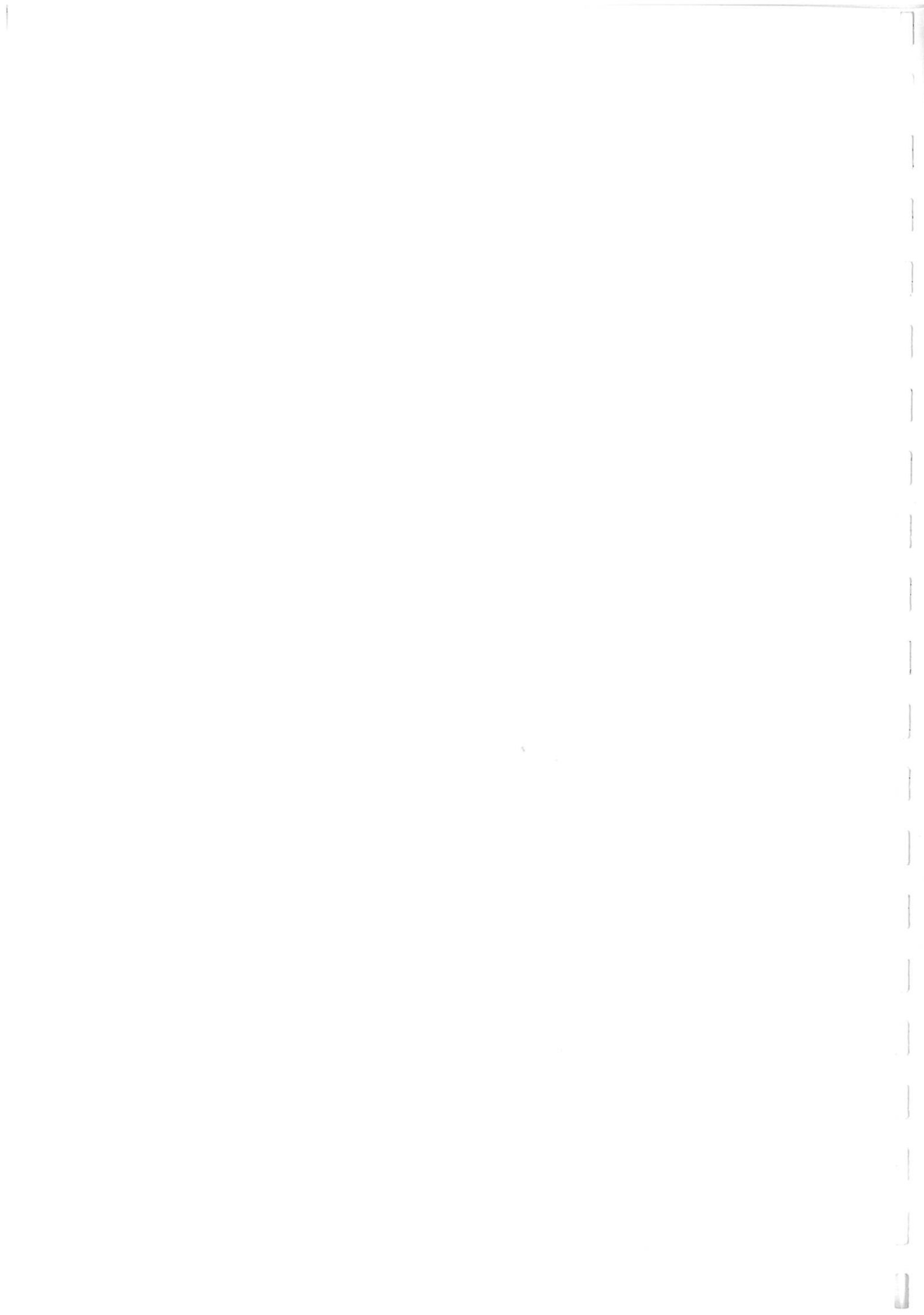


Figure 28

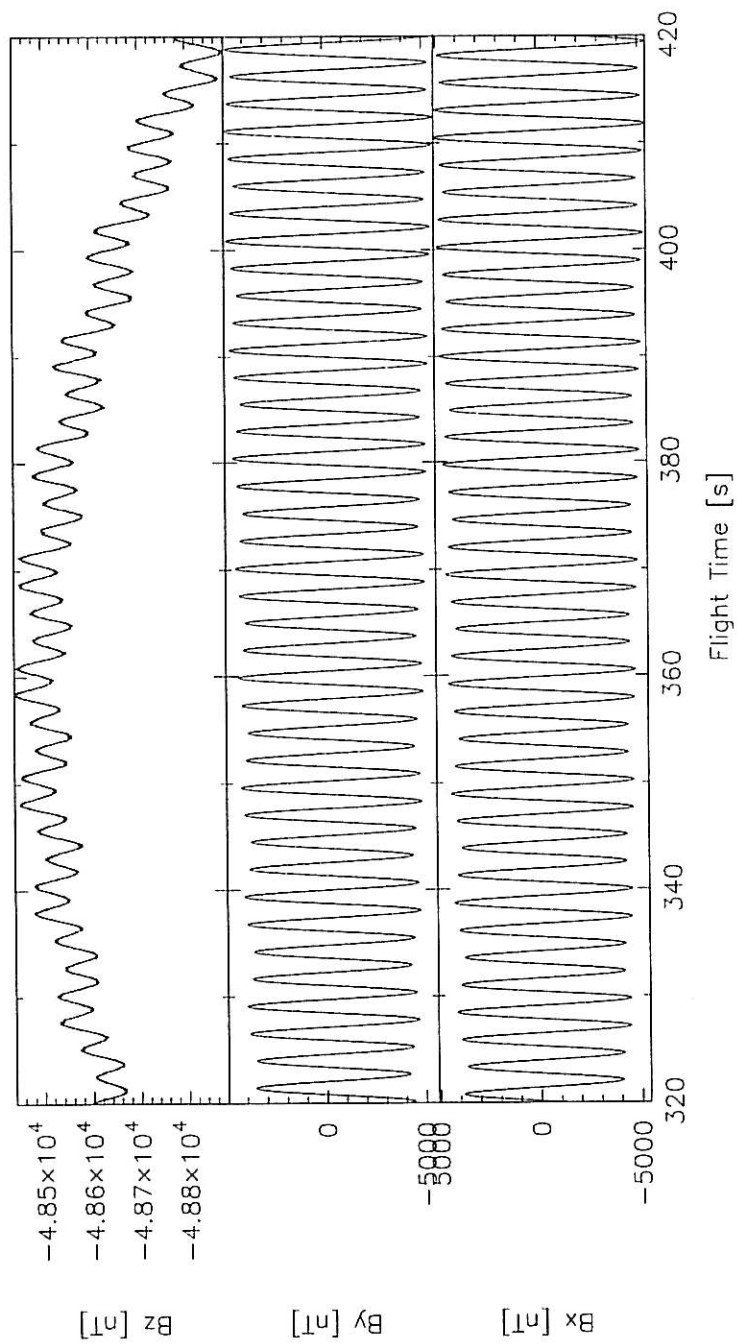


Figure 29 - Calculation of angles from magnetic field data

This diagram illustrates the technique for calculating the angle between , in this case, the background field B and the z-axis of the magnetometer. It uses the fact that the field is zero in the horizontal direction

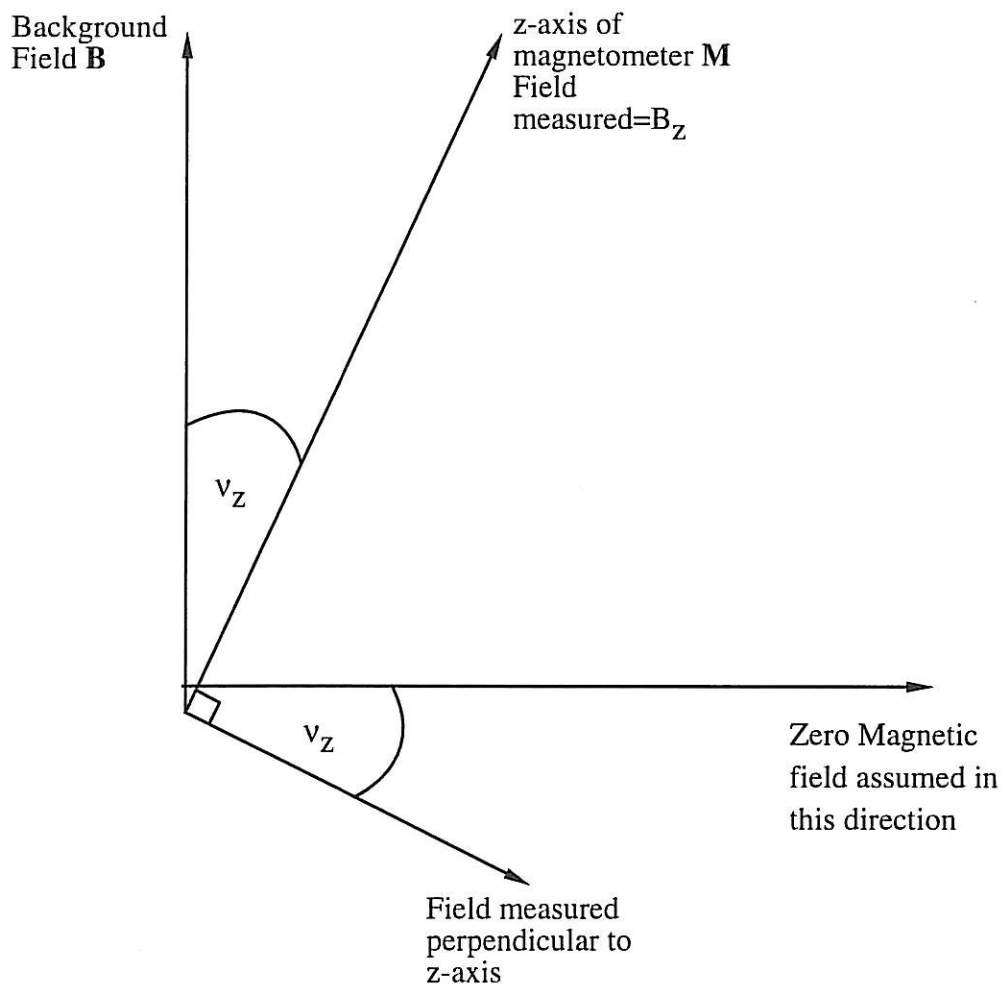




Figure 30

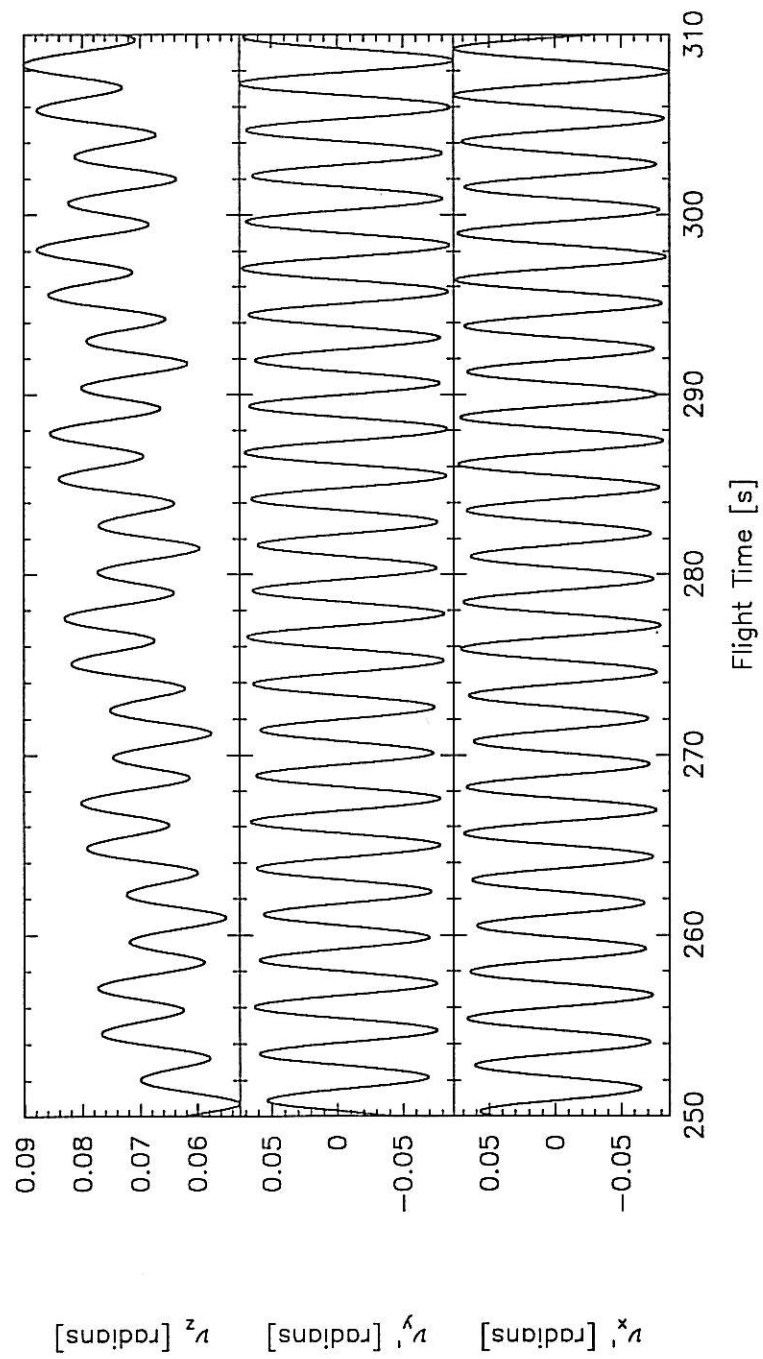


Figure 31 - Demonstration of the effect of misalignment between the z-axis of the magnetometer \underline{M} and the spin axis \underline{S}

This diagram iuses the 2-dimensional projection described in Figure 20 to show how spinning can be present in the values of v_z

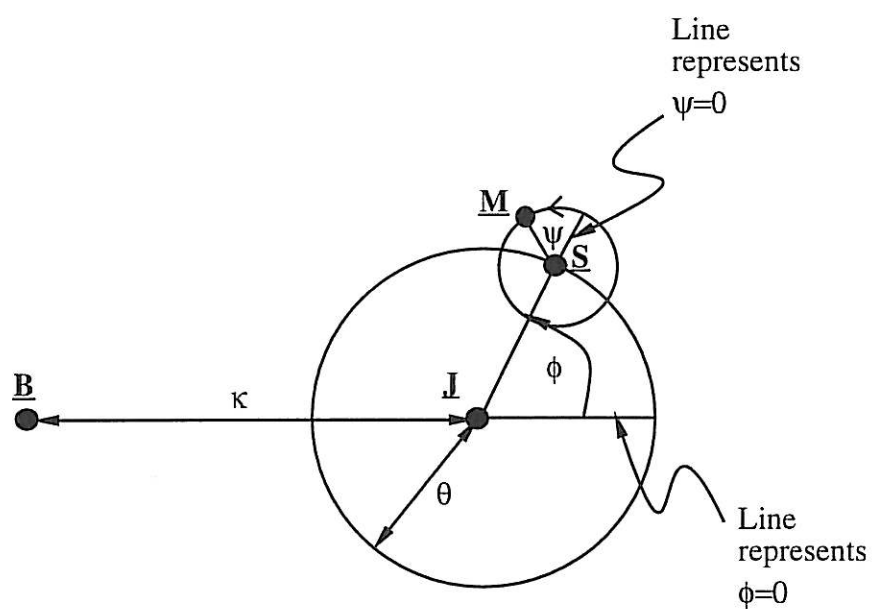
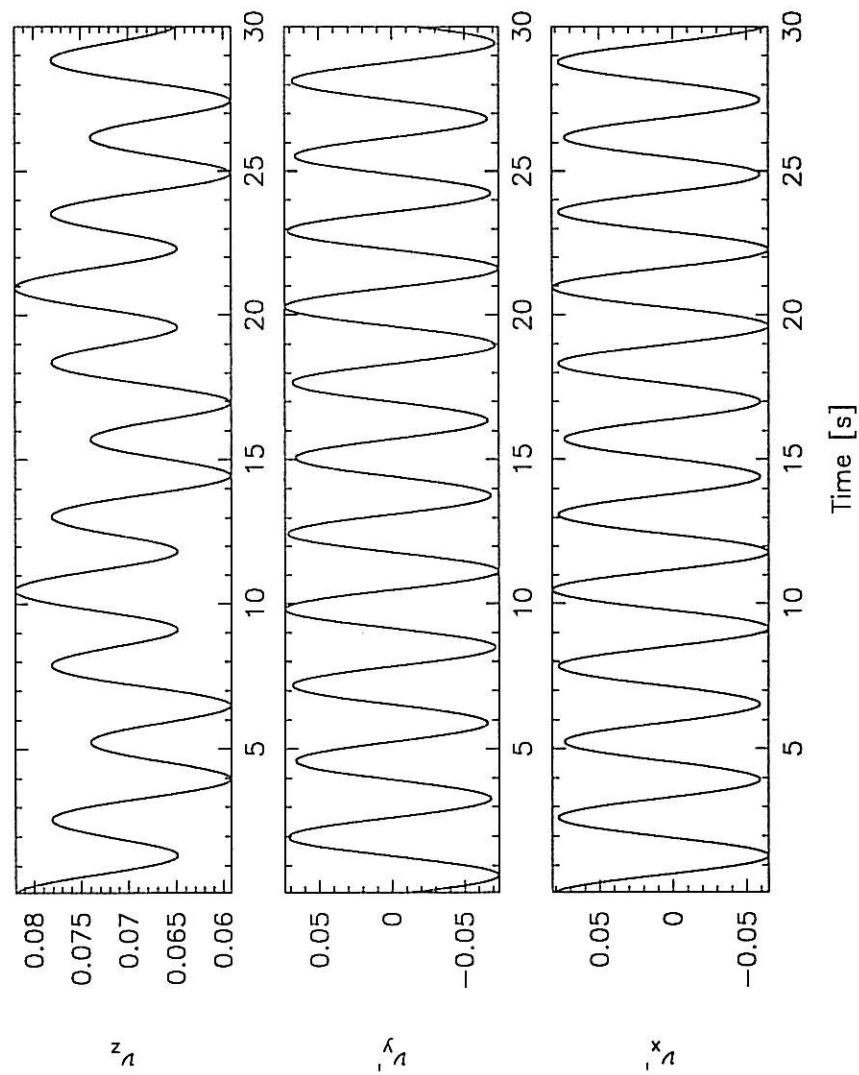
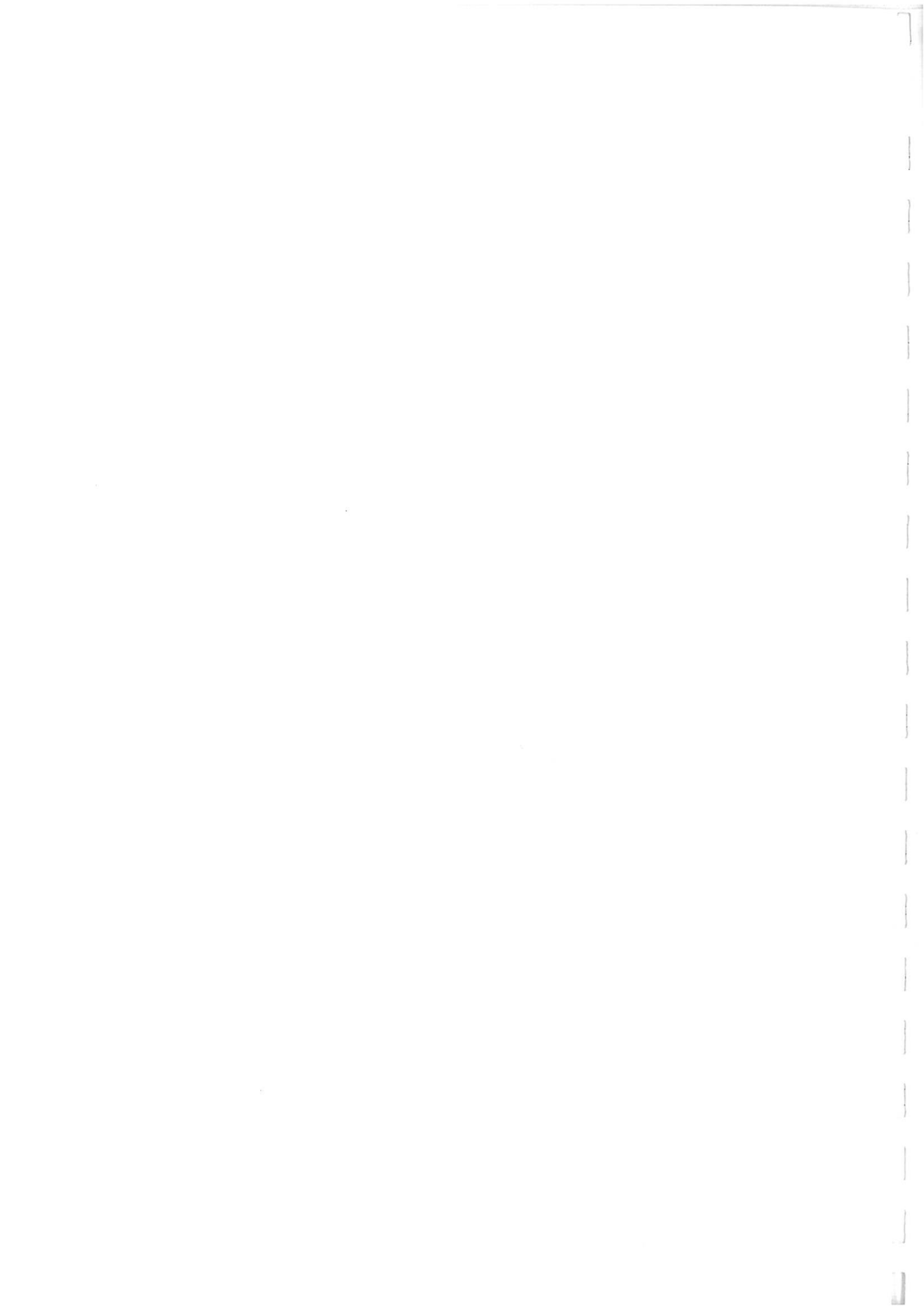


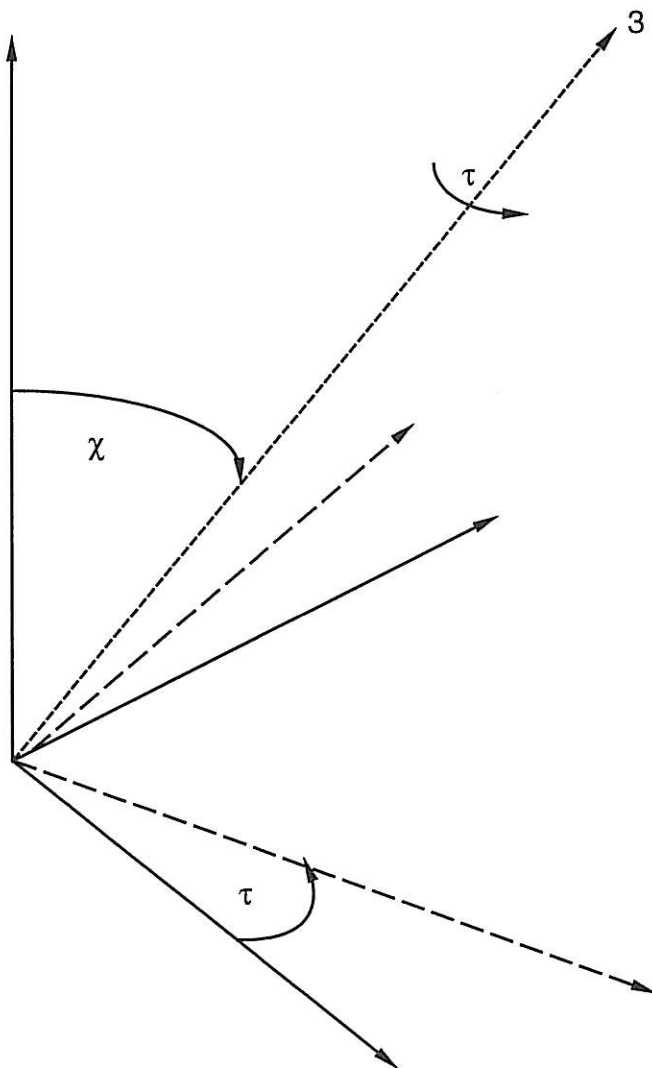
Figure 32 – Results from SIM2.FOR



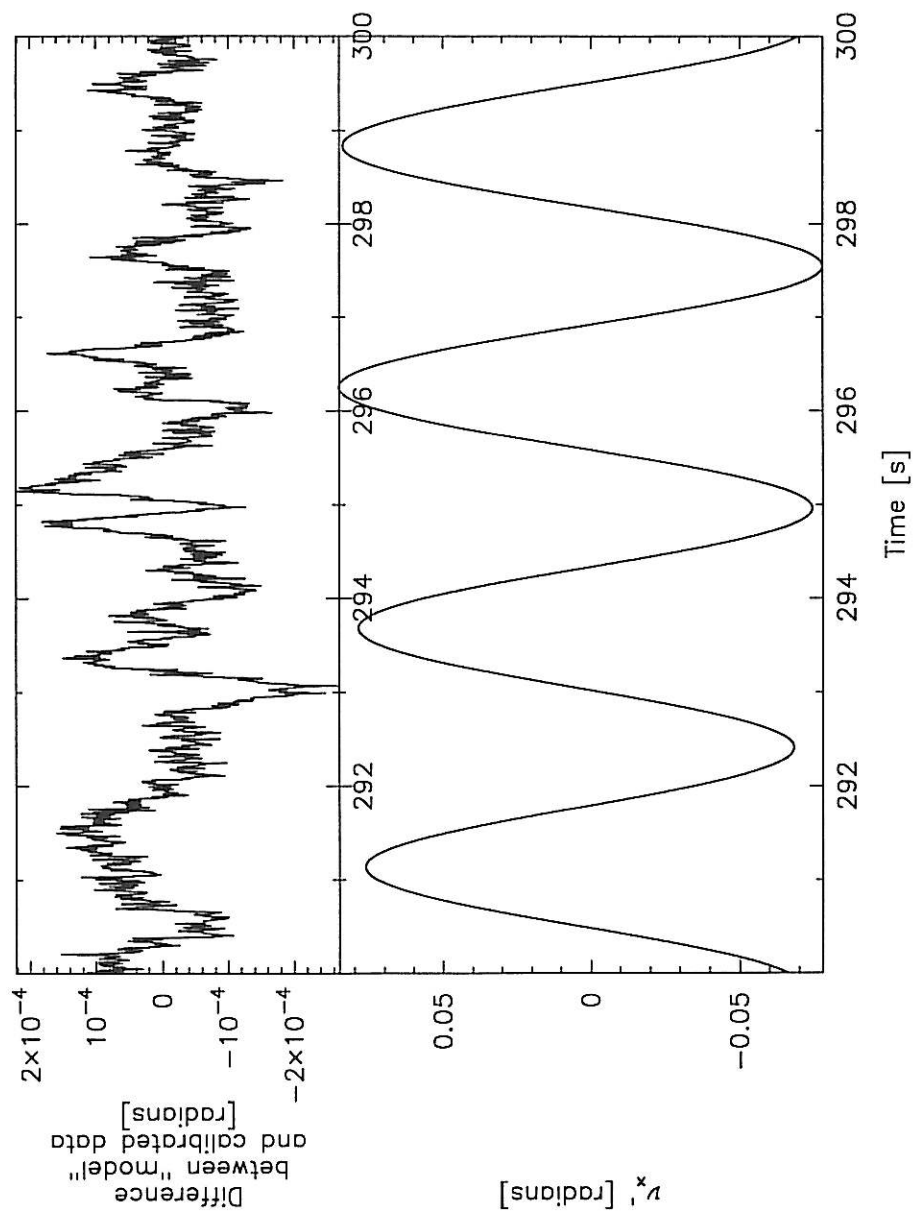


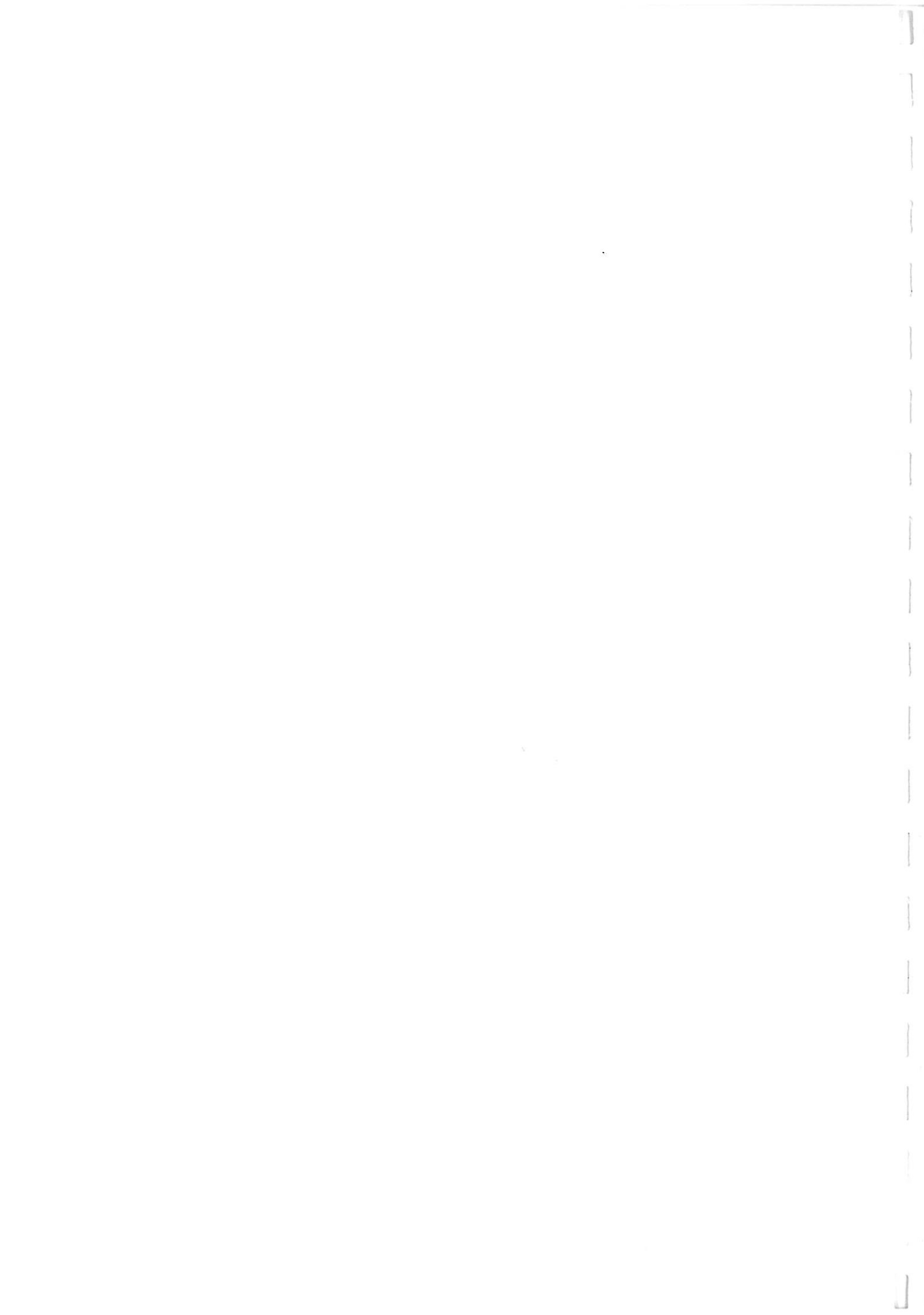
**Figure 33 - Definitions of
misalignment angles**

The misalignment with the spin axis is by an angle χ , and then the magnetometer is rotated around its own axis by an angle τ

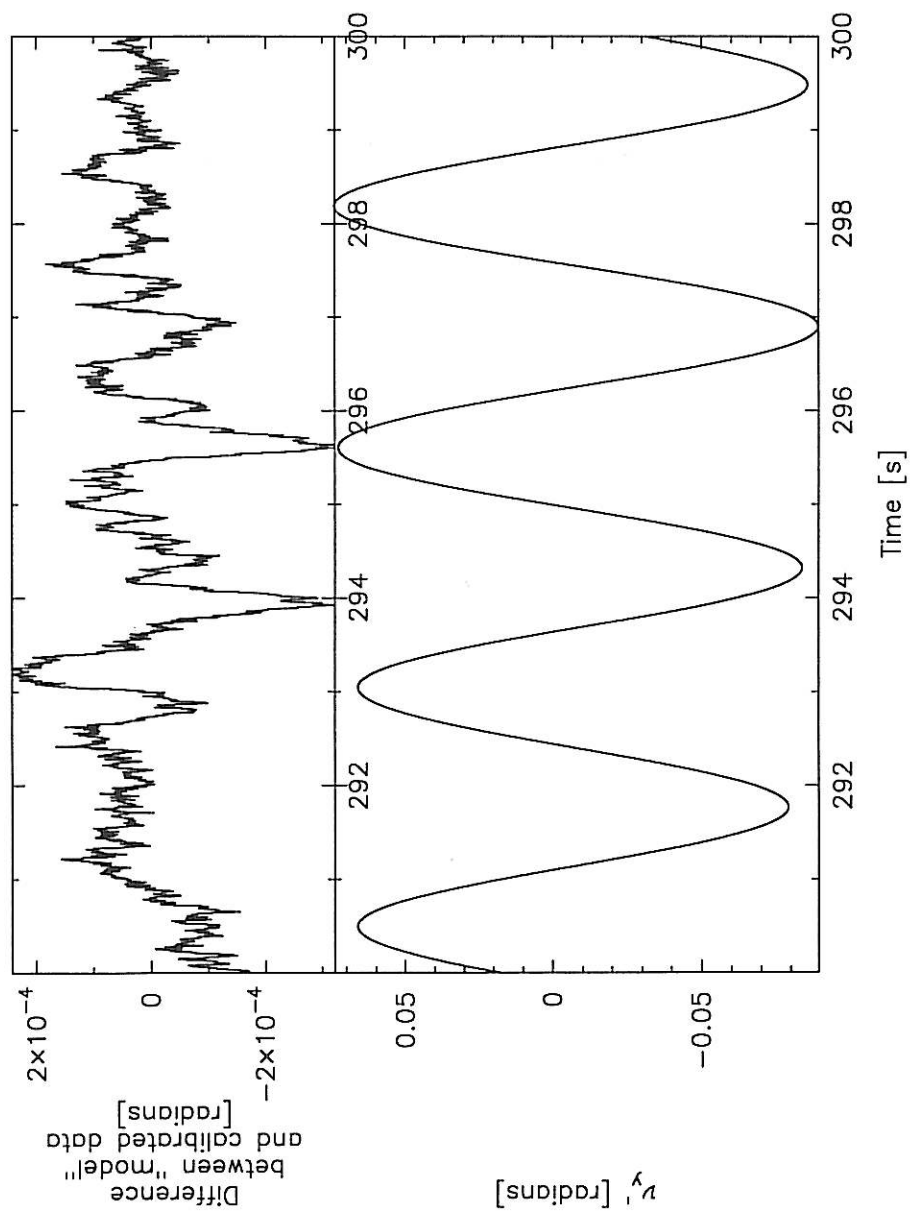


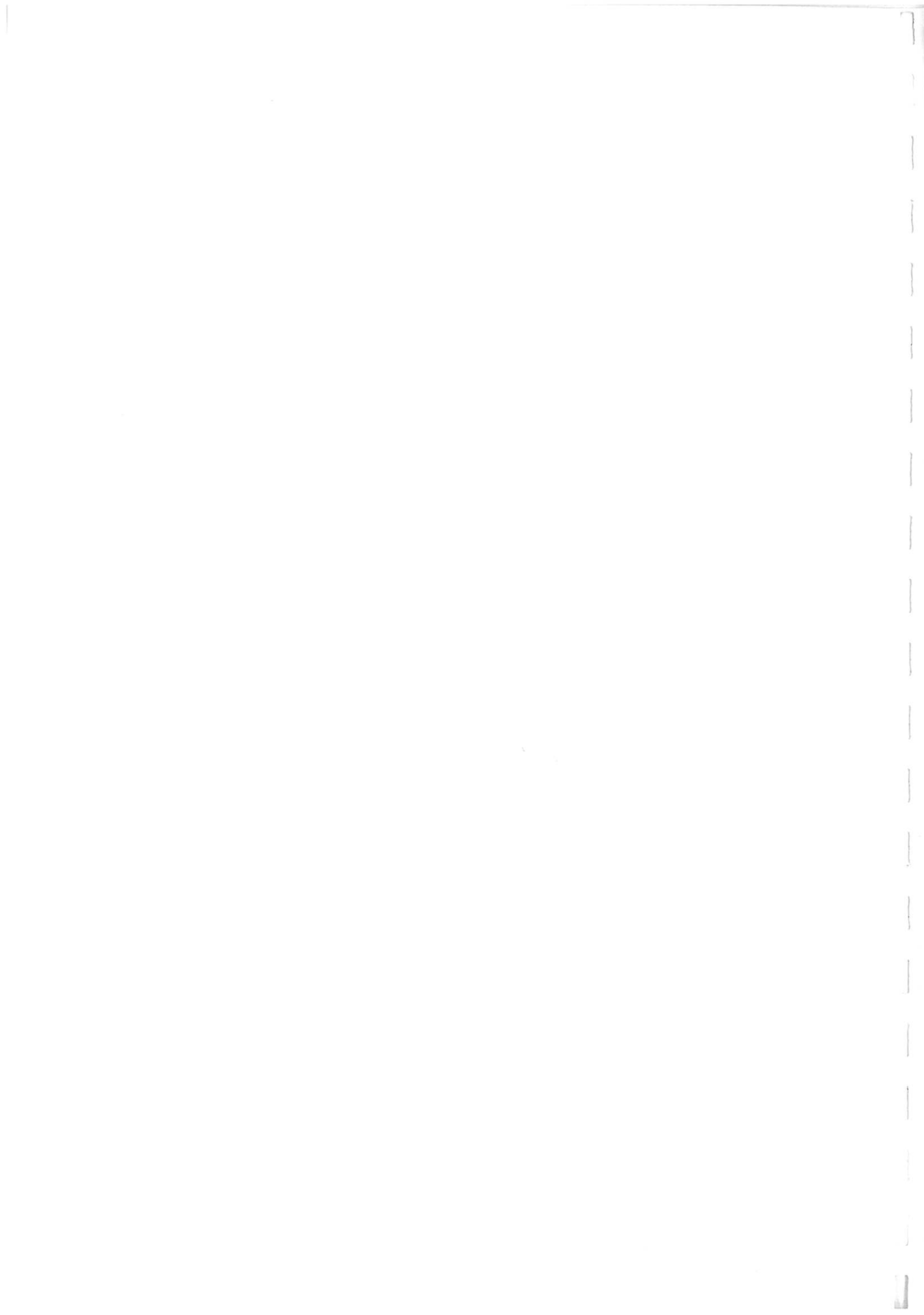
Text results in file [smith.at.fdata]290_300_10_6.txt
Figure 34 — Result from fit_10.FOR



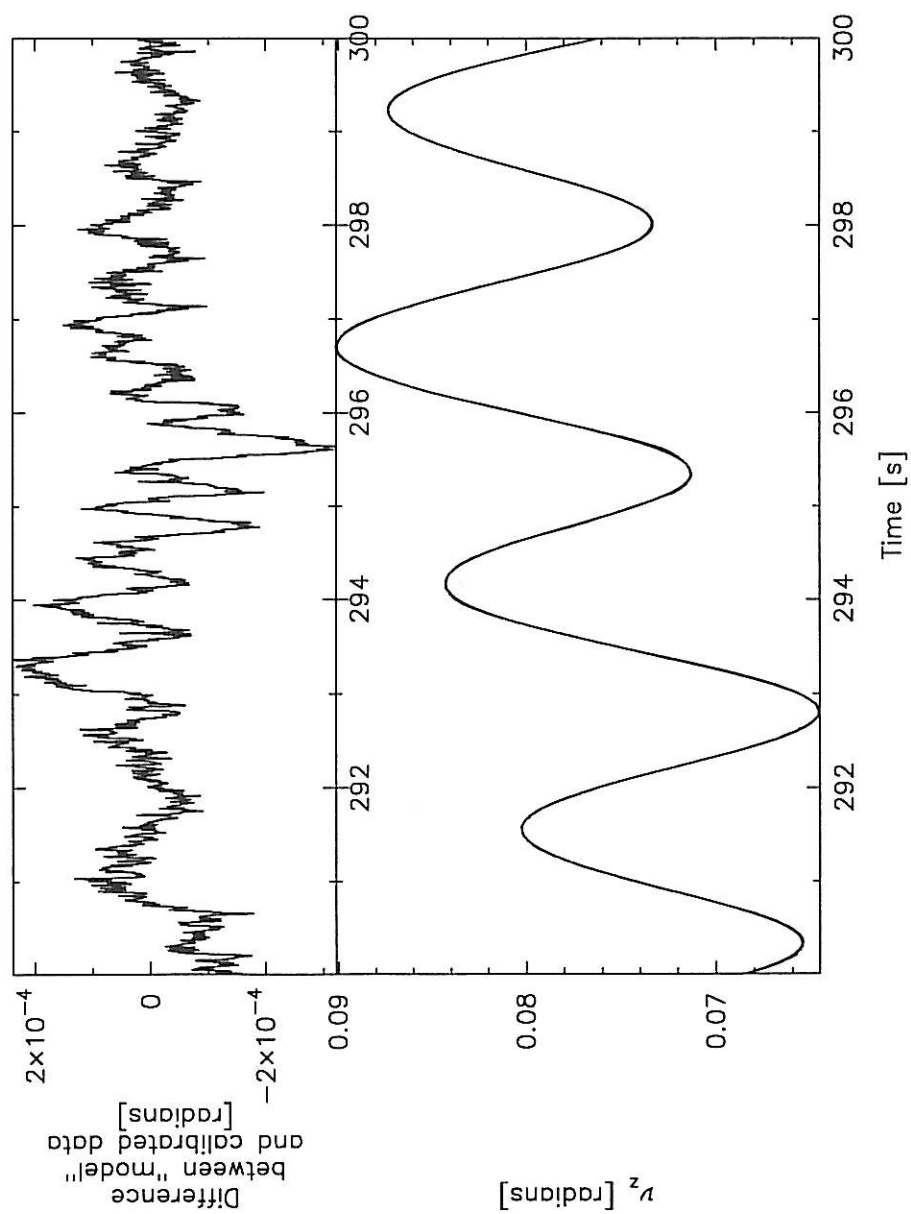


Text results in file [smith.at.fdata]290_300_10_6.txt
 Figure 34 - Result from fit_10.FOR 300_10_6.txt





Text results in file [smith.at.fdata]290_300_10_6.txt
Figure 34 — Result from fit_10.FOR 300_10_6.txt



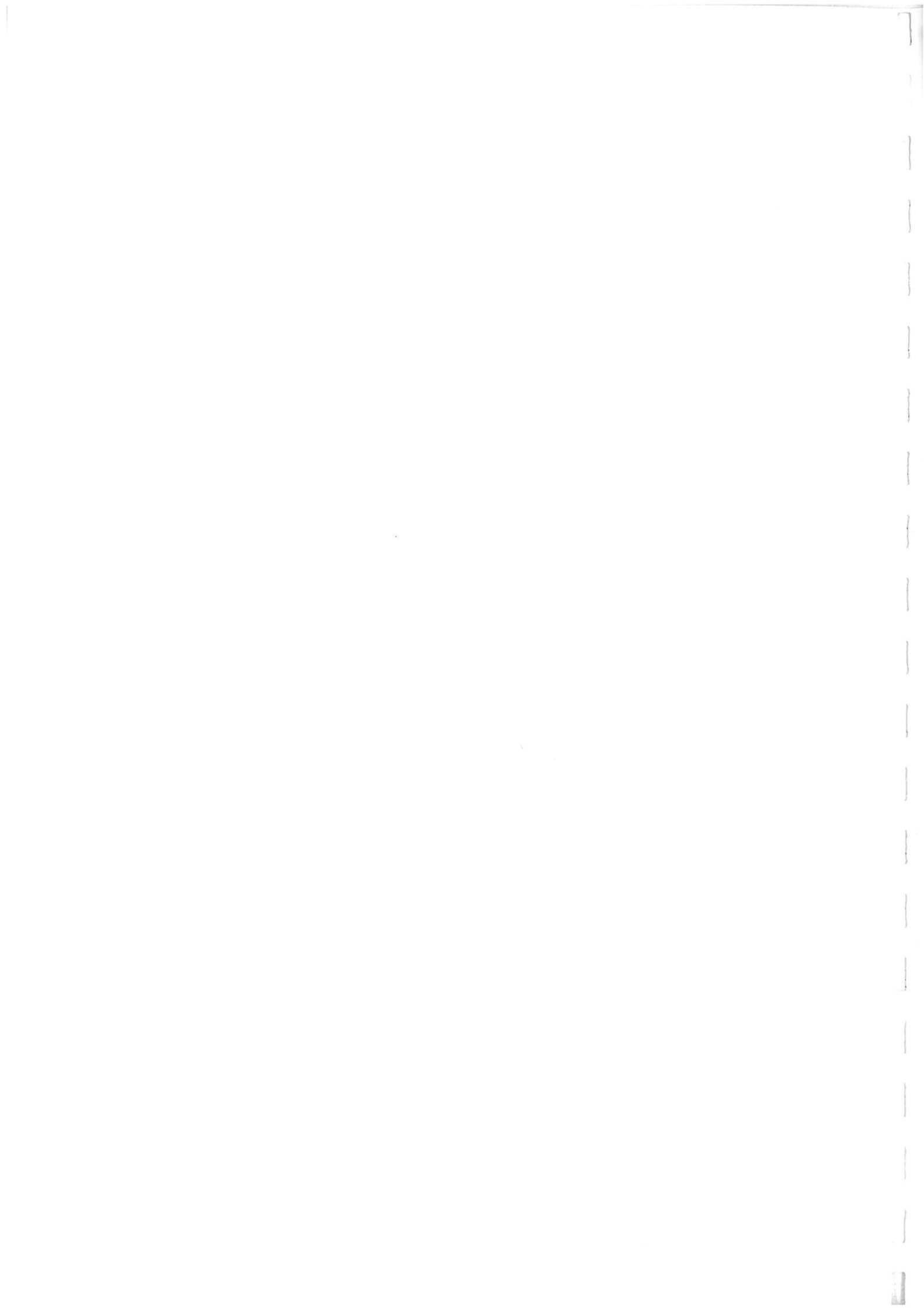
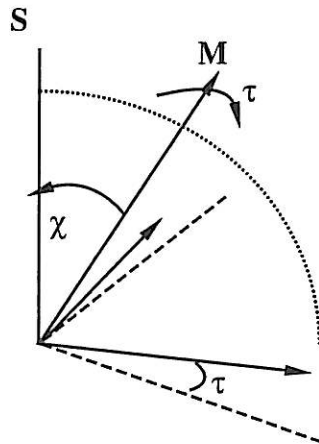
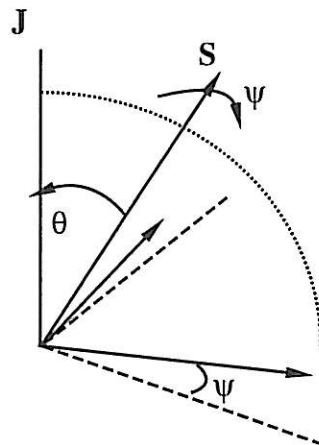


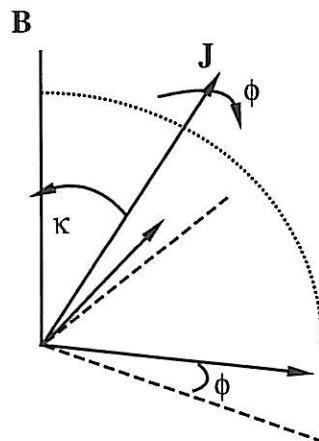
Figure 35 - Rotations required to align magnetometer



First rotate the magnetometer by τ around its own axis M , and then about its y-axis by angle χ to align with the spin axis S



Second rotate the magnetometer by ψ around its own axis $M=S$, and then about its y-axis by angle θ to align with the coning axis J



Finally rotate the magnetometer by ϕ around its own axis $M=S=J$, and then about its y-axis by angle κ to align with the magnetic field B

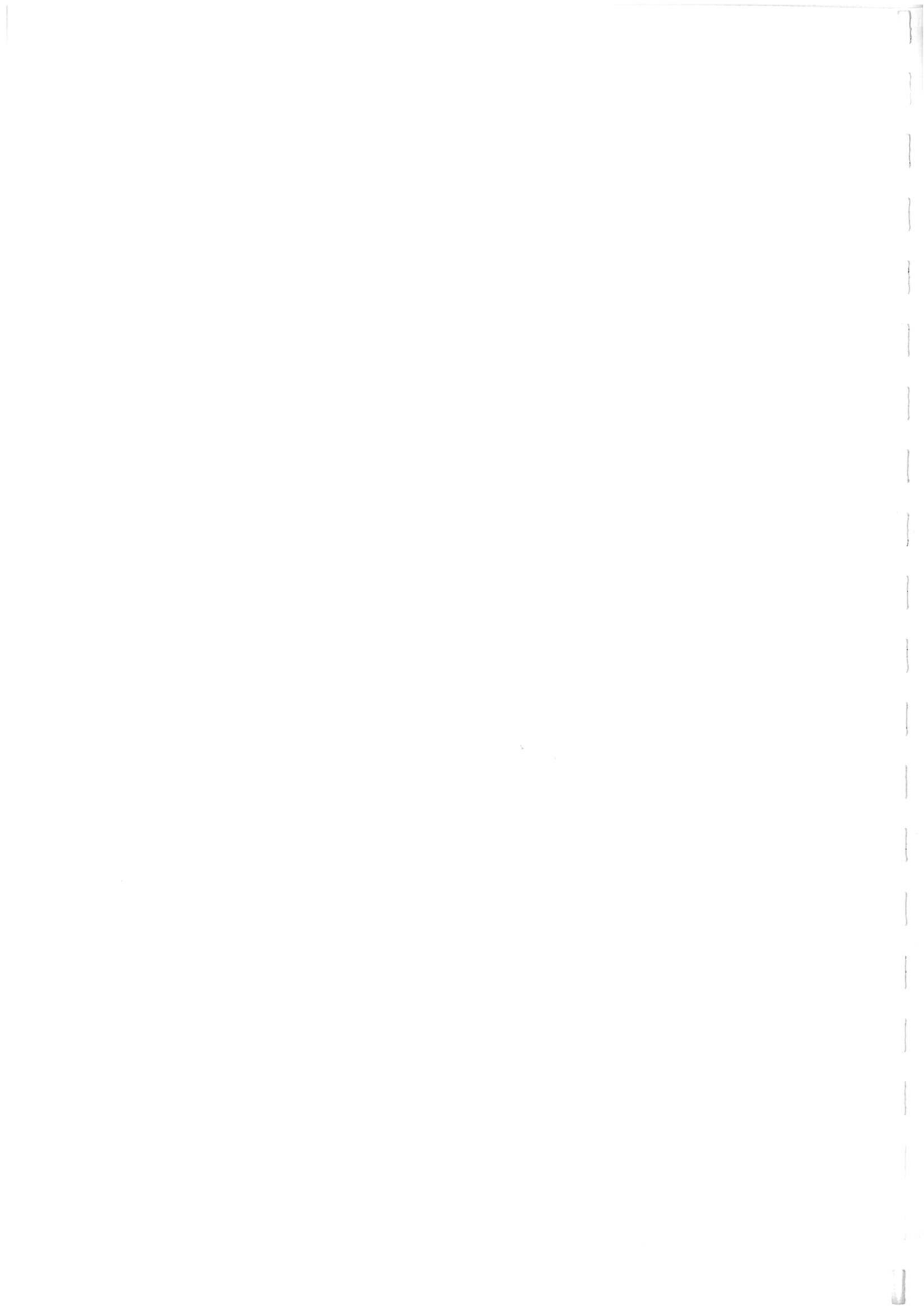


Figure 36— Three axis Magnetic Field Results

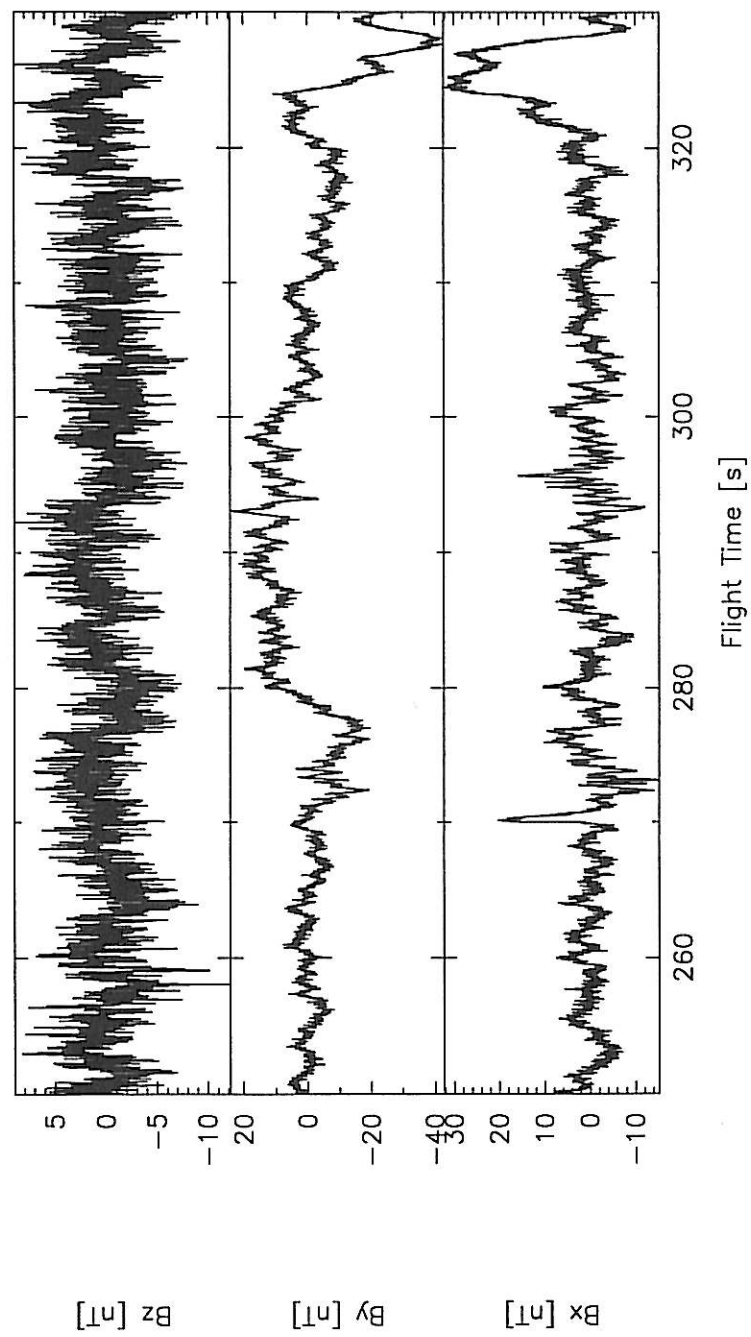
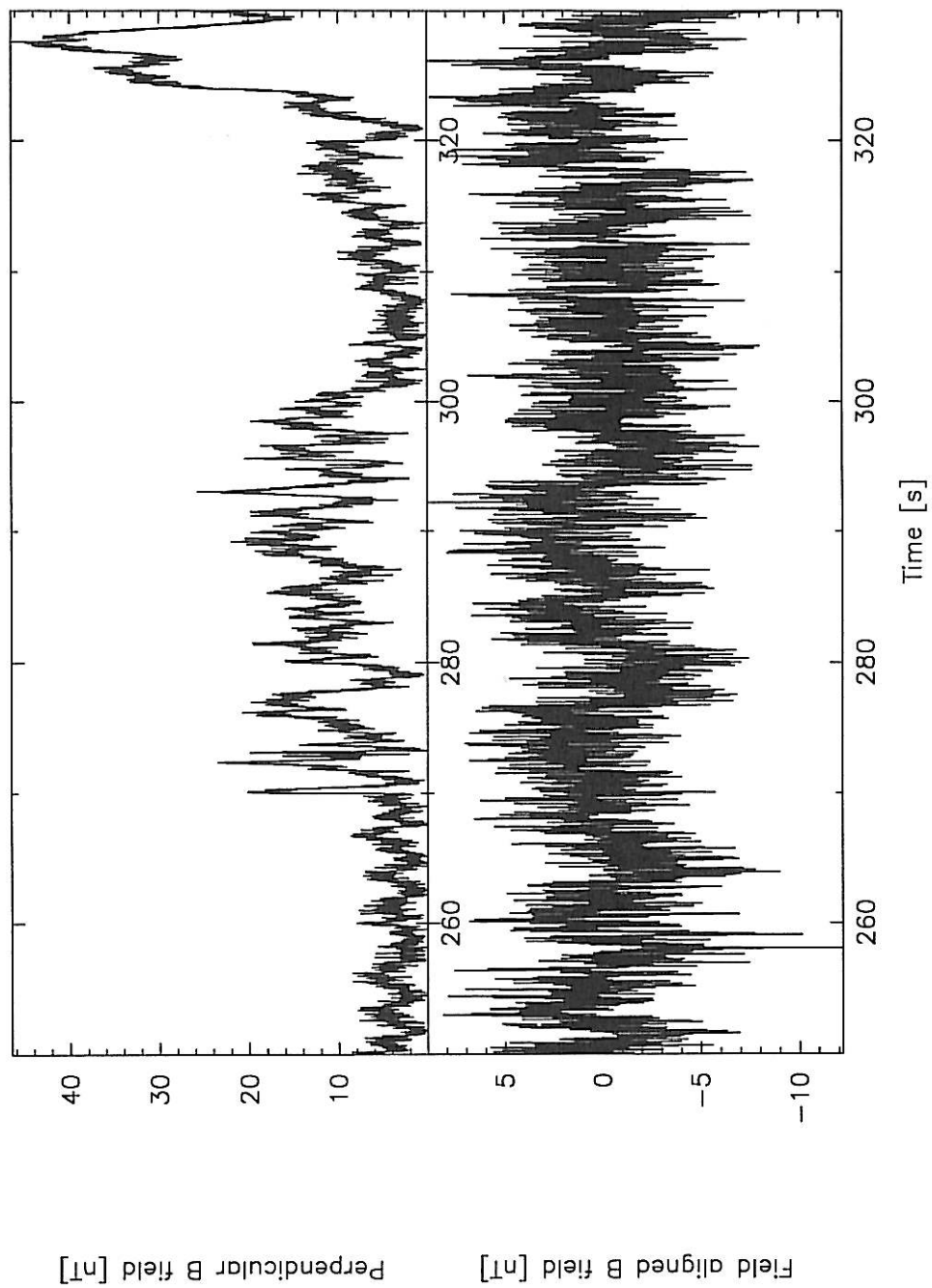




Figure 37— Parallel and Perpendicular Magnetic Fields



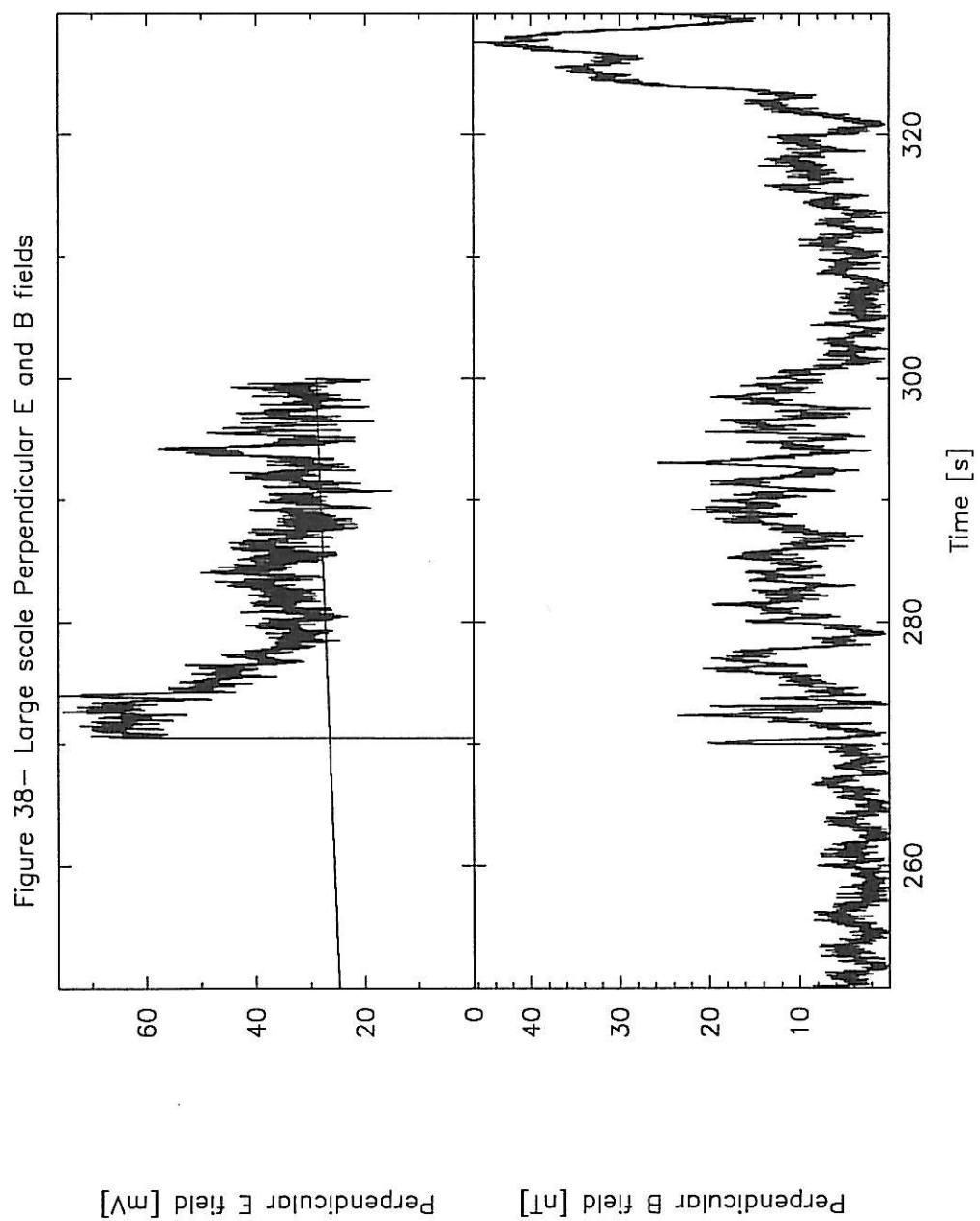


Figure 39a-- Small scale E and B field results

